DEVELOPMENT OF A SINGLE-ATOM MICROSCOPE FOR OPTICAL DETECTION OF ATOMIC NUCLEAR REACTION PRODUCTS

By

Benjamin Thomas Loseth

A DISSERTATION

Submitted to
Michigan State University
in partial fulfillment of the requirements
for the degree of

Physics – Doctor of Philosophy

2020

ABSTRACT

DEVELOPMENT OF A SINGLE-ATOM MICROSCOPE FOR OPTICAL DETECTION OF ATOMIC NUCLEAR REACTION PRODUCTS

By

Benjamin Thomas Loseth

Development of increasingly sensitive detection techniques is necessary for the measurement of extremely small nuclear cross sections that are crucial to understanding many nucleosynthesis processes. To that end, this thesis presents the first steps toward the commissioning of a novel detector, called the single-atom microscope, with a cross section measurement for the reaction $^{84}\mathrm{Kr}(p,\gamma)^{85}\mathrm{Rb}$, by optically imaging rubidium atoms in solid krypton. Techniques for the growth of highly transparent 100 μm thick films of solid noble gases are demonstrated. The absorption cross section for matrix-isolated rubidium in solid krypton is measured to be on the order of $8\times10^{-15}\mathrm{cm}^2$, with a fluorescence cross section on the order of $2\times10^{-16}\,\mathrm{cm}^2$. The fluorescence cross section of rubidium atoms embedded in solid krypton as a 1.7 MeV/u ion beam was measured to be $(9\pm4)\times10^{-16}\,\mathrm{cm}^2$. The neutralization efficiency of rubidium ions implanted in solid krypton is measured to be on the order of unity. The next steps toward imaging individual rubidium atoms in solid krypton are presented.

ACKNOWLEDGEMENTS

First of all, I am especially grateful for the guidance and support of my advisor, Prof. Jaideep Singh, and will be forever thankful to him for the opportunity to participate in this interesting and challenging scientific research. Working in Spinlab has reinvigorated my love for physics, and I will look back on the time spent here with a great fondness. It have greatly enjoyed working alongside the other Spinlab group members, including Roy, Erin, and the many other brilliant graduate and undergraduate students I have had the pleasure to work with. I want to especially thank Fry Fang for the many long days he spent working with me on pSAM - I could not have made it this far without him.

During my long tenure here at MSU I have had the privilege to get to know Kim Crosslan and Brenda Wenzlick - Thank you both for your friendship and help! Thank you to Profs. Johannes Pollanen, Martin Berz, Kyoko Makino, Pavel Snopok for supporting me with your kindness, knowledge, and advice. Working at the NSCL has been an eye-opening experience, and I could not imagine working in a more exciting facility staffed with such kind and professional staff. I want to thank Tony Swartz, Brad Powell, Chuck Gaus, and Kim Gwinn from NSCL facilities for their excellent work in powering and supporting the SAM project. Thanks to Ben Arend, Jeff Wenstrom, Morgan Burr, and Cody Norat for their excellent design work. A huge thanks to Ken Plath, Jay Pline, and the NSCL machine shop staff for their tremendously skilled work and lifesaving last-minute modifications.

I want to offer my sincere thanks to the members of my guidance committee, Profs. Luke Roberts, Hendrik Schatz, Stuart Tessmer, and Kirsten Tollefson for devoting their valuable time and energy to advise and review this research, and support me in my endeavors.

I am deeply grateful for the love, support, and kindness of my family and friends (Kairi, Alyssa, Aimee, Phil, Jon, and many others) throughout my time here at MSU, without which I could not have accomplished this dream of mine.

TABLE OF CONTENTS

LIST OF TABLES

LIST OF FIGURES

CHAPTER 1

INTRODUCTION

This thesis describes the first steps undertaken in the development of a new method for measuring the cross section of low-yield nuclear reactions. The detector, called the single-atom microscope, works by capturing the product atoms of the nuclear reaction in a cryogenically frozen noble gas solid. Once embedded in the noble gas solid, which is optically transparent, the product atoms are selectively identified with laser-induced fluorescence and individually counted via optical imaging to determine the nuclear cross section. Single-atom sensitivity by optical imaging is feasible because the surrounding lattice of noble gas atoms facilitates a large wavelength shift between the excitation and the emission spectrum of the product atoms. This novel detection scheme has the potential for near-unity efficiency, a high degree of selectivity, single-atom sensitivity, and could be used to determine a number of astrophysically important nuclear reaction rates.

This technique will first be implemented in measuring the cross section for the reaction $^{84}\mathrm{Kr}(p,\gamma)^{85}\mathrm{Rb}$. This reaction is an ideal choice for a commissioning experiment because the beam, ^{84}Kr, is a noble gas and will be optically invisible when captured in a solid krypton film. The product nuclei, ^{85}Rb, have a strong transition at a readily accessible wavelength, which is helpful in achieving single-atom sensitivity. Before implementation, a number of tasks must be accomplished in order to demonstrate the ability to count atoms in a solid noble gas film via fluorescence imaging. First, it is necessary to repeatably grow and maintain optically transparent solid krypton films of sufficient thickness to stop an energetic ion. Second, as the number of product atoms will be at least partially determined by the amount of fluorescence light emitted in the film under resonant laser excitation, the intrinsic brightness of rubidium atoms embedded in solid krypton must be determined. Third, a number of open questions exist regarding implementing the technique in an actual beamline experiment, including determining the neutralization fraction of ions stopped in the film, as well as the durability of solid noble gas thin films under heavy ion irradiation, among others.

This thesis is organized into the following topics. In Chapter 2 the single-atom microscope detection technique is described in detail, including a discussion of open questions and technical challenges to be accomplished. Chapter 3 details the design and components of the prototype single-atom microscope, as well as results of noble gas film growth studies. Chapter 4 describes the atomic beam fluorescence technique for measuring the intensity of an atomic beam, and subsequent measurement of the absorption and fluorescence cross section of matrix-isolated rubidium in solid krypton. Chapter 5 encompasses the first beamline tests for the prototype single-atom microscope, including effects of energetic heavy-ion beam implantation on a solid krypton film, ion beam-induced luminescence, and the fluorescence cross section of ion-implanted rubidium in solid krypton. Chapter 6 describes the next steps for the single-atom microscope project, including improving the absorption and fluorescence cross section measurement of matrix-isolated krypton, as well as detailing what is necessary for achieving single-atom sensitivity.

CHAPTER 2

DETECTION OF ATOMIC NUCLEAR REACTION PRODUCTS VIA OPTICAL IMAGING

2.1 Motivation

In stars and during stellar explosions, and over billions of years, intricate networks of nuclear reactions synthesized nearly every natural chemical element that we observe around us. Nucleosynthesis of most elements heavier than iron are not produced by stellar fusion but rather by neutron capture, whether it be slow and gradual individual neutron captures during stellar burning (s-process) or the rapid capture of many neutrons such as is believed to occur during neutron star mergers (r-process). There are 35 stable isotopes inaccessible to neutron-capture processes and believed to be produced through γ-induced photodisintegration (p-process) [4, 5, 6, 7].

There are a significant number of nuclear reactions that have a strong influence on nuclide abundances and whose cross sections are either unknown or poorly understood at astrophysically relevant energies. Measuring these cross sections is often technically challenging for a variety of reasons. At astrophysical energies (in the so-called Gamow window), the cross section can be extremely small due to the difficulty in overcoming the Coulomb barrier at stellar temperatures. In order to measure extremely small cross sections directly and within an acceptable time period, high beam currents and dense targets are required for the production of only a handful of reactions per day.

An inverse kinematics configuration is often utilized, where the beam nuclei have a higher mass than the target nuclei so that the reaction products scatter forward in a narrow cone. Based on their charge and mass, the few product nuclei are then separated from the beam and secondary nuclei by electric and magnetic fields in recoil separator systems [8, 9]. Alternative and often

complementary methods involve the detection of the proton, neutron, or gamma created by the reaction with an array of scintillating detectors around the reaction site [10]. Unfortunately such methods are sensitive to cosmic ray, natural, and beam-induced background sources, the rates of which can be significantly higher than that of the reaction of interest. Some experimental efforts have moved deep underground, where the cosmic-ray-induced background rates are significantly lower. For underground facilities, CASPAR at Sanford Underground Research Facility [11], and LUNA in Italy [12], background rates become limited by radioactive elements in the surrounding rock, and are $10^2 - 10^4$ times lower than on the surface.

For reactions involving rare isotopes, it can be difficult to achieve sufficient statistics due to inadequate beam intensities. Rare isotope beams can also be significantly contaminated with other nuclei as a consequence of production mechanisms, which can drastically increase background rates. Furthermore, heavy nuclei have substantial magnetic rigidity and relatively slight differences in charge-to-mass ratios, making them cumbersome to separate due to the long distances and high magnetic fields required. Typical recoil separators are less effective at high masses for the same reasons.

Novel detection schemes capable of bypassing the aforementioned challenges create an opportunity to measure exceptionally low yield nuclear reactions or other such low yield nuclear events, such as neutrinoless double-β decay. Such a detection scheme should exhibit single-atom sensitivity to the reaction products while being unsusceptible to traditional background sources. The detection methods should exhibit a high degree of selectivity between atomic species to overcome beam contamination or separation issues. A high detection efficiency is also highly desirable to maximize the probability of detecting rare events.

We propose a technique for measuring cross sections of low yield nuclear reactions by detecting the atomic products *optically*, called the single-atom microscope (SAM). The SAM is intended for reactions performed in inverse kinematics, such that most or all of the recoiling product atoms are captured inside a cryogenically frozen noble gas solid (such as neon, argon) deposited on a transparent substrate. Once trapped, an atomic resonance is excited in the product atoms with

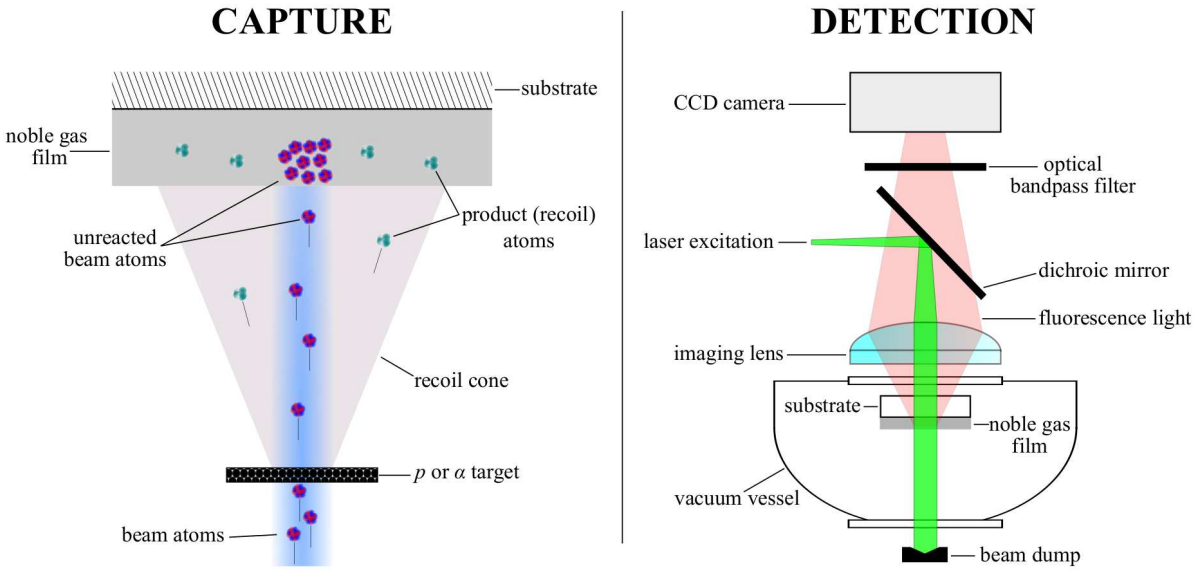

Figure 2.1: Graphical representation of the SAM concept (not to scale, noble gas film thickness exaggerated for clarity). Left: Basic capturing scheme without a recoil separator. The nuclear reaction takes place in inverse kinematics, where the recoiling products and low intensity unreacted beam are captured in a noble gas film. Right: Schematic of optical excitation and fluorescence imaging of the captured recoil atoms onto a CCD camera. The excitation light is separated from the emitted fluorescence light using optical bandpass filters.

a laser, and the emitted fluorescence light is collected by a CCD camera-based imaging system. Guest atoms that are isolated in a noble gas matrix generally exhibit blue-shifted absorption and red-shifted emission bands relative to the wavelength in vacuum for a given atomic transition. This wavelength shift between absorption and emission bands (Stokes shift [13]) can be as large as hundreds of nanometers. To detect the isolated product atoms, their red-shifted fluorescence is isolated from transmitted or scattered excitation light with optical filters to pick out the emission wavelength range of interest.

A schematic of the method is included in Fig. 2.1. We argue that single-atom sensitivity is feasible with the SAM, noting that single atom detection of barium atoms in solid xenon has been demonstrated [14, 15]. The main advantage of this approach is that the detection mechanism is not affected by traditional background sources. Neutron and γ-ray backgrounds do not affect the fluorescence spectra or detection thereof, and the product atoms are identified by their unique

atomic transitions, which are distinct from any codeposited atoms from the beam.

In Sec. II we discuss promising cross-section sensitivities for two classes of nuclear reactions. We then describe specific details regarding the capture and detection of atomic species in a noble gas solid in Sec. III. Finally, in Sec. IV the method is summarized and the benefits and limitations of the SAM detection scheme are discussed.

2.2 Cross Section Sensitivity

Table 2.1: Candidate reactions for the single-atom microscope, with approximate beam currents, target areal densities, and expected yields.

Reaction	Beam current (pps)	Target density (atoms/cm^2)	Cross section (b)	Approx. yield (products/day)	Reaction importance
^{22}Ne$(\alpha,n)^{25}$Mg	10^{15}	10^{19}	10^{-15}	1	s-process n source
	10^{15}	10^{17}	10^{-11}	100	
^{91}Nb$(p,\gamma)^{92}$Mo	10^{4}	10^{20}	10^{-5}	1	Production of p-nucleus ^{92}Mo
	10^{7}	10^{20}	10^{-3}	10^{5}	

We envision two classes of reactions where the SAM detection scheme is applicable: (i) extremely small cross-section reactions with a high-current stable isotope beam- and (ii) low-current rare isotope (radioactive) beam reactions. Table 2.1 lists approximate experimental parameters for example reactions of each type.

2.2.1 Small cross-section reactions

^{22}Ne$(\alpha,n)^{25}$Mg is a key reaction for s-process nucleosynthesis, and it has an extremely small predicted cross section in the Gamow window, of the order of femtobarns (10^{-15} b) [16]. Assuming a high-intensity ^{22}Ne beam of current 10^{15} pps incident on a windowless ^{4}He gas jet target with an areal density of 10^{19} atoms/cm^{-2} (JENSA target [17]), the expected yield for a 1-fb cross section is only a single ^{25}Mg atom per day. Due to these small yields, single-atom sensitivity to the product ^{25}Mg atoms with negligible background rates is necessary to measure a cross section for

this reaction in a reasonable amount of time, even at the highest achievable currents and target densities.

For the SAM to measure this reaction, it should be noted that such high beam currents require that the unreacted beam intensity (10^{15} pps) be attenuated by a factor of 10^6 in order to avoid melting a cryogenic noble gas film, as discussed in Sec. III. With an appropriate recoil separator to attenuate the unreacted beam intensity, this reaction is well suited for the SAM, as the beam (^{22}Ne) is a noble gas and thus any unseparated ^{22}Ne beam atoms would not contribute background fluorescence during optical imaging of the product ^{25}Mg atoms. An advantage is that, unlike some traditional detection methods, the SAM detection scheme would be immune to leaky beams or other non-magnesium beam contaminants, which can be difficult to completely eliminate from high-intensity beamline systems. It is, furthermore, desirable to have an alternative technique, which the SAM detection scheme can potentially satisfy, with different systematics than the forthcoming underground measurements due to the importance of this reaction.

2.2.2 Low-beam-current reactions

The low intensity of rare isotope beams is often the limiting factor in the cross-section sensitivity for traditional detection methods. With single-atom sensitivity and atomic species selectivity, the SAM scheme can improve upon cross-section sensitivities even with low-intensity beams. As an example, the reaction ^{91}Nb$(p,\gamma)^{92}$Mo has been identified as a key reaction in the production of the p-process nuclei ^{92}Mo [18]. A Hauser-Feshbach model (NON-SMOKER database) predicts cross sections from 1 μb to 1 mb in the Gamow window [19]. At the National Superconducting Cyclotron Laboratory (NSCL), a ^{91}Nb beam can be produced with a current of order 10^4 pps, which will be further improved to 10^7 pps at the upcoming Facility for Rare Isotope Beams (FRIB). An advantage of such small currents for SAM is that no beam rejection or recoil separator will be necessary to protect the noble gas film, easily allowing for a capture efficiency approaching unity. Using a proton target (CH_2, of density 0.25 mg/cm^2), for a 10-μb cross section roughly one ^{92}Mo atom is produced daily at NSCL beam intensities, and the same yield allows for 10-pb cross

sections to be probed with FRIB beam currents assuming negligible background rates.

Gamma-based detection methods are handicapped by lower efficiencies and are susceptible to cosmic ray and environmental γ sources, requiring more beam time to achieve sufficient counts above background (typically hundreds of counts for good statistics). Similar difficulties exist for low-energy neutron detection. Reactions involving higher mass nuclides, such as $^{91}\mathrm{Nb}(p,\gamma)^{92}\mathrm{Mo}$, easily exceed the design magnetic rigidity acceptance of contemporary recoil separator systems [8, 9] unless a high charge state is selected, a limitation on the overall efficiency despite the near-unity detection efficiency of recoils after the separator. The SAM has the potential to significantly outperform γ, neutron, and electromagnetic separator-based methods for some rare isotope reactions due to shorter beam-time requirements to amass sufficient statistics, especially for lower cross sections where expected yields are small.

2.3 Technical Challenges

A number of technical challenges must be overcome before this method can be applied to measuring the cross section for a low-yield reaction. Chief among them, single-atom sensitivity must be demonstrated for the product species of interest, which we argue is feasible for many species. Achieving single-atom sensitivity requires performing time-dependent calibrated fluorescence spectroscopy of the species of interest in a solid noble gas, as well as optical background characterization at excitation and emission wavelengths appropriate for the product species to be detected. As laser intensity and optical requirements may not allow for imaging the entire area containing product atoms simultaneously, a laser scanning system will be implemented to raster across the surface of the deposited solid noble gas film. Furthermore, single-atom detection should be achieved for short optical integration times, so the optical signal-to-background rate should be maximized to ensure that imaging the entire substrate via rasterized scanning is not prohibitively time-consuming. There are also a few outstanding questions regarding capture and neutralization of energetic ions in a cryogenic solid noble gas.

2.3.1 Capture in noble gas solids

To capture the products, generally speaking, a solid noble gas film of thickness 100 μm is sufficient to fully stop an ion with a kinetic energy of a few MeV per nucleon [20], which is at the higher end of the energy range for most reactions of astrophysical interest. Highly transparent thin films of thickness 100 μm can be deposited in about an hour with an area of 20 cm^2 or larger, which matches the size of the focal plane for a typical recoil separator. The specific properties of most noble gases in solid form are listed in Table 3.1. The selection of which noble gas to use for a given reaction will depend primarily on the matrix-isolated spectra of the product atoms to be detected. The polarizability of the noble gas atoms has a significant effect on the spectra of trapped atoms [21].

There are a few important factors to consider regarding the capture of energetic ions in a noble gas solid. First, some amount of damage will be inflicted on the noble gas film through direct heating and surface sputtering due to exposure to an energetic ion beam. Second, all product atoms are highly ionized and may not be completely neutralized before stopping in the film. As ions may have drastically different spectra than neutral atoms, the fraction of product atoms which remain ionized may be optically undetectable. Third, it is unclear what trapping site the stopped atoms will occupy in the face-centered cubic (fcc) lattice formed by noble gas atoms (called the noble gas matrix), and trapping sites are known to affect the spectra of the captured atoms [22].

2.3.1.1 Noble gas film damage

Two obvious mechanisms affect the maximum beam intensity at which significant damage is inflicted on the noble gas matrix. The kinetic energy of any unseparated beam atoms is deposited as heat in the noble gas film, which will cause the film to sublime for sufficient beam intensities. This effect may be especially significant for neon due to the single-digit temperatures required for solidification, where the cooling power of contemporary pulse-tube cryocoolers is only of the order of 1 W. The heavier noble gas films will be more resistant to direct-heating sublimation, as the cooling power improves to tens of watts at higher temperatures. It is important to note that

Table 2.2: Properties of noble gas solids.

	Ne	Ar	Kr	Xe	Ref. No.
Lattice structure	fcc	fcc	fcc	fcc	[23]
Lattice constant (Å)	4.464	5.311	5.646	6.132	[24]
Triple point (K)	24.56	83.81	115.78	161.37	[24]
ρ_{solid}, t.p. (g/cm^3)	1.444	1.623	2.826	3.399	[25]
T$_{solid}$ (K, 10^{-6} Pa)	7.3	27.4	38.4	51.3	[26]
Sublim. energy (meV)	19.6	80	116	164	[27]
Polarizability (Å^3)	0.394	1.641	2.484	4.044	[23]
Refractive index	1.11	1.29	1.38	1.49	[28]

noble gas ices are electrical insulators, and will, therefore, have poor thermal conductivity at low temperatures, which may prove to be a limiting factor despite sufficient cooling power [1]. To get a sense of a typical heat load, a 3 MeV/nucleon ^{91}Nb beam with a current of 10^8 pps would deposit a tolerable 4 mW.

A likely more significant damage mechanism is surface sputtering of the film by the beam and products. Noble gas matrices are relatively loosely bound, and each incoming energetic ion will eject some number of noble gas atoms from the matrix, typically called the sputtering yield. This effect can be compounded under high beam intensities, as the ensuing higher temperatures due to kinetic energy deposition increase the noble gas atom mobility and effectively lowers the surface binding energy. For light ions (p or α) with a kinetic energy of the order of MeV incident on sufficiently thick, low temperature noble gas films, the sputtering yield is determined by the sublimation energy and the electronic stopping power of the noble gas solid [29, 27].

The literature only reports sputtering of noble gas films by heavy ions at a low kinetic energy, in the range of 1–10 keV, where the sputtering yield is dominated by nuclear stopping power among other effects [30, 31], in contrast to the light ion case. Balaji *et al.* report sputtering yields as high as $10^3 - 10^5$ with 5-keV ions for various combinations of Ne, Ar, Kr, and Xe ions and targets [31]. To get a more macroscopic understanding of this effect, under a beam intensity of 10^9 ions/cm^2/s, such sputtering yields correspond to a thickness loss of roughly $0.002 - 0.2$ μm/hr. Studies have not been performed for medium- to high-mass ions impingent on noble gas solids at astrophysical

energies of a few MeV per nucleon, where the electronic stopping power will be dominant, and where electronic stopping powers are an order of magnitude higher than in the light-ion case. Extrapolating the low-energy heavy-ion sputtering yields to astrophysical energies, the maximum thickness loss would increase to 2 μm/hr, assuming that sputtering yields are proportional to the total stopping power.

2.3.1.2 Product ion neutralization and trapping

For studies of the optical spectra of atomic species in noble gas matrices, samples are typically prepared by depositing an initial layer of the noble gas matrix on the cooled substrate, followed by a layer of co-deposited noble gas and guest species, and finished with a final layer of noble gas to ensure that each guest atom is isolated (i.e. surrounded by noble gas atoms). The guest species are usually deposited with either an effusive or an ionic source; studies of Na^+ ions deposited in Ar [32] and Ba^+ ions in Xe [33] have shown spectra consistent with those of their neutral counterparts, and it is known that the charge state of energetic ions stopped in medium approaches 0 [34]. However, as noble gas solids have poor electrical conductivity, it is unknown whether there is a sufficient population of loosely bound electrons for complete neutralization. Furthermore, it may be advantageous for some species to remain singly ionized due to more favorable spectroscopy.

The implantation mechanism for energetic nuclear reaction product ions, which will penetrate some depth into the film, is starkly different from the typical preparation method. In particular, the reaction products will be highly ionized before implantation and it is not clear what percentage of the product ions will become fully neutralized during and after stopping in the noble gas film. Furthermore, the trapping site of the stopped product atom in the noble gas atom lattice may be unstable or significantly different from the trapping sites for typical noble gas matrix samples. Fortunately, annealing noble gas films have been shown to recover atoms in unstable trapping sites [22]. These questions require further investigation as they directly limit the SAM detection efficiency.

Table 2.3: Selected matrix-isolated absorption and emission spectra of SAM-friendly species. Italicized lifetimes are vacuum values from the NIST Atomic Spectra Database (physics.nist.gov).

Atom	Z	Vacuum transition		Matrix isolated		Lifetime (ns)	Ref. No.
		assignment	λ (nm)	absorption λ (nm)	emission λ (nm)		
Li	3	2p ^{2}P←2s ^{2}S	671.0	Ar 656.5-679.0	900	*26*	[35]
Na	11	3p ^{2}P←3s ^{2}S	589.2, 589.8	Ar 536.0-594.5	670-710	13 – 28	[36]
K	19	4p ^{2}P←4s ^{2}S	766.7, 770.1	Ar 666.4-746.7	850-950	20 – 75	[37]
Rb	37	5p ^{2}P←5s ^{2}S	780.2, 795.0	Ar 705-755	877	~20	[21, 38]
		4d ^{2}D←5s ^{2}S	516.5	Ar 420-540	630	~100	[38]
		6p ^{2}P←5s ^{2}S	420.5	Ar 420-540	630	~100	
Cs	55	6p ^{2}P←6s ^{2}S	852.3, 894.6	Ar 822-845	970	*30.5*, *35*	[38]
		5d ^{2}D←6s ^{2}S	685.1	Ar 610-670	762	2.2×10^{10}	
		7p ^{2}P←6s ^{2}S	455.6	Ar 440-520	762	*543*	
Be	4	2p ^{1}P←2s ^{1}S	234.9	Ne 232.0	232	*1.8*	[39]
				Ar 235.0-237.0	465	1.33×10^9	
				Kr 240.5	464.7	9.5×10^7	
Mg	12	3p ^{1}P←3s ^{1}S	285.3	Ne 275.3	296.5	2.03	[40]
				Kr 277.0-296.0	297-326	1.25 – 2.25	[41]
		3p ^{3}P←3s ^{1}S			472	8.91×10^6	
Ca	20	4p ^{1}P←4s ^{1}S	422.8	Ar 422.0	432.9	*4.6*	[42]
		4p ^{3}P←4s ^{1}S			647.6	8.6×10^5	
Sr	38	5p ^{1}P←5s ^{1}S	460.9	Ar 447	466.2	*5*	[43]
		5p ^{3}P←5s ^{1}S	689.4		709.2	2.1×10^4	
Ba	56	6p ^{1}P←6s ^{1}S	553.7	Ar 532	550	*8.4*	[33]
				Xe 561-566	570-591		
Zn	30	4p ^{1}P←4s ^{1}S	213.9	Ne 205.4	212.8	1.15	[40]
				Xe 219.9	356, 399	$> 10^4$	[44]
		4p ^{3}P←4s ^{1}S	307.7	Ar 297		2.6×10^4	[45]
Cd	48	5p ^{1}P←5s ^{1}S	228.9	Ne 216.5-221.7	227.2	1.26	[40]
		5p ^{3}P←5s ^{1}S	326.2	Ar 312.4		2.5×10^3	[45]
Hg	80	6p ^{3}P←6s ^{1}S	253.7	Xe 253.2		*119*	[45]
Al	13	3d ^{2}D←3p ^{2}P	308.3	Ne 260.0		*17*	[46, 47]
		4s ^{2}S←3p ^{2}P	394.5	Ne 320.0		*20*	
S	16	3p ^{1}S$_0$ ← 3p ^{3}P$_1$	459.0	Ar 456.9		3.3×10^9	[48]
		3p ^{1}S$_0$ ← 3p ^{1}D$_2$	772.7		785	2.3×10^5	
Mo	42	5p z ^{7}P← 5s a ^{7}S	379.8	Ar 341.3	399.0	$> 10^3$	[49]
		5s b ^{5}D← 5s a ^{7}S			496.8	1.5×10^5	
Yb	70	6p ^{1}P← 6s ^{1}S	398.8	Ne 388.2	394.9	*5.2*	[50]
		6p ^{1}P← 6s ^{1}S	555.8		546.0	6.8×10^2	[51]

2.3.2 Optical signal-to-background estimates

After capture, the product atoms must be identified and detected in the noble gas film based on their atomic spectra. It is advantageous that the spectral behavior of atoms and molecules isolated in noble gas matrices has been a field of study in chemical physics for decades, and so the spectra of many atomic species have been measured in a variety of matrices. Broadly speaking, the transitions of atomic species isolated in noble gas matrices are qualitatively similar to the transitions in vacuum, however, transition wavelengths can be shifted by tens to hundreds of nanometers and exhibit significantly broadened linewidths (typically 1–10 nm). Table 2.3 lists a subset of the available atomic spectra in noble gas matrices along with the vacuum transition wavelengths. The lifetimes of allowed transitions are not significantly affected in medium [51], and so transitions lacking any available lifetime data in medium are listed with their vacuum lifetimes. This table is not exhaustive, as many species and transition data have been omitted for brevity, but it does include species compatible with the SAM detection scheme.

The physics of atoms and their electronic spectra interacting with noble gas atoms is thoroughly reviewed in [22]. Our proposed optical detection scheme relies on the shift between excitation and fluorescence spectra exhibited by most species in medium (see Fig. 2.1), which allows for the selective optical filtration of any transmitted or scattered excitation light. Divalent atoms, in particular, can exhibit considerable shifts due to an intersystem crossing behavior, such as Yb in Ne [52], Mg in Kr [41], and Hg in Ar and Kr [53], where the perturbative effect of the noble gas lattice facilitates a radiationless transition from an excited state to an adjacent or lower-lying state.

2.3.2.1 Single-atom signal rate

The net optical signal rate due to a single resonantly emitting atom is simply the fluorescence intensity F (number of photons isotropically emitted per unit time) per atom multiplied by the efficiency of the optical imaging system, which we estimate to be of the order of 10^{-2}–10^{-3}. Optical imaging efficiency includes factors due to the solid angle, transmission efficiency of optical filters for wavelength separation of the excitation from emission light (Semrock, Rochester, NY),

and wavelength-dependent quantum efficiency of CCD cameras. Laser-coolable atoms are ideal, as they are generally characterized by cycling transitions with no or minimal repumping. For an alkali atom under resonant excitation from the ground state a to the first excited state b, the fluorescence intensity F is half the inverse of the excited state lifetime, assuming that the excitation light is of sufficient intensity. Consulting Table 2.3, the $^2S \rightarrow ^2P$ transition of Rb atoms in solid Ar exhibits a 20-ns lifetime, corresponding to an optical signal rate of roughly 25–250 kHz depending on the imaging efficiency.

The alkaline earth elements, with two valence s-shell electrons, are slightly more complicated. As depicted in Fig. 2.2, upon resonant excitation from $a \rightarrow b$, there is some chance of transfer from b to a lower-energy metastable state m with a significantly longer lifetime. Mg atoms in solid Kr exhibit a 2-ns lifetime for the $^1S \rightarrow ^1P$ transition, corresponding to an optical signal rate of 0.25–2.5 MHz. However, emission from the triplet ^3P state was also observed with a 9-ms lifetime (0.5-Hz optical signal rate) [41]. Detection of a Mg atom via the ^1P emission appears feasible based on these lifetimes, as a sufficient number of photons will be detected before the atom transfers to the metastable ^3P state. Waiting for the metastable state decay or repumping the atom with a secondary light source should allow for recovery of the ^1P emission band. This blinking into and out of metastable states is characteristic of a single emitter, and observation of blinking behavior would go towards confirmation of single-atom sensitivity. It should be noted that detection of the ^3P emission is technically feasible, as the optical signal rates are still well above the dark count rate of order 1 mHz for state-of-the-art CCD cameras (Andor, Belfast, United Kingdom). Furthermore, background rates may be significantly lower at the 472-nm ^3P Mg emission compared to the 297- to 326-nm ^1P emission, whether it be due to the effectiveness of optical filters for intense ultraviolet excitation light, the relative wavelength shift between excitation and emission bands, or the fluorescence of impurities in the windows and optics.

Detection of a transition metal like molybdenum is expected to be more challenging than the previous cases, with a $4d^5 5s^1$ electronic configuration and $a\ ^7S$ ground state. Studies of matrix isolated Mo in solid Ar and Kr by Pellin *et al.* [49] report substantial nonradiative transfer to

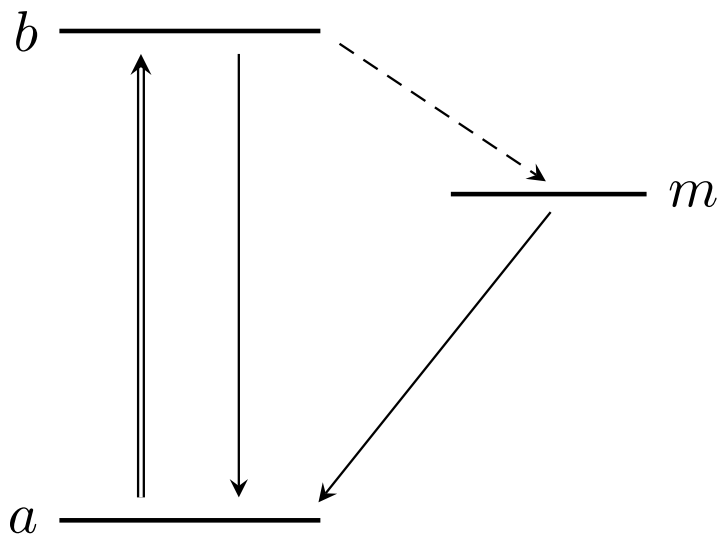

Figure 2.2: Generic energy level diagram for a three-level system with ground state a, excited state b, and metastable state m. Excitation is labeled by the double arrow; emission, by single arrows; and nonradiative transfer is denoted by the dashed arrow.

metastable states widely separated in gaseous Mo atoms despite the spin, parity, or J selection rules. Emission from metastable $b\,^5D$, $a\,^5P$, and $a\,^5F$ states were observed with similar lifetimes after excitation to $z\,^7P$ in an argon matrix. Taking the reported in-medium lifetimes at face value (Table 2.3), observation of the $z\,^7P$ fluorescence will yield kHz signal rates, while the metastable $b\,^5D$ state would yield 30-Hz signal rates. The challenge becomes determining an excitation scheme that effectively mimics the three-level system depicted in Fig. 2.2, analogous to the magnesium case.

2.3.2.2 Signal-to-background estimation

Estimating the optical background rate is a more challenging task. The high number of possible optical background sources hampers the declaration of a general quantitative assertion about the background rate, and ultimately it will have to be measured and minimized for a given species through adjustments in optical spectroscopy geometry and materials selection. Instead, we catalog some possible sources of background light and estimate their relative importance (see Table 2.4). Any scattered or reflected excitation laser light is expected to be sufficiently attenuated through

Table 2.4: Potential sources of optical background, with known excitation wavelengths.

Background	Location/Source	Wavelength	Note
Scattered light	Laser excitation	Species dependent	Attenuate with optical filter(s)
unreacted beam	Noble gas film	Species dependent	
Beam contaminant	Noble gas film	Species dependent	
N_2	Film/residual gas	<200 nm	Off resonance
N	Film/residual gas	523, 1047 nm [54]	Unknown concentration
O_2	Film/residual gas	763 nm [55]	1-nm FWHM, 24-ms lifetime
O	Film/residual gas	296, 558, 630 nm	Unknown concentration
H_2O	Film/residual gas	<200 nm	Off resonance
C	Film/residual gas	462, 872, 980 nm	Unknown concentration
Cr^{3+}	Sapphire impurity	693.0, 694.4nm [56]	Impurity in substrate

the use of optical filters. The primary sources of background light are expected to be contaminant atoms or molecules that, under the excitation wavelength of the product atom of interest, happen to fluoresce at wavelengths within the bandpass of the optical filters. These contaminants could be impurities in the substrate, noble gas film, vacuum windows, or optics. Furthermore, the beam can be contaminated by isotopes with similar charge-to-mass ratios, which will be implanted alongside the product atoms.

The overall background rate will be related to the sum of the fluorescence rates for all background sources. Assuming experimental conditions with excitation light at a 500-nm wavelength, with an intensity (power per unit area) of $P_\gamma/A_\gamma = 1\text{W/cm}^2$, the optical signal-to-background ratio S/B for one product atom with a $\tau = 5$ ns excited-state lifetime is approximately

$$S/B = \left[\frac{2\tau P_\gamma}{h\nu_\gamma}\sum_i n_i\sigma_0^i\left(\frac{\sigma^i(\nu_\gamma)}{\sigma_0^i}\right)\right]^{-1} \tag{2.1}$$

$$\approx 4\times10^{-14}\left[\sum_i n_i\sigma_0^i\left(\frac{\sigma^i(\nu_\gamma)}{\sigma_0^i}\right)\right]^{-1}, \tag{2.2}$$

where the sum is over all background species with areal density n_i, peak absorption cross section σ_0^i, and wavelength-dependent absorption cross section $\sigma^i(\nu_\gamma)$ at a laser frequency ν_γ, and h is the Planck constant.

Equations (1) and (2) state that S/B is inversely proportional to the areal number density n_i and the absorption cross section $\sigma^i(\nu_\gamma)$ of background species. The absorption cross section is

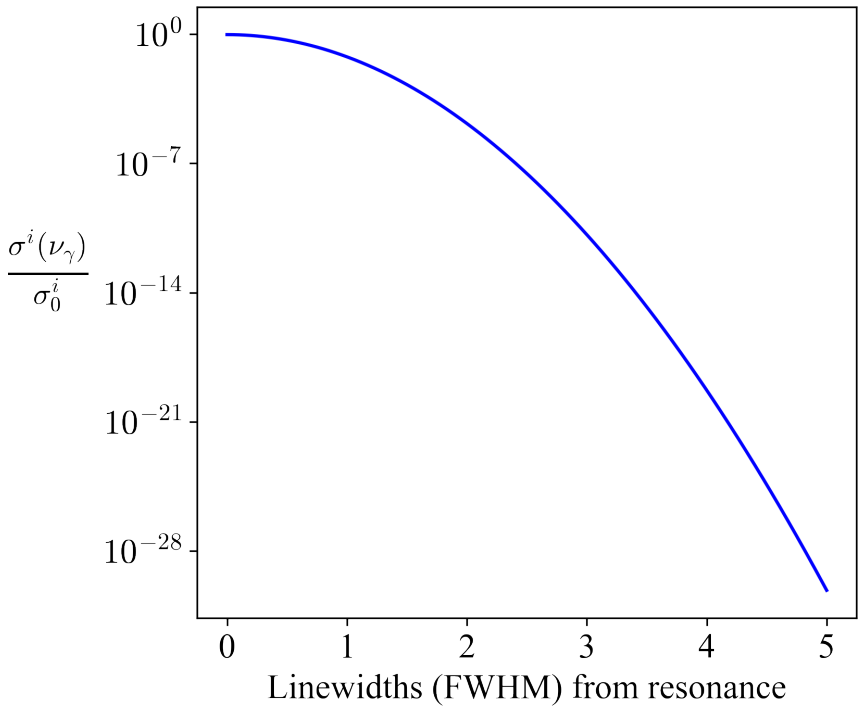

Figure 2.3: Off-resonance suppression factor $\sigma^i(\nu_\gamma)/\sigma_0^i$ for Gaussian absorption lineshapes. Far from resonance, the probability of excitation decreases exponentially, suppressing the probability of impurity fluorescence.

dependent on the in-medium lineshape factor, which is a function describing the probability of absorption as a function of the wavelength, and is typically Gaussian for matrix isolated species. Figure 2.3 illustrates the off resonance suppression factor as a function of the linewidths from the transition resonance, assuming that the in-medium lineshape remains Gaussian far from resonance. If the peak absorption wavelength of a background species is sufficiently far from the excitation wavelength, the background atom excitation rate will be exponentially suppressed. It is important to note that linewidths for absorption and emission are very broad in medium due to phonon excitation of the noble gas lattice, and are of the order of 10^3–10^4 GHz or roughly 1–10 nm, which is orders of magnitude larger than in vacuum.

As an example, the most abundant potential background source will be components of air trapped as impurities in the noble gas film. Noble gases are commercially available with ppm

purities and can be further purified to ppb levels with gettering. For an argon film of 100 μm thickness, there will be roughly 2×10^{20} argon atoms/cm^2, with 10^{14} molecules of air assuming a ppm purity. To achieve $S/B = 1$ would require an off-resonant suppression factor of roughly 10^{-28}, a distance of almost 5 linewidths from resonance for a Gaussian absorption lineshape. As the molecular components of air do not absorb until well into the ultraviolet, they are not expected to contribute significantly to the background rate, with the exception of O_2 near 763 nm.

2.4 Limitations and Summary

Several limitations exist for the SAM detection scheme. First, while atomic species can be selectively excited, this method is incapable of distinguishing between different isotopes of the same species. Although small isotope differences exist in the atomic hyperfine structure due to the nuclear spin, the linewidths in medium are so broad that any isotopic variation becomes obscured. Second, while this method is potentially applicable to a wide range of species, species without optically accessible transitions cannot be detected, which eliminates the noble gas elements along with elements like fluorine, whose lowest-lying transition occurs at 97.7 nm in vacuum. Third, it is not suited to detect products that are abundant in a vacuum system, such as oxygen, nitrogen, and carbon, as it would be impossible to grow a solid noble gas film without thousands of such contaminant atoms even with the highest achievable noble gas purity. Fourth, the detection mechanism is slow for the SAM relative to traditional methods since the products are not detected immediately after creation but, rather, at a later time when they are imaged. Therefore short-lived isotopes ($\tau_{1/2} < 1$ day) are not suitable unless the daughter nuclei are also optically detectable and the daughters are a different species from the beam atoms and any background atoms.

To summarize, important reactions for nucleosynthesis processes are often difficult to measure because of their low yield, whether it be due to extremely low cross sections, low-intensity rare isotope beams, or high background rates. We propose a novel detection method for low-yield nuclear reactions that captures the product atoms in a cryogenically frozen film of a solid noble gas where they are optically imaged and counted. This method can offer a near-unity capture and

detection efficiency, feasibly achieve single-atom sensitivity, and is potentially applicable to many astrophysically important nuclear reactions. The chief advantage of the single-atom microscope is that it is not sensitive to neutron, γ, or charged particle background sources and could, therefore, outperform traditional detection methods.

2.5 Acknowledgements

Special thanks to go Sam Austin, Artemis Spyrou, Hendrik Schatz, and Xiao-Dong Tang for helpful discussions. This work benefited from support by the National Science Foundation under Grant No. PHY-1430152 (JINA Center for the Evolution of the Elements). This work was supported by Michigan State University, the Director's Research Scholars Program at the National Superconducting Cyclotron Laboratory, and the U.S. National Science Foundation under Grant No. #1654610.

CHAPTER 3

THE PROTOTYPE SINGLE-ATOM MICROSCOPE

This chapter describes the design, construction, and performance of the prototype single-atom microscope (pSAM). The first section, 3.1, describes the design requirements and considerations for a low temperature cryostat with large optical access. Section 3.2 describes the construction and individual components of the prototype Single Atom Microscope (pSAM). Section 3.3 reports on the growth of thin films of solid Neon, Argon, and Krypton in pSAM.

3.1 Requirements

The pSAM has three fundamental design considerations. First, it should be capable of growing transparent thin films of solid noble gases on a cold substrate. Second, there should be access to the film surface for an external source (beamline) to embed the atomic species of interest into the noble gas film. Third, it should provide substantial optical access to the film for a charge-coupled device (CCD) camera-based imaging system.

3.1.1 Heat Load

A central requirement for the pSAM is the ability to grow and maintain thin films of solid noble gases. The freezing point of the noble gases increase with mass, as can be seen in Table 3.1 along with a number of other properties. Helium solidifies only under high pressure (0.95 Kelvin at 2.5 MPa [23]), and is therefore technically inaccessible for this purpose. Neon has the lowest freezing point among the noble gases used in pSAM, and requires temperatures in the single digits (Kelvin) at ultra-high vacuum (UHV, $< 10^{-7}$ Torr). Traditionally, cooling to low temperatures involved cryostat systems using liquid helium as a refrigerant [28]. The invention of the closed-cycle cryorefrigeration systems (cryocoolers) revolutionized many aspects of low temperature physics, as cryocoolers are capable of cooling to liquid helium temperatures without the materials expense and overhead of using liquid helium. Closed-cycle cryocoolers deliver long term, stable, and

Table 3.1: Properties of noble gas solids.

	Ne	Ar	Kr	Xe	ref
lattice structure	fcc	fcc	fcc	fcc	[23]
lattice constant (Å)	4.464	5.311	5.646	6.132	[24]
triple point (K)	24.56	83.81	115.78	161.37	[24]
ρ_{solid}, t.p. (g/cm^3)	1.444	1.623	2.826	3.399	[25]
T_{solid} (K, 10^{-6} Pa)	7.3	27.4	38.4	51.3	[26]
Sublim. energy (meV)	19.6	80	116	164	[27]
polarizability (Å^3)	0.394	1.641	2.484	4.044	[23]
refractive index	1.11	1.29	1.38	1.49	[28]

low maintenance cooling to liquid helium temperatures, and are therefore an ideal choice for this purpose.

Blackbody radiation is the main source of external heating in cryogenic vacuum systems as there is insufficient residual gas to conduct heat from the vacuum vessel to the cold parts. Cryostats and cryocoolers utilize thin-walled stainless steel for structural support, which similarly conducts a negligible amount of heat in the temperature range of interest. Achieving single digit temperatures at the sample location, in this case the substrate upon which the noble gas films are deposited, requires shielding from the walls of the vacuum vessel, which at room temperature are an intense source of radiative heat. The radiative heat flow between two surfaces is given by the Stefan-Boltzmann equation [1],

$$P_{rad} = \sigma E A (T_2^4 - T_1^4), \tag{3.1}$$

where $\sigma = 5.67 \times 10^{-8}\,\text{W/m}^2\text{K}^4$ is the Stefan-Boltzmann constant, A is the area (depending on the geometry) of the two surfaces, T_1 and T_2 are the temperatures of the two surfaces, and E is a factor depending on the emissivities of the two surfaces. The emissivity (ϵ) is a measure of how absorptive a material is to radiation (light) and is related to how reflective (R) a surface is by $\epsilon = 1 - R$. A perfect blackbody ($\epsilon = 1$) at $T = 300\,\text{K}$ has a radiative intensity of $\sigma(300\,\text{K})^4 = 46\,\text{mW/cm}^2$ onto the substrate and mounting fixtures at single digit temperatures. To be capable of growing solid neon films, the cooling system should have sufficient cooling power at temperatures below 10 K to offset the incoming blackbody radiation.

3.1.2 Beamline and Optical Access

Fluorescence photons from atoms captured on the substrate surface will be emitted isotropically, and so the optical signal size for detection will be proportional to the accessible solid angle around the sample. Imaging single atoms is more efficient if the imaging optics are placed close to the sample in order to maximize the number of fluorescence photons collected. Using large diameter viewports and lenses is likewise beneficial. The challenge becomes optimizing the distance and diameter so as to maximize the collection efficiency without adding significant heat load to the substrate. As a starting point, design of a vacuum chamber and substrate mount is intended for the single lens imaging solution displayed in Figure 3.1. In principle, the imaging can be performed with a single 50 mm diameter aspheric lens with an effective focal length of 40 mm (Edmund Optics No. 84-340). Creation of a 1:1 image on the CCD camera (Andor CLARA CCD), requires the substrate front surface to lens distance be equal to the lens to camera distance, which is twice the focal length (80 mm). The light collection efficiency for this setup is estimated by $\Omega/4\pi = (1 - \cos\theta)/2$, where θ is half the angle occluded by the lens. In this case, $\tan\theta = 25\,\text{mm}/80\text{mm}$, resulting in a light collection efficiency of roughly 2.3%. In contrast, a typical optical cryostat has efficiencies around 0.1% or lower [50].

Unimpeded access to the front surface of the substrate is essential for achieving unity capture efficiency of recoiling product atoms. However, it is difficult to imagine a single chamber design which features the requisite beamline access and good optical access to embedded atoms without significant compromise. Optical cryostats for similar applications angle the substrate between the viewports and sample deposition port as a compromise [57]. Instead, a two-chamber design was chosen to ensure ideal accessibility for both, with the substrate mounted on a linear drive for transfer between chambers. This will allow for the design of an imaging chamber with ideal optical access without obstructing atom implantation.

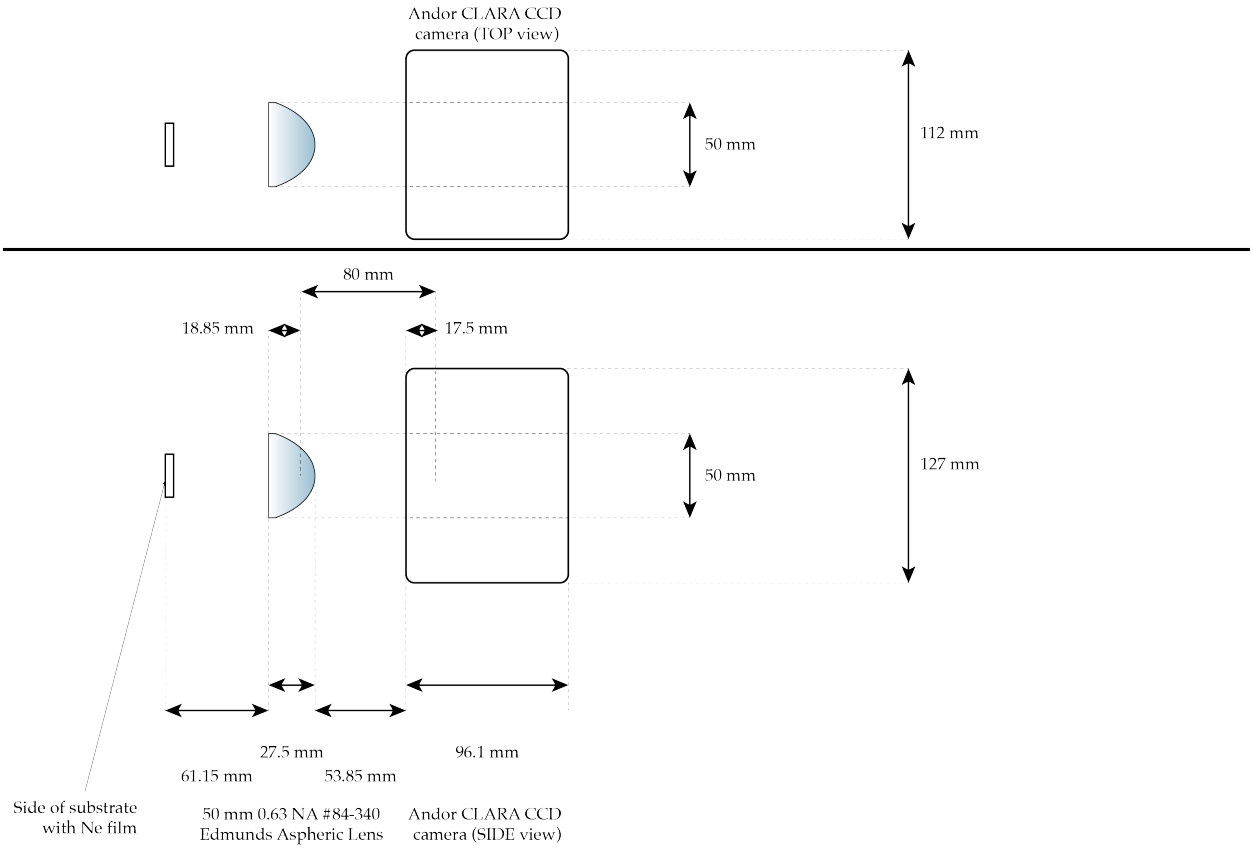

Figure 3.1: Top-down and side-view of the optical imaging system for creating a 1:1 image of the substrate on the Andor Clara CCD camera sensor with a solid angle efficiency of 2.3%.

3.2 Components

3.2.1 Overview

At the heart of pSAM is a pulse tube cryocooler, necessary for cooling a substrate to the cryogenic temperatures required to solidify noble gases. The substrate is clamped to a copper substrate mount attached to the cryocooler and surrounded by a cooled copper shield assembly in order to block most blackbody radiation from the room temperature vacuum vessel walls. The cryocooler itself is mounted on a linear drive (linear shift mechanism) used to position the substrate in either the growth or imaging chamber. The linear drive is mounted on top of the growth chamber, where noble gas films are grown and product atoms are embedded. The growth chamber features viewports for monitoring during sample growth and also contains the turbomolecular vacuum pump and vacuum

sensors. The imaging chamber is mounted below the growth chamber and is of custom design, featuring large diameter viewports in close proximity to the substrate. Figure 3.2 and 3.3 contain a rendering of the pSAM model and a picture of the detector.

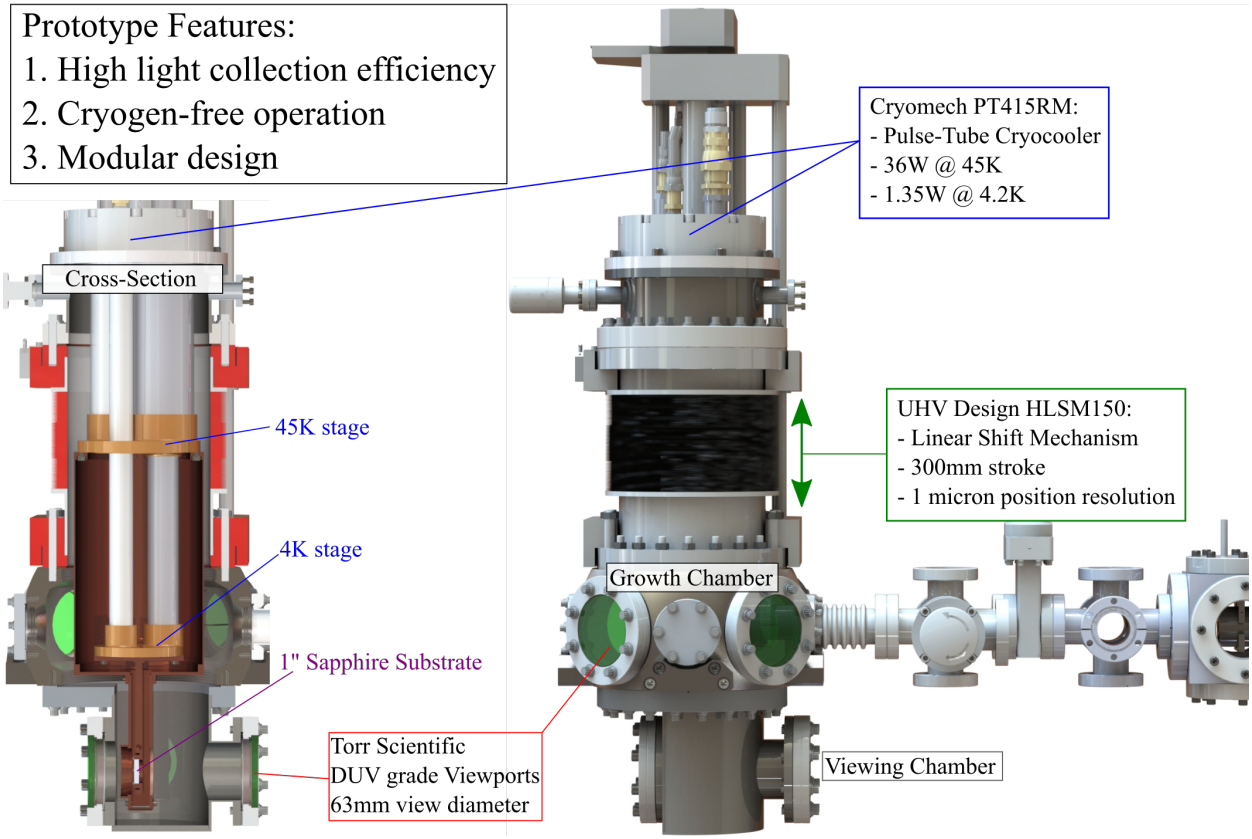

Figure 3.2: A rendering of the original prototype Single Atom Microscope design. left: exterior of pSAM with an atomic source attached. The cryocooler is mounted on a linear drive, capable of positioning the substrate in the upper 'growth' position or lowering it into the 'imaging' position. right: cross section of pSAM, showing the two stages of the cold head and the substrate in the 'imaging' position. The substrate is positioned close to a large 2.5" viewport to maximize the light collection efficiency.

3.2.2 Assembly and Cleaning Protocol

It is good practice to thoroughly clean all vacuum components before assembly. Components are often contaminated with oils from fabrication and handling that outgas under vacuum and limit the ultimate vacuum pressure. Furthermore, any impurities captured in a film or contamination on the substrate has the potential to be a significant source of background light under laser excitation. The

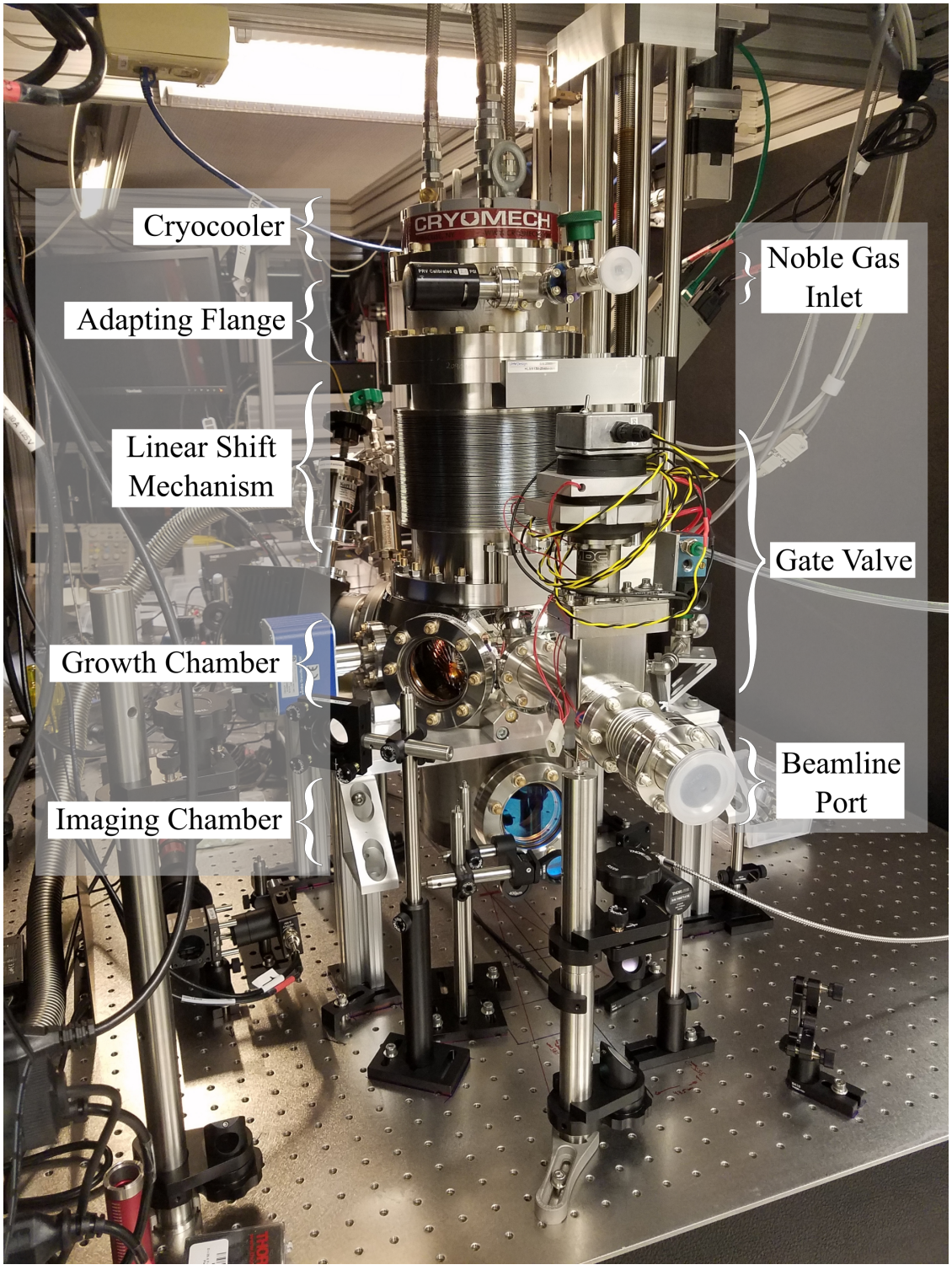

Figure 3.3: A picture of the assembled pSAM while mounted to a laser table in the Spinlab at the NSCL. An array of optics can be seen in front of the imaging chamber for directing laser light through the substrate.

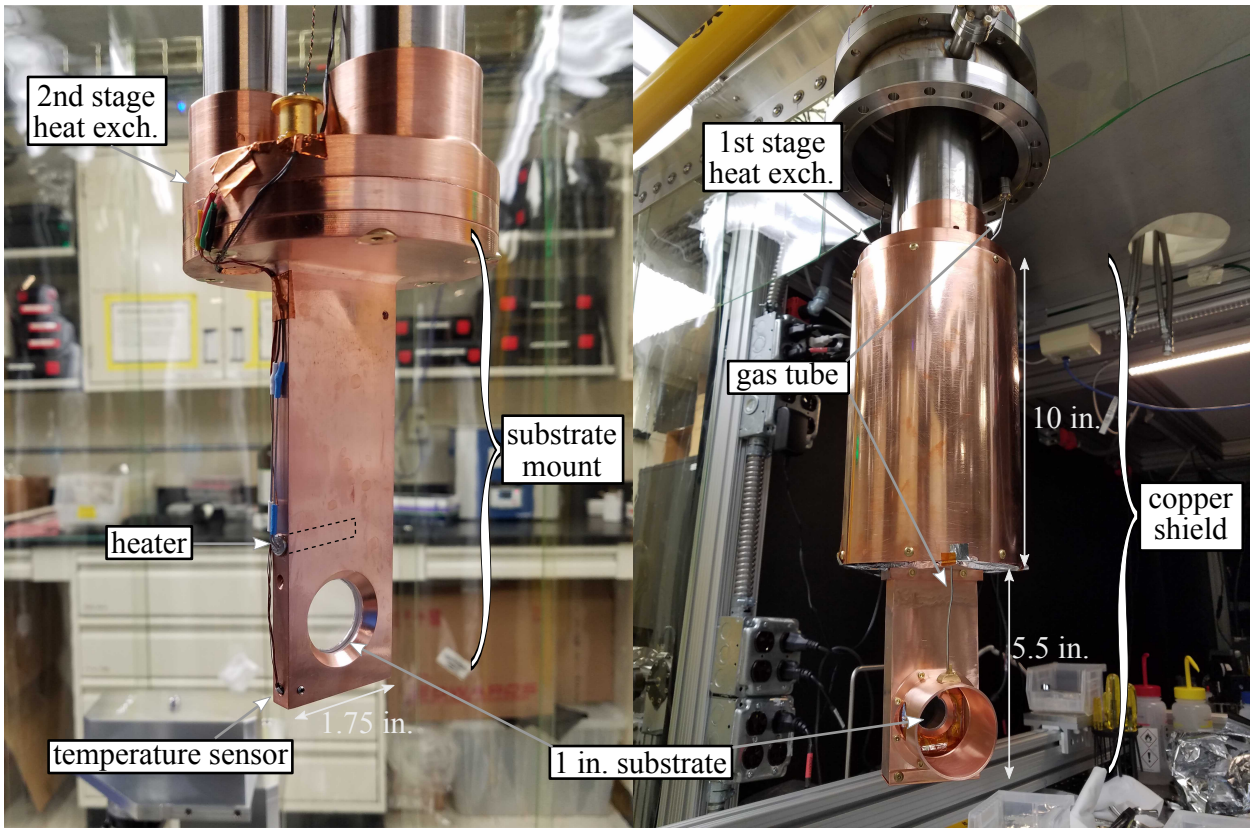

Figure 3.4: *left panel.* Picture of the pSAM substrate mount as attached to the 2nd stage heat exchanger. A heater and temperature probe can be seen on the left side, with wires secured to the mount and heat exchanger with copper tape to best ensure thermal grounding. This thermal grounding ensures the wires are at the same temperature as the substrate mount, which prevents any erroneous readings due to heat conduction along the wires. The heater is quite long, and extends 1 inch into the substrate mount as outlined by a dashed line. *right panel.* Nearly fully assembled pSAM cold head structure. The 1-inch diameter substrate is visible through the hole near the bottom of the copper shield assembly, as is the thin gas tubing (1/16" OD) for depositing the noble gases on the substrate surface. Aluminized mylar shielding has not yet been applied to the outer copper shield in this picture except in one small spot. The substrate has mount has been shielded with aluminized mylar (barely visible). See also: Appendix C for more pictures of the cold head.

pSAM components were cleaned before assembly by hand cleaning all surfaces first with acetone, and then with isopropyl alcohol. Afterward, they were submerged in an ultrasonic cleaner for one hour at 60° Celsius, rinsed with distilled water, and left to air dry in a clean area. Assembly of pSAM was performed in a Class-100 cleanroom to minimize the amount of dust and particulates as well as minimize the chance for surface contamination inside the vacuum vessel.

3.2.3 Cryocooler and Cold Components

The pSAM cryocooler is a Cryomech PT415 Cryorefrigerator [58], which is two-stage Pulse Tube type cryocooler with a cooling power of 40 Watts at 45 Kelvin and 1.5 Watts at 4.2 Kelvin at its first and second stage heat exchangers, respectively (see Figure 3.6). The theory of operation and specific details of the cryocooler 'cold head' (main body of the cryorefrigeration system, separate from the compressed helium gas system) are detailed in Appendix B. The noble gas films are grown on the surface of a substrate that is mounted to the 2nd stage heat exchanger on the cold head. The substrate mount, pictured in the left panel of Figure 3.4, is machined from a block of oxygen-free electrolytic (OFE, C10100 Copper Alloy) copper, which is a commonly used material in cryogenic applications due to its exceptional thermal conductivity at low temperatures. The substrate itself is synthetic sapphire, which has both excellent optical qualities and among the highest thermal conductivities of any material at low temperature. Table 3.2 contains properties about various materials used in pSAM at cryogenic temperatures. The substrate is firmly clamped to the substrate mount with a copper ring, and a layer of indium metal is used as a gasketing material to improve thermal contact with the substrate mount. Indium also has excellent cryogenic properties and is a very soft metal, making it ideal for this purpose. Firmly clamping the substrate to its mount with Indium as a gasket effectively cold-welds them together, filling in any gaps or irregularities between the mating surfaces [1]. A cross section of two different substrate mounts that have seen use in pSAM is included in Figure 3.5.

A shielding structure made of several copper parts is constructed around the 2nd stage of the cold head, including the substrate mount, and is pictured in the right panel of Figure 3.4. This shield is

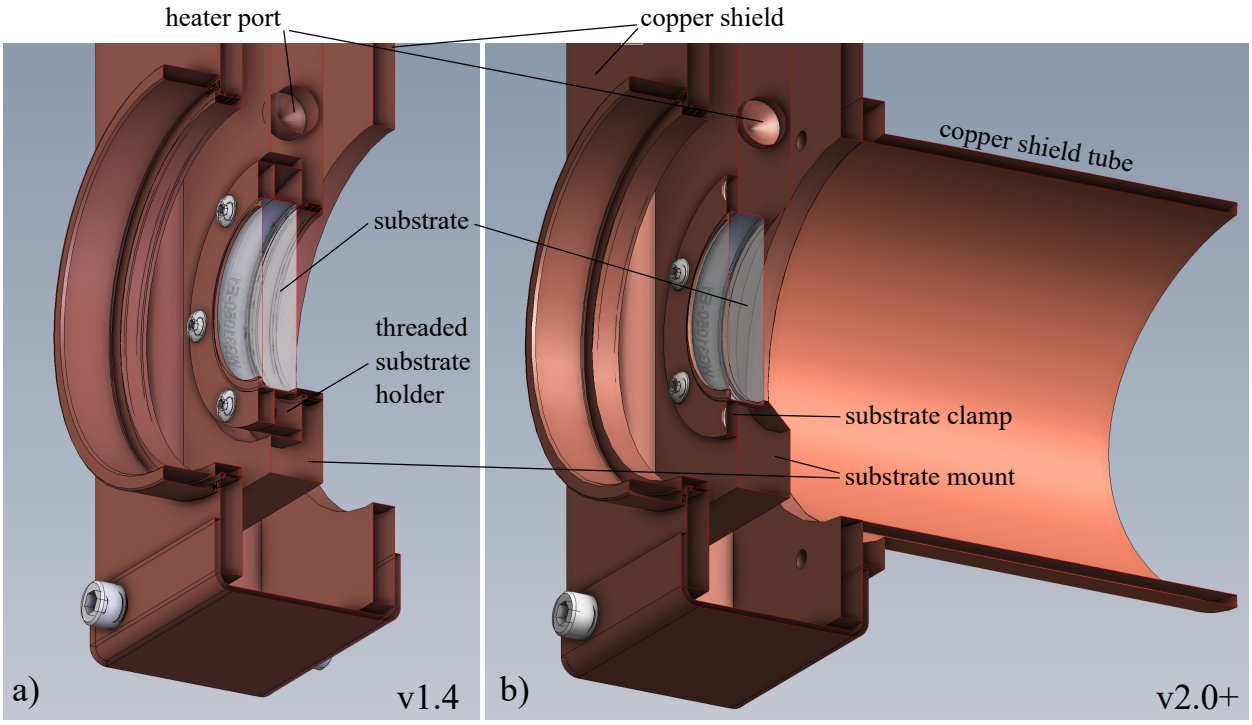

Figure 3.5: a) Original pSAM substrate mount, which utilized a removable threaded copper substrate holder to make it easier to install and remove the substrate. However, the threads were found to poorly conduct heat at low temperatures and limited the ultimate substrate temperature unless cryogenic vacuum grease (Apiezon-N) was applied during installation. b) Current substrate mount that clamps the substrate directly to the mount, eliminating the need for Apiezon-N application. Indium wire is applied as a gasketing material at each substrate-copper interface. Also featured is the copper shield tube to reduce blackbody irradiation on the front substrate surface.

thermally anchored to the 1st stage heat exchanger and completely covers the substrate mount except for a pair of 2 in diameter holes centered on either side of the substrate to allow for good optical access. The purpose of this shield is to protect the 2nd stage from blackbody radiation emanating from the enclosing vacuum vessel, which is at room temperature. Assuming a perfect blackbody ($\epsilon = 1$), the pair of 2 in diameter holes allow a radiative power of $(46\,\mathrm{mW/cm^2}) \times (2) \times (20\,\mathrm{cm^2}) = 1.84\,\mathrm{W}$ through the shielding,

To further reduce the effect of blackbody, a layer of aluminized mylar is taped to the surface of the substrate mount and the outside of the shielding structure. Aluminized mylar is a thin layer of plastic sheeting that has been coated with aluminum on one side. The aluminum is very reflective (emissivity ≈ 0.01 [1]) compared to the unpolished copper substrate mount (emissivity > 0.02 [1]),

Table 3.2: Table of material properties. Values taken from [1].

	Thermal conductivity W/(m·K)		Specific heat J/(g·K)		Thermal contraction $\Delta L/L$ (%)
	4 K	295 K	4 K	295 K	293K – 4 K
Brass	2	86	0.00015	0.377	0.384
Copper OFHC	630	397	0.00009	0.386	0.324
Stainless steel	0.27	15	0.00017	0.48	0.296
Polyimide (Kapton^{TM})	0.011	0.19	0.00079	0.755	0.44
Sapphire	230	47	<0.00009	0.779	0.079

reducing the amount of blackbody radiation absorbed by the substrate mount. The combination of the copper shield structure and aluminized mylar shielding allows for optical access and the substrate mount to reach temperatures below 6 K, which is cold enough to grow films of solid Neon. The heavier noble gases' temperature requirements are much easier to achieve. The next lowest freezing point is for Argon at 27 K, where the cooling power of the cryocooler is improved to tens of Watts. A plot of the cooling capacity of the cryocooler is included in Figure 3.6, and the pressure and temperature inside pSAM during a typical cooldown from room temperature is included in Figure 3.7

3.2.4 Temperature Control

Monitoring and controlling the temperature is done with a temperature sensor and heater mounted to the substrate mount (pictured in Figure 3.4). The sensor type is a Cernox resistor (Lakeshore Model CX-1050-AA, SN:X103297) and provides a temperature measurement via its temperature dependent electrical resistance. It is calibrated over the range of temperatures from 1.4 – 325 K, with an uncertainty of less than 20 mK at temperatures below 50 K. The temperature sensor is mounted in a hole on the bottom end of the substrate mount, below the substrate. This location is furthest from the 2nd stage heat exchanger and nearby the substrate, where the temperature reading should be close to the actual substrate temperature. Measuring the substrate temperature directly is not done in pSAM due to the difficulty of mounting a temperature probe without contamination

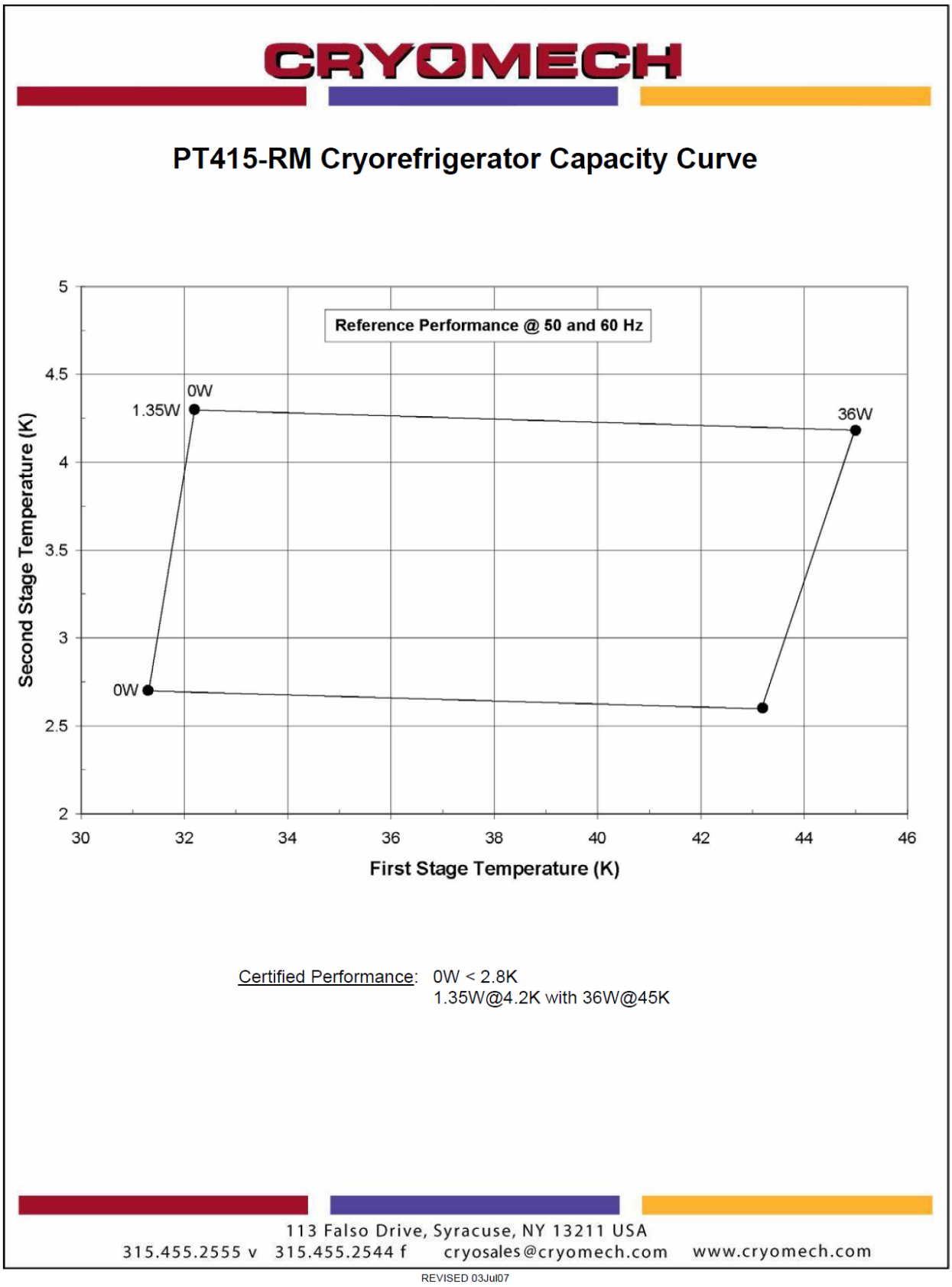

Figure 3.6: Advertised cooling power capabilities of the pSAM cryoocoler.

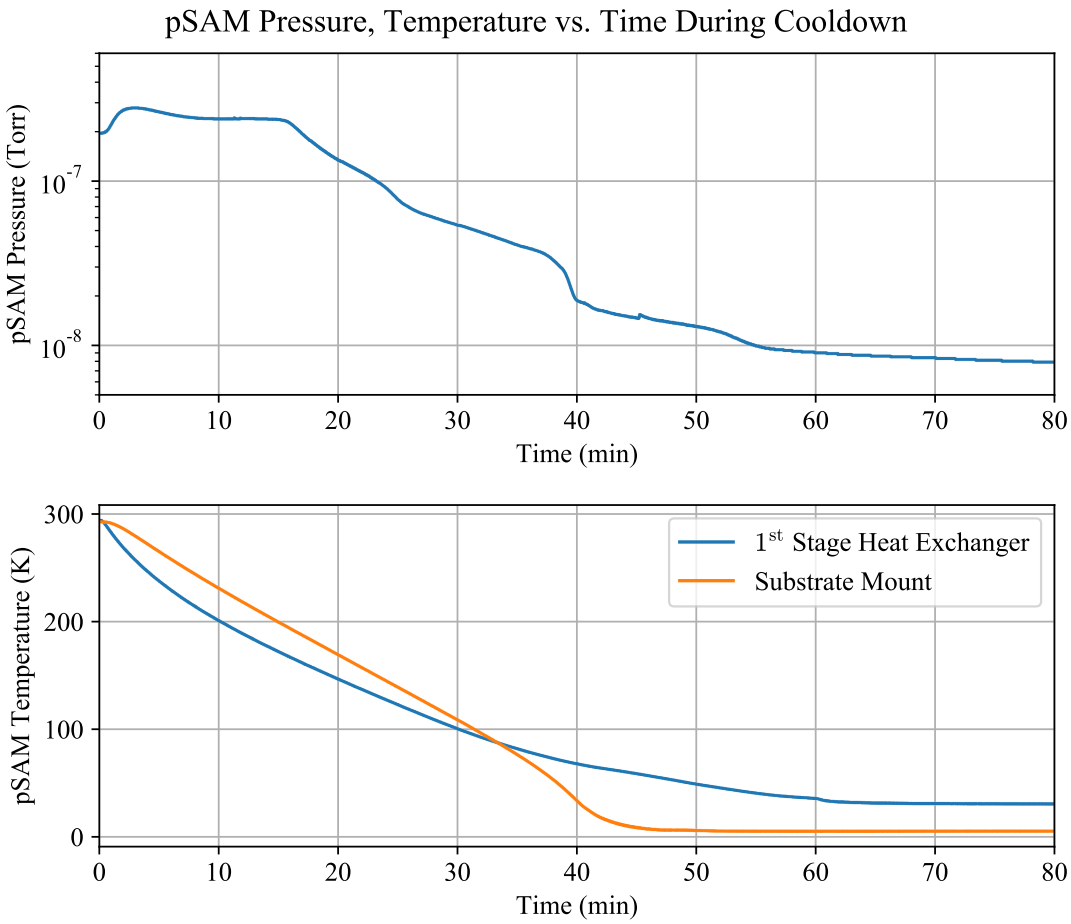

Figure 3.7: Pressure and Temperature measured inside pSAM as a function of time relative to cryocooler start. The pressure initially increases as the top of the cold head gets hot as heat is pumped out of the cold components, leading to increased outgassing. The substrate mount is cooled below 6 K in 50 minutes, but it takes roughly 70 minutes for both stages to stabilize.

or obstruction of the substrate. Another Cernox sensor (Lakeshore Model CX-1050-CU-HT, SN:X134596) is mounted to the 1st stage heat exchanger for diagnostic purposes. The temperature sensor calibration data is included in Appendix C.

The heater is an 50 Ohm resistor in a cylindrical housing (Lakeshore part number HTR-50) that is used to raise the temperature of the substrate mount by simply sending current through it. The heater is mounted just above the substrate, a distance of 3 inches from the 2nd stage heat exchanger. The heater cartridge is quite large (1/4 inch in diameter, 1 inch long), penetrating more than halfway into the substrate mount. This placement of the heater ensures that the temperature

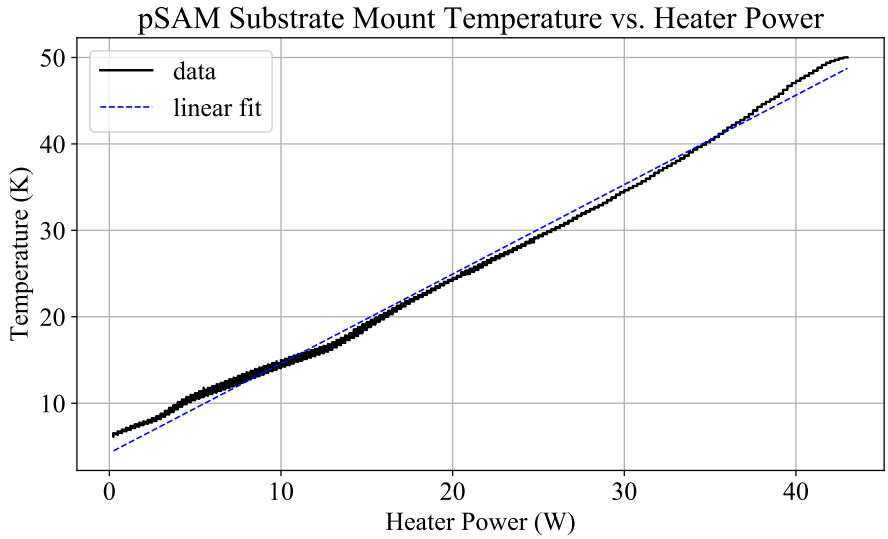

Figure 3.8: Plot of Temperature vs. Heater power as read by the substrate mount temperature sensor. Relation is reasonably well represented by a linear fit with a slope of 1 K/W.

of the mount around the substrate is uniform, since the heat source is between the substrate and the source of cooling (2nd stage heat exchanger). Sending current I through the heater with resistance R injects heat energy into the substrate mount at a rate of $P = I^2R$, where P is the power in Watts. A temperature is maintained when the total heat load is matched by the cooling power of the cryocooler.

The temperature sensors and heater are wired to an electrical vacuum feedthrough flange that is externally connected to a Lakeshore Model 331 Temperature controller. The Lakeshore 331 measures the resistance of each temperature sensor and converts to a temperature with each sensor's unique calibration curve. It also is capable of sending up to 1 Amp of current through the heater, corresponding to a maximum power of 50 Watts. A plot of the substrate mount temperature as a function of heater power is included in Figure 3.8. The Lakeshore 331 can be set to maintain a specific temperature through the use of a Proportional-Integral-Derivative (PID) control algorithm, which adjusts the heater power automatically to maintain a specific temperature. Altogether, with the temperature control system, the temperature of the substrate mount can be set to any temperature in the range from 5 - 60 K.

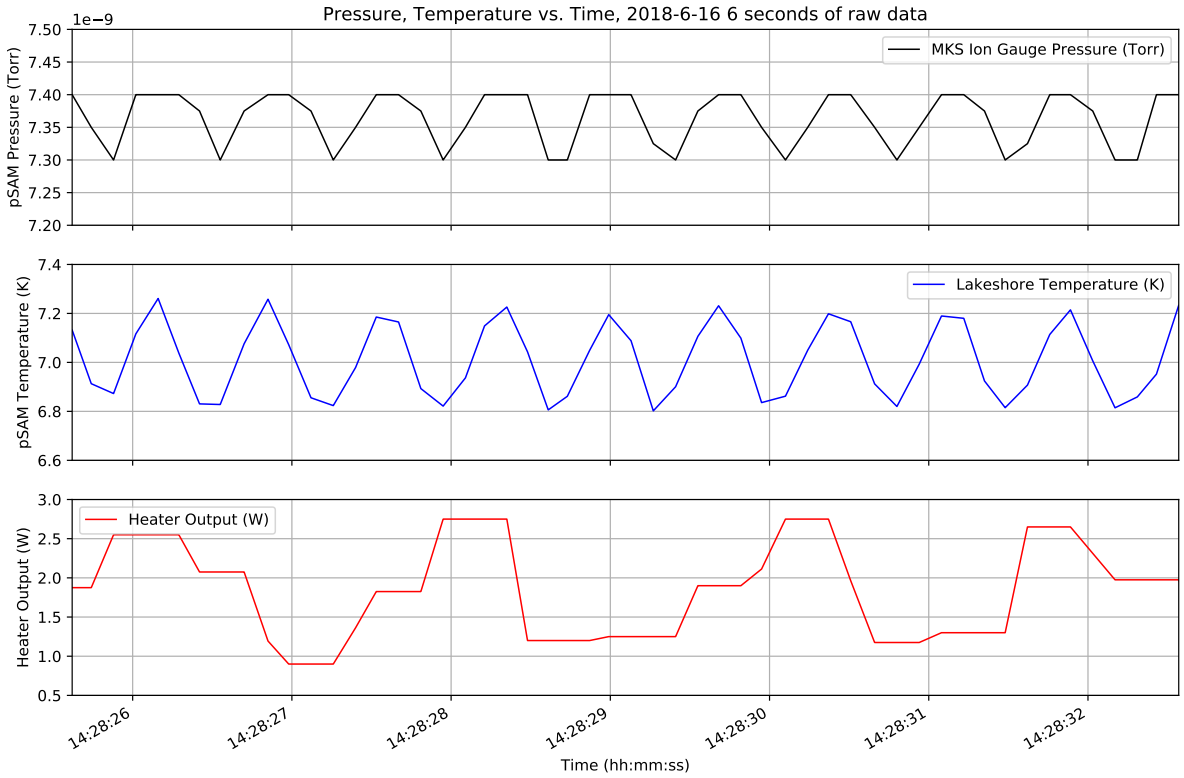

Figure 3.9: Plot of pSAM pressure, substrate mount temperature, and heater power over a period of 6 seconds. The oscillation in temperature (middle trace) is clearly evident, as well as a corresponding oscillation (top trace) in pressure associated with a variation in vapor pressure for residual gases frozen on the cold parts. The bottom trace shows the Lakeshore temperature control is unable to vary the heater fast enough to counteract the oscillation.

The cryocooler cooling power is created by cycling between high (280 psi) and low (100 psi) pressures of compressed helium at a frequency of roughly 1.4 Hz. This oscillatory behavior of the cooling power manifests itself in an observable temperature oscillation below 20 K. At such low temperatures, the specific heat of copper falls drastically, so the small oscillation in heat energy corresponds to a noticeable temperature oscillation. This oscillation is depicted in Figure 3.9, which shows the automated heater corrections (controlled by the Lakeshore 331) are insufficiently fast to accommodate the rapid swings in temperature, which reach a maximum amplitude of nearly 1 degree K near 10 K. This temperature variation is not expected to significantly affect spectroscopy of samples deposited on the substrate. However, should it prove necessary, it is possible to damp the oscillations by increasing the total thermal mass or installing a large heat capacity spacer between

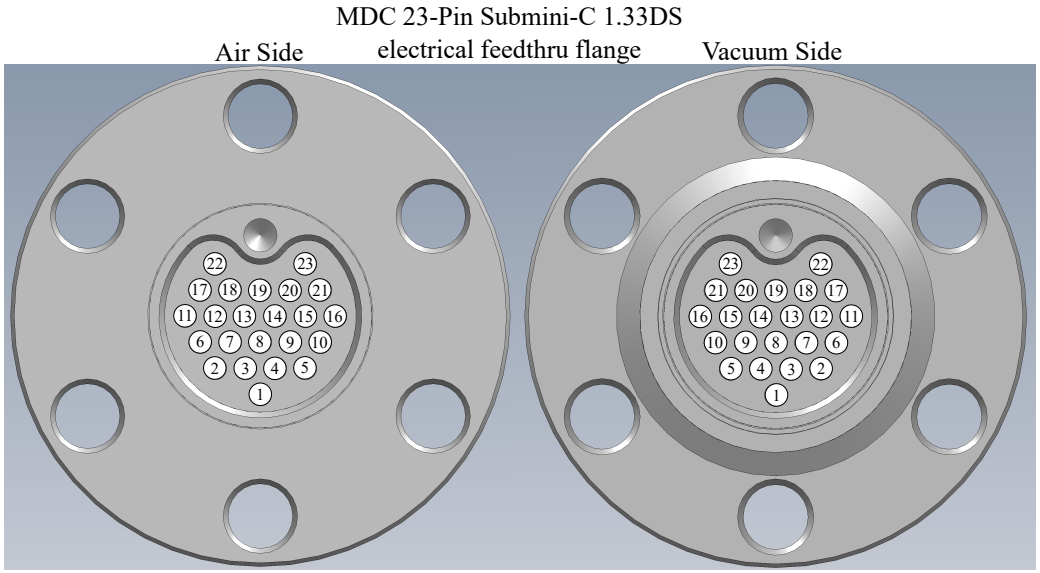

Figure 3.10: Pinout of electrical feedthrough flange on pSAM, denoting pin assignments for the heater and temperature probe leads.

the substrate mount and 2nd stage heat exchanger. A layered spacer of lead and copper has been shown to damp the oscillations to the milliKelvin scale [59].

3.2.5 Feedthrough Vacuum Access

External access to the interior of pSAM is provided through a set of feedthrough flanges attached to an adapting flange between the Linear Shift Mechanism and cold head flange near the top of pSAM. The stainless steel capillary tubing (1/16" OD, 0.04"ID) used to deposit noble gases on the substrate surface is connected to a 1/4" stainless steel feedthrough tube on a 1.33" ConFlat (CF) flange (Lesker part: LFT212TEFV). The sections of stainless steel tubing are connected with custom fittings that are silver soldered (brazed) to the tubing. The fittings are fastened together with brass screws and an indium o-ring seal is compressed between the fittings to ensure a leak-tight seal even at low temperature. The noble gas feedthrough tubing is externally sealed with a stainless bellows valve (Swagelok part SS-4H). The noble gases flow through this inlet valve from a separate gas handling vacuum system, described later in this chapter.

A pressure relief valve on a 1.33" CF flange is also fitted to the adapting flange as a safety

measure in case of rapid sublimation of large amounts of frozen gases inside pSAM. The pressure relief valve (Accu-Glass Model PRV-133) is designed to open at when the internal pressure exceeds 2 psi above atmosphere, thereby preventing a hazardous overpressurization situation. The electrical feedthrough flange (MDC 23 Pin Submini-C 1.33DS) for the temperature sensors and heater is also attached to the adapting flange.

3.2.6 Linear Shift Mechanism and Position Control

As mentioned in the overview, the cold head and adapting flange are mounted to a UHV Design HLSM150 Linear Shift Mechanism (LSM), which is capable of 300 mm of linear motion (300 mm stroke). The purpose of the LSM is to move the substrate between the growth and imaging chamber, described in subsequent sections. The LSM consists of an expandable edge-welded bellows assembly with 8" CF flanges supported in a kinematic guide system. Linear expansion or contraction of the bellows is driven by a McLennan stepper motor (23HT18C230) fitted to a 50:1 IP57 gearbox, which drives a precision stainless steel trapezoidal lead-screw (with 2 mm pitch). Control of the LSM position is done through a Mclennan Sim-Step stepper motor drive and controller, which utilizes a Mclennan PM1000 motion controller to command a MSE570M microstepping bipolar stepper motor drive. The Sim-Step is operated through a command line interface and is capable of precisely translating the LSM throughout its full stroke range at adjustable speeds, along with execution of user-defined motion sequences.

The stepper motor divides a full revolution into 200 steps, which is improved by the MSE570M drive which implements a microstepping (μstep) resolution factor of 16, thereby dividing a full rotation into 3200 μsteps. The stepper motor drives a 50:1 gearbox coupled to the 2 mm pitch lead-screw (2 mm per revolution), which propels the actual expansion and contraction of the LSM. Converting steps to LSM displacement is a straightforward calculation:

$$\left(\frac{200\,\text{steps}}{1\,\text{rev}}\right)\left(\frac{16\,\mu\text{step}}{1\,\text{step}}\right)\left(\frac{50\,\text{rev}}{1\,\text{screw rev}}\right)\left(\frac{1\,\text{screw rev}}{2\,\text{mm}}\right) = 80,000\,\frac{\mu\text{steps}}{\text{mm}} \tag{3.2}$$

This corresponds to 12.5 nm/μstep, well beyond the resolution of the Renishaw LM10 magnetic

encoder attached to the LSM for precision position measurements. The LM10 has a resolution of 1 μm, corresponding to 80 μsteps or 5 motor steps. Positioning the LSM repeatably with micron precision is typical with this setup although the position has been observed to drift as far as 10 μm over a period of a week, likely due to thermal contraction and expansion. Refer to Appendix D for a list of common commands used in controlling the LSM.

3.2.7 Growth Chamber

The growth chamber is an 8" ID spherical square design commercially available from Kimball Physics, with four 4.5"CF and four 2.75"CF ports. A cross section of the growth chamber is included later in Figure 3.15. Two 4.5"CF ports are occupied by a pair of large diameter fused silica viewports (2.5" view diameter) from Torr Scientific Ltd on opposing sides of the substrate at a 45-degree angle, for the purpose of monitoring noble gas film growth, a process described later in the Performance section of this chapter. One 4.5"CF port is occupied by a vacuum pump, and two 2.75"CF ports by vacuum sensors. The beamline port (2.75"CF), directly in-line with the front surface of the substrate, is sealed with a pneumatically actuated MDC gate valve (GV-1500M-P) on a 2.75"CF flange for isolation from the beamline. The additional ports in the growth chamber are unused.

3.2.8 Vacuum control

The vacuum pump system consists of an Oerlikon TurboVac 50 turbomolecular pump (55 l/s), with an Anest Iwata 250C oil-free scroll pump (9.1 CFM displacement) for rough vacuum. Vacuum pressure is monitored with an MKS Series 392 Micro-Ion Gauge, accurate for pressures ranging from 10^{-9} – 760 Torr. In addition, pSAM features an SRS RGA200 Residual Gas Analyzer (RGA) for vacuum diagnostics and noble gas partial pressure measurements. The RGA is capable of measuring the partial pressures of residual gases in pSAM in the pressure range of $10^{-4} - 10^{-10}$ Torr (10^{-6} – 10^{-12} Torr with the electron multiplier on). The RGA functions by ionizing residual gas atoms and molecules with a hot filament and separating them based on the mass-to-charge (m/q)

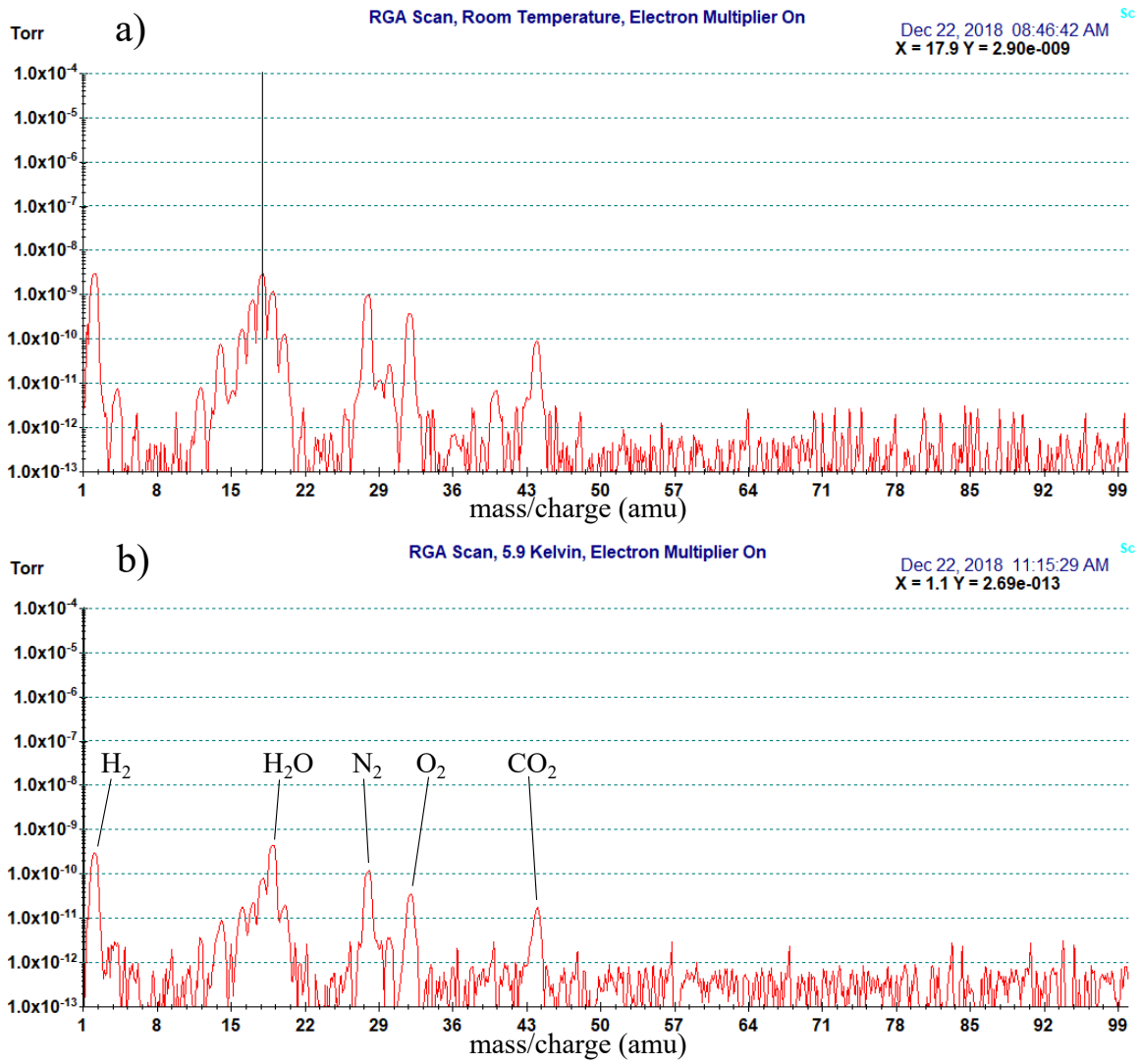

Figure 3.11: Typical partial pressure as a function of mass/charge as measured by the RGA with pSAM at room temperature (top), and with the substrate mount at 5.9 K (bottom). With the cryocooler at base temperature, the pressure is reduced by an order of magnitude relative to room temperature. The principle peaks of the residual gases are labeled in the bottom plot.

ratio. The SRS RGA200 is sensitive in the range from $m/q = 0 - 200$ amu, although typically no peaks are detected above the background for $m/q > 86$, which is the heaviest stable isotope of Krypton. Typical RGA scans for pSAM at room temperature and at base temperature are displayed in Figure 3.11. Partial pressure measurements can also be performed during film deposition, where the scan is dominated by the noble gas being deposited, as displayed in Figure 3.12.

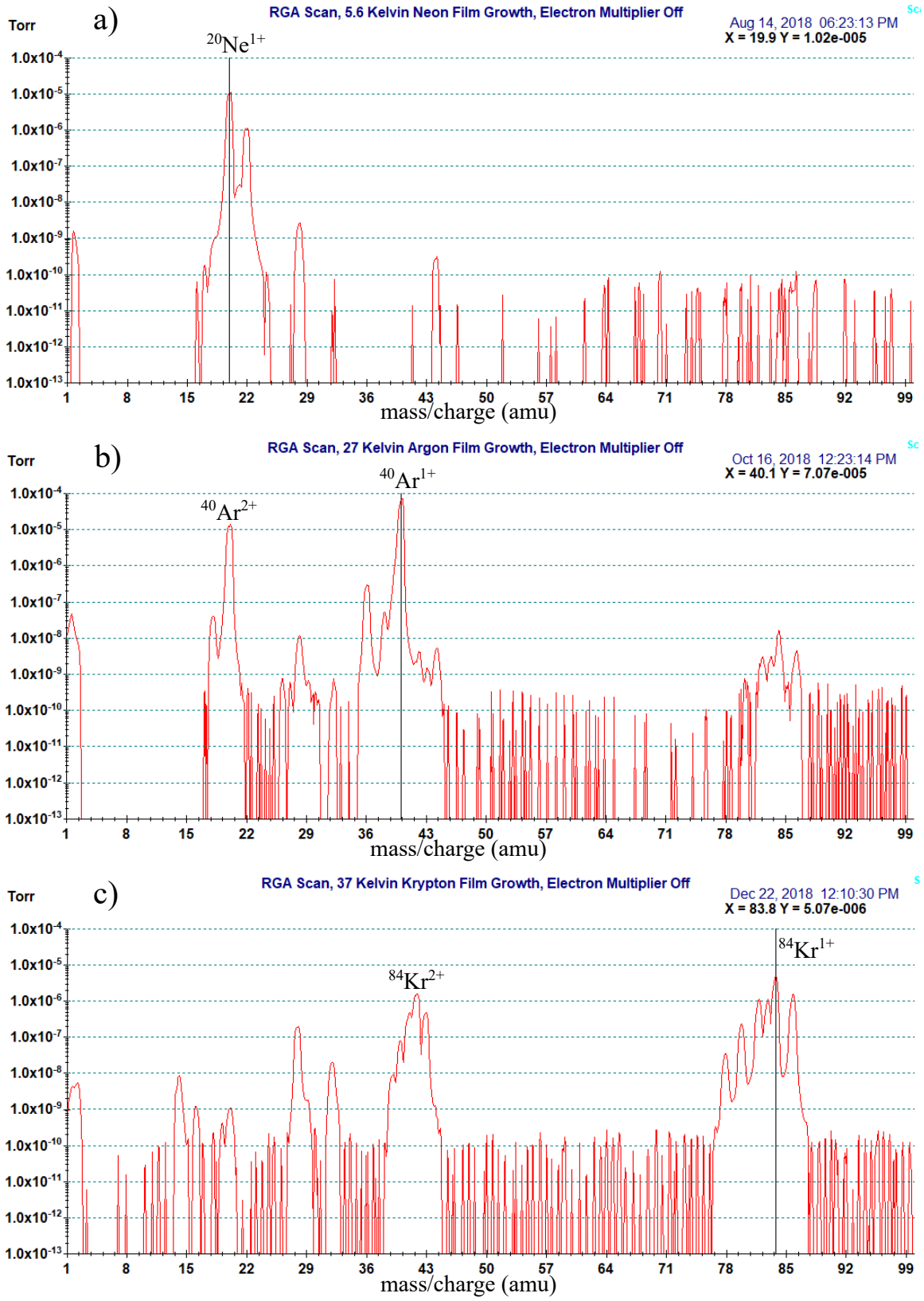

Figure 3.12: RGA scans taken during noble gas film growths, where the naturally abundant isotopes of neon, argon, and krypton dominate the scans.

3.2.9 Imaging Chamber

The imaging chamber features two large fused silica viewports (2.5" view diameter) from Torr Scientific Ltd with an anti-reflective coating (part VPZ64QBBAR, 700-1100 nm) mounted to 4.5"CF ports on either side of the substrate. The vacuum chamber was designed with a "D"-shaped cross section with the flat section parallel to the substrate, and is detachable in case a new design is required. The rear viewport is positioned just 1.5" from the front (noble gas film) side of the substrate, corresponding to approximately 10% total solid angle efficiency out of the rear viewport from the center of the substrate.

3.2.10 Gas Handling System

The purpose of the gas handling system is to transfer noble gases from a compressed gas cylinder to pSAM in a controlled fashion and at the highest purity. A diagram of the system is included in Figure 3.13. The noble gases used are of research grade purity, purchased from Praxair (Neon 99.999%, Kr 99.999%) and Airgas (Argon 99.998%). The gas cylinders are fitted with a standard dual-stage regulating valve (Matheson 3120A) and connected to a noble gas purifier (SAES GC50 Purifier) which is capable of reducing impurities in the noble gases to concentrations below 10 parts per billion (ppb), or 99.99999% purity. The purifier was bypassed with isolating and bypass valves for the majority of film growths described in this thesis. The noble gases then flow through an electronically controlled needle valve (Pfeiffer EVR116 control valve) into the main buffer volume, which is a 2.75" Conflat (CF) 6-way cross. Mounted to the buffer volume is the vacuum pump system (Oerlikon TurboVac 50 with Edwards nXDS10i forevacuum pump), which can be isolated from the buffer volume with an angle valve (Lesker SA0150MCCF). Pressure in the buffer volume is measured with a cold cathode ionization vacuum sensor (HPS Series 423 I-MAG) valid in the range 10^{-11} – 10^{-2} Torr, and a capacitance manometer (MKS Baratron 626C) that is accurate in the range 0.1 – 100 Torr. The cold cathode sensor is powered off during film growth for protection.

After the buffer volume, the gas flows through a liquid nitrogen cold trap to freeze out water vapor present in the gas. The cold trap consists of a long 1/4" diameter stainless steel tube (approx

5 meters in length) coiled to fit inside a dewar filled with liquid nitrogen. The gas completes the journey to pSAM through a section of flexible tubing that is connected to a gas inlet flange, located near the top of pSAM. Once through the pSAM inlet valve, the gas enters a long capillary tubing (1/16" OD, 0.04" ID, approximately 20" in length) starting at the inlet, passing inside the copper shielding, and ending approximately 2 cm from the substrate surface. The capillary tubing is thermally isolated from the shielding itself to ensure its temperature remains high enough to prevent noble gases (Argon and Krypton in particular) from freezing inside the tubing and clogging it.

Gas flow into pSAM is controlled via computer, which reads the pressure inside the buffer volume with the Baratron 626C and adjusts the Pfeiffer control valve in order to maintain a specifically set pressure with a PID algorithm, similar to the temperature control described previously. The pressure differential between the purifier section and the buffer volume causes gas to flow into the buffer volume at a rate controlled by the Pfeiffer valve. The pressure differential between the buffer

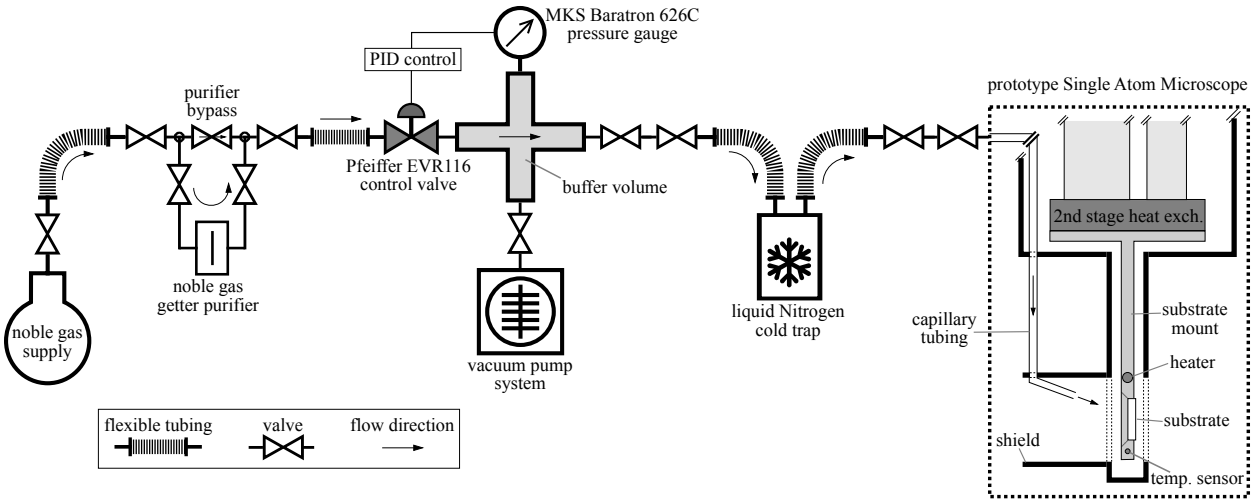

Figure 3.13: Diagram of the gas handling system used to deposit noble gases onto the substrate in pSAM. The general direction of flow is from left to right, and starts at a cylinder of research grade (99.999% purity) noble gas. After flowing through an optional purifier, it enters a buffer volume through an electronically controlled valve. The noble gas subsequently passes through a liquid Nitrogen cold trap for further purification (removal of water vapor) before entering pSAM, where it flows through a stainless steel capillary tubing ending approximately 2 cm from the surface of the substrate. During a film growth, the valve to the vacuum pump system is closed.

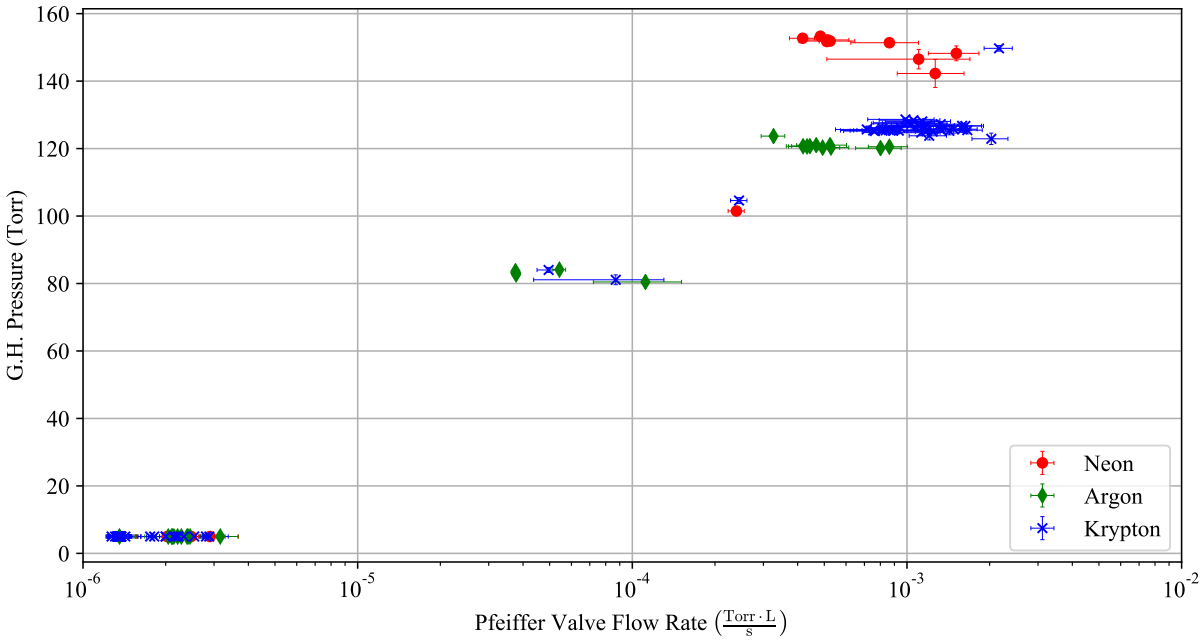

Figure 3.14: Plot of the Gas Handling buffer volume pressure as a function of Pfeiffer valve flow rate setting during a collection of neon, argon, and krypton film growths. The units for the Pfeiffer Valve flow rate are not the actual gas flow rate (Torr L/s) through the Pfeiffer valve, but rather the flow rate setting used to control how open the valve is. The actual flow rate through the Pfeiffer valve has been measured to be roughly a factor of 20 higher, and strongly depends on the difference in pressure across the valve and is related to the noble gas cylinder regulator setting (typically 18 – 20 psig).

volume and pSAM causes the gas to flow through the cold trap, capillary tubing, and onto the substrate surface at a rate related to the pressure differential and the effective conductance of the cold trap and capillary tubing. The regulator on the noble gas cylinders is typically set at 18 – 20 psig, and the pressure in the buffer volume is maintained at 100 – 150 Torr with the Pfeiffer valve for a typical film growth. The pressure in the buffer volume can be held at a constant pressure to within 0.2 Torr, and this stable pressure control in the buffer volume ensures a stable film growth rate on the substrate. The averaged Pfeiffer valve settings used during a collection of film growths is included in Figure 3.14.

3.3 Noble Gas Film Growth

3.3.1 Background

Noble gas solids offer a stable and inert environment for the capture and preservation of atomic and molecular species. In the mature field of matrix isolation spectroscopy, guest species (atoms or molecules) are codeposited with a gaseous noble gases sprayed onto a cryogenically cooled substrate, whereupon spectroscopic studies can be performed [60]. The structure and properties of the noble gas matrix can have a significant effect on the spectra of isolated species [22]. It is important that techniques for the deposition of such samples result in thin films with consistently reproducible properties.

The Single Atom Microscope requires films of 100 μm in thickness, as 100 μm is sufficient to fully stop energetic ions at most astrophysical energies in the noble gas film based on theoretical stopping power calculations [20]. In contrast, the matrix isolation literature typically utilizes samples thicknesses of order $1 - 10$ μm [44, 33], significantly less than required for the SAM. Transparency of the noble gas film is also an important factor, as Schulze and Kolb report that while Ne and Ar films are generally transparent over the range of thicknesses studied (< 30 μm), Kr and Xe films become opaque with increasing thickness. Film opacity may not play a significant role for matrix isolation studies, as guest species concentration are generally high ($1{:}10^4$) to maximize the signal for bulk spectroscopy [61]. Large guest concentrations are not a luxury available for the SAM, which aims to image extremely small concentrations ($1{:}10^{20}$), where individual atoms may be obscured by noble gas film opacity. It is highly desirable to be able to deposit transparent films of all the noble gas types, as the spectral behavior of guest species can vary significantly between different matrix types.

The next section describes the systems and procedure for depositing noble gas films onto the cryogenically cooled sapphire substrate in pSAM. The aforementioned gas handling system, external to pSAM, controls the film growth rate and offers additional noble gas purification options. The film growth rate is measured via laser thin film interference, and the optical quality of the

films is measured after growth via white light transmission. After describing the equipment and methods, observations from Neon, Argon, and Krypton film growths over a range of deposition temperatures are catalogued.

3.3.2 Experimental setup

The noble gas flows into pSAM from the aforementioned gas handling system, and is directed at the substrate with a thin capillary tube (1/16" OD). Noble gas atoms exiting the capillary tubing will collide with and have some probability of freezing on the surface of the cold substrate, and in this manner a thin film of solid noble gas gradually builds up. The thickness of the film is measured using the principle of thin film interference, wherein extrema are evident in the intensity of laser light transmitted through the film and substrate as the film thickness increases. This phenomena is caused by interference of the coherent laser light in the film and is quantified by the condition for extrema,

$$M\lambda = 2n_1 t\cos\theta_1 = 2t\sqrt{n_1^2 - \sin^2\theta_0} \quad , \tag{3.3}$$

where λ is the wavelength of the light, θ_0 is the angle of incidence, n_1 is the index of refraction of the film material, t is the film thickness, and $M = 1, 2, 3...$ is an integer. Whether this is the condition for a minima or maxima, which are separated only by a half integer (*i.e.* $M + 1/2$), depends on the index of refraction of the substrate material n_2 relative to the film n_1 and whether it is the reflectance R or transmission T being measured [62]. This distinction is immaterial for our purposes, as the condition is used to calculate a growth rate from the frequency that maxima and minima occur.

The experimental setup for a film growth is displayed in Figure 3.15, which also contains detailed part and equipment information. Film growths occur with the substrate in the pSAM growth chamber, which has a circular cross section and 8 access ports. Three of the ports are occupied by a turbomolecular vacuum pump, and an ionization pressure gauge and residual gas analyzer for vacuum diagnostics. Two large viewports on opposite sides of the growth chamber allow optical access through the substrate at a 45-degree angle, and are designated for a thin film

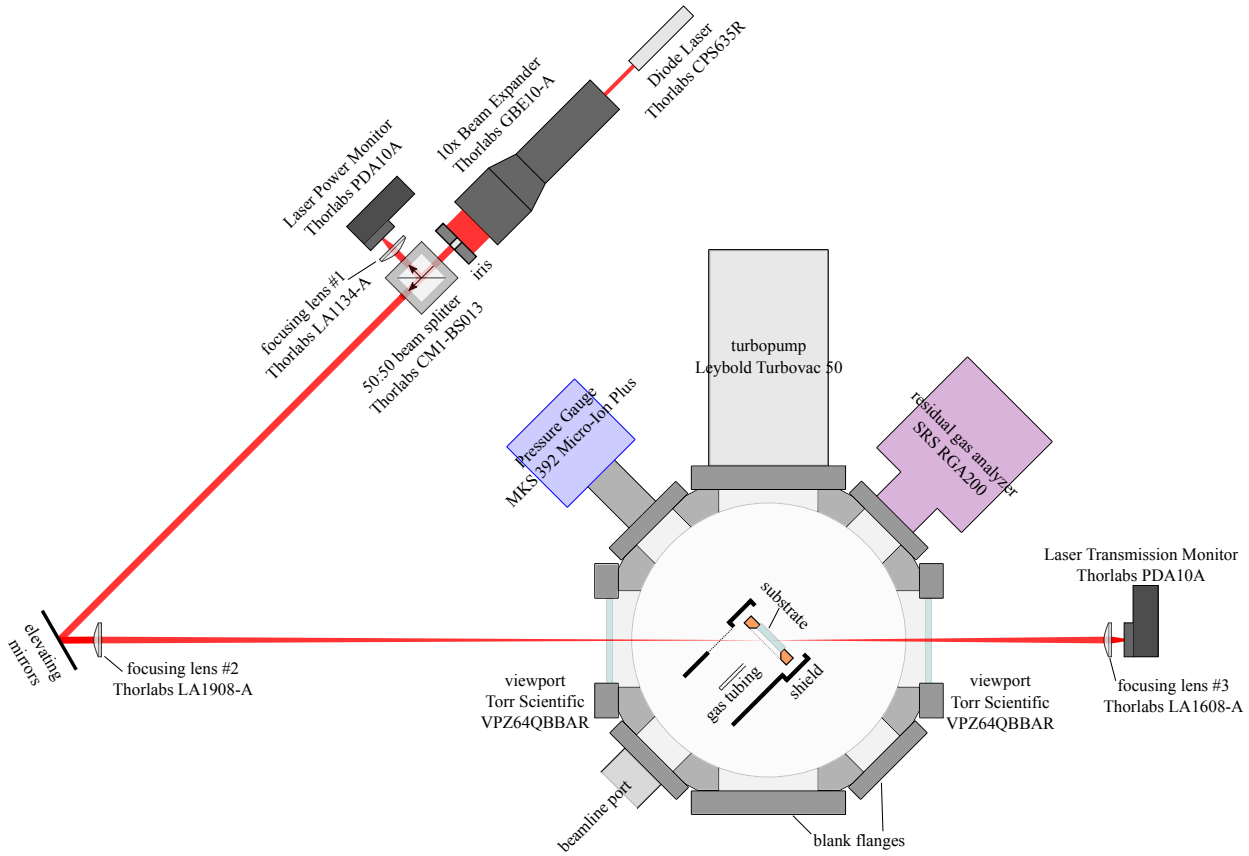

Figure 3.15: Top-Down schematic of a thin film thickness measurement during noble gas deposition. Light from a diode laser is sent through the combination of a beam expander and iris to reduce the light intensity below 1 mW/cm^2. Afterward the light passes through a 50:50 beam splitter and one of the beams is focused onto a photodiode to monitor the beam power. The second beam is directed and focused onto the center of the front surface of the substrate located in the middle of the pSAM growth chamber at a 45 degree angle to the beam path. The light transmitted through the substrate is focused onto a second photodiode to monitor the laser transmission as a function of time.

interference measurement during growth. The port in line with the front surface of the substrate is designated for beamline access, to be utilized for implantation of guest species that will be detected during imaging. The two remaining ports are unused. Light from a diode laser is focused onto the front surface of the substrate to get a localized film thickness measurement at the center of the substrate. The laser power is measured before the substrate with the use of a beam splitter and photodiode to correct for any fluctuations in laser power, and the light transmitted through the film and substrate is monitored with a second photodiode.

A film growth begins by setting the pressure in the gas handling buffer volume to approximately 5 Torr (≈0.3 μm/hr growth rate) for a period of 15 minutes in order to gently deposit an initial thin layer of noble gas on the surface of the substrate. The gas handling pressure is subsequently ramped up to a higher pressure, typically 100-150 Torr (≈100 μm/hr growth rate) for the remainder of the film growth. As an example, a plot of the gas handling pressure and normalized laser transmission is included in Figure 3.16, which clearly displays the increasing oscillation frequency in the transmission as gas handling pressure is increased, corresponding to a growth rate increase. The growth rate is extracted from the laser transmission with a peak finding function that locates the minima and maxima in the interference pattern. Adjacent ($M = 1$) maxima or minima correspond to a thickness increase $\Delta t = \frac{1}{2}\lambda(n_1^2 - \sin^2\theta_0)^{-1/2}$. The diode laser used for these measurements has a wavelength of $\lambda = 638$ nm and is aligned at a 45-degree angle to the substrate, giving $\Delta t \approx 280 - 380$ nm depending on the film type.

The film growth proceeds until a thickness of approximately 100 μm has been deposited. The optical quality of the film is measured after growth based on the transmission of broadband (white) light as measured by a spectrometer. Broadband light is produced by an Ocean Optics DH-2000-S-DUV-TTL light source, employing deuterium and halogen lamps for stable light output (stability and drift ≤0.1%/hr) in the wavelength range of 190-2500 nm. Light from the DH-2000 is fiber coupled to a single collimating lens (Ocean Optics 74-UV) and directed through the substrate in the pSAM imaging chamber. The transmitted light is collected and fiber coupled to an Ocean Optics FLAME-S-ES Spectrometer, either a UV-VIS (200-850 nm) or VIS-NIR (350-1000 nm) model depending on application, with a resolution better than 2 nm. A schematic of the film optical quality measurement is included in Figure 3.17. Typical spectra measured by both spectrometers are included in Figure 3.18.

3.3.3 Results

Films of Neon, Argon, and Krypton have been grown over a range of deposition temperatures and for three distinct configurations of pSAM. The initial configuration (pSAM v1.4) featured a

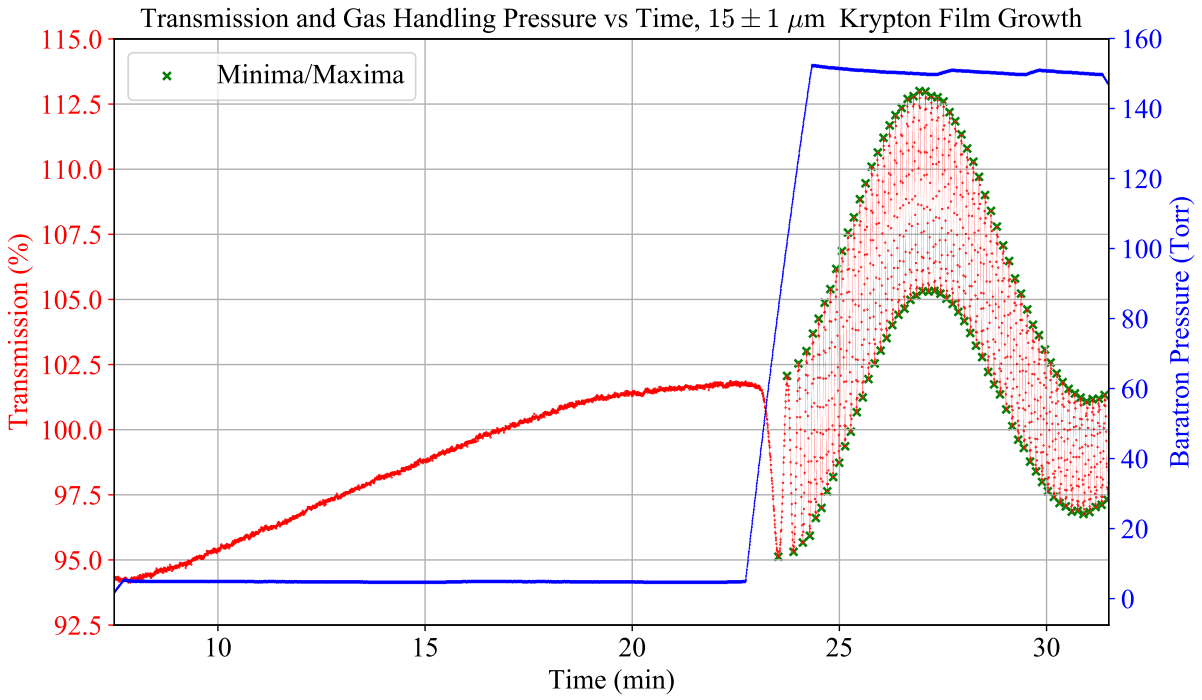

Figure 3.16: Example data from a 15 ± 1 μm Krypton film growth. The laser transmission (red) is plotted alongside the gas handling pressure (blue) as read by the Baratron pressure gauge. After the initial 15 minute deposition period at low pressure, depositing approximately half of a fringe (roughly 140 nm), the gas handling pressure is ramped up to 150 Torr and the fringe frequency increases drastically. Also pictured are the minima and maxima in the interference pattern (green Xs). A much lower frequency oscillation is visible at high growth rates due to thin film interference in the secondary film deposition on the back surface of the substrate.

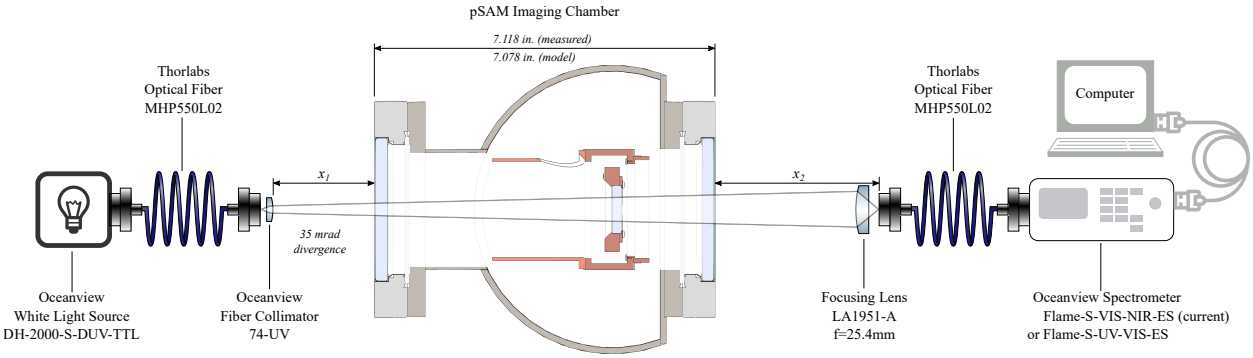

Figure 3.17: Top-Down schematic of a white light transmission measurement. Light is fiber-coupled from the DH-2000 and collimated before passing through the substrate in the pSAM imaging chamber. Transmitted light is gathered by a focusing lens and fiber coupled to the spectrometer.

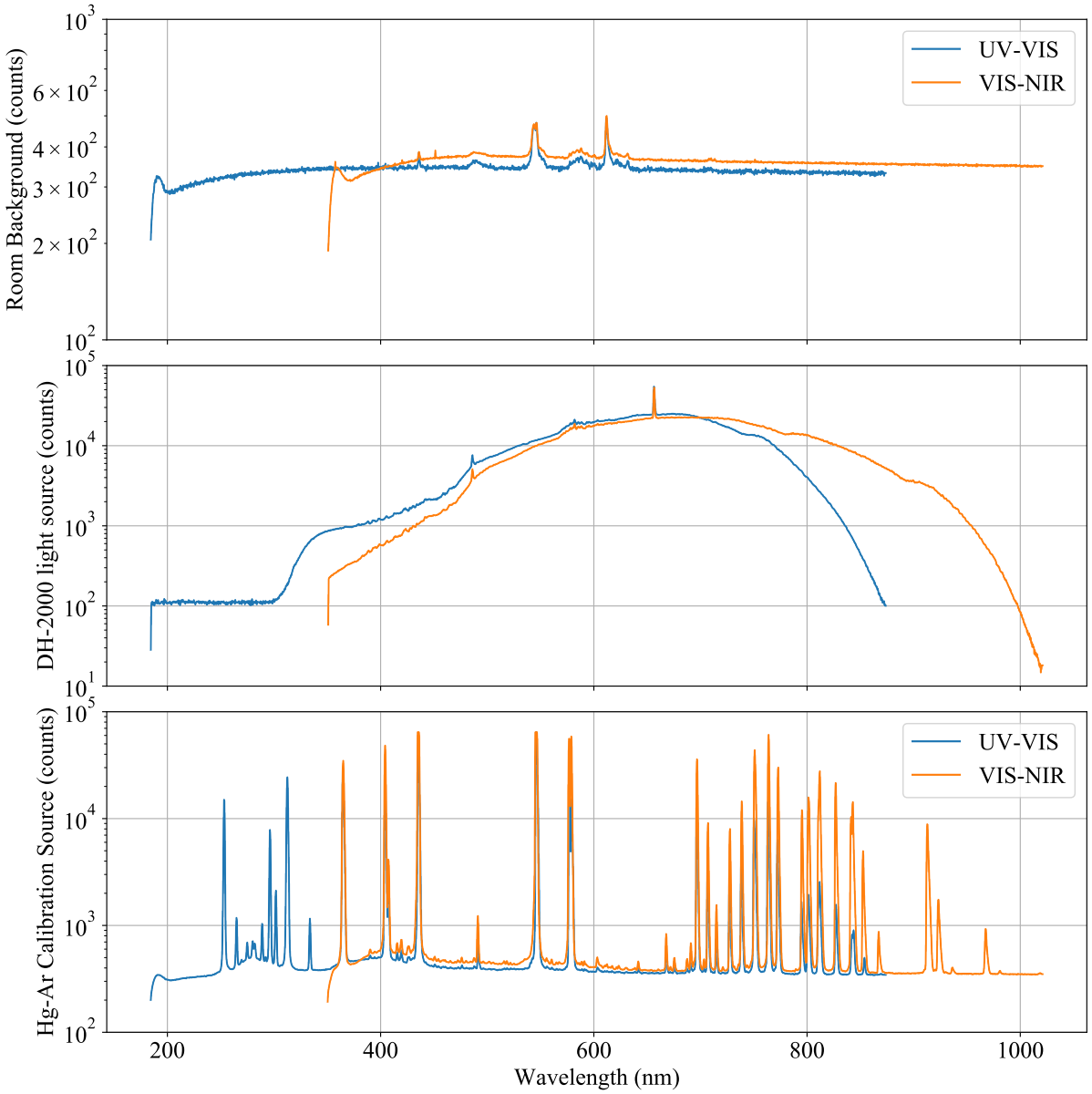

Figure 3.18: *Top:* Typical room background spectra as measured by the UV-VIS and VIS-NIR spectrometers. *Middle:* Typical DH-2000 light source transmission through the substrate (no film) in the pSAM imaging chamber. The peaks in the spectra correspond to the Balmer series transitions from the deuterium lamp in the DH-2000. *Bottom:* Mercury-Argon calibration source (Ocean Optics HG-1) spectrum as measured by each spectrometer. Peak locations generally agree between the spectrometers to within 0.5 nm.

substrate mount with a removable copper substrate holder. The v1.4 substrate mount and holder were threaded (optical SM1) for ease of removal, however this led to thermal contact issues between the substrate mount and holder at low temperature due to thermal contractions. The thermal contact issue was resolved by application of cryogenic vacuum grease (Apiezon-N) between mount and holder, however concerns regarding grease contamination of the substrate surface led to the design of a new substrate mount. For the redesigned substrate mount, installed for pSAM v2.0 and v2.1, the substrate is clamped directly to the mount with indium as a gasketing material, eliminating the need for grease near the substrate. In pSAM v2.0, a new gas feedthrough and slightly longer internal capillary tubing were installed to fix a small vacuum leak. In addition, pSAM v2.0 and v2.1 feature a new section of blackbody shielding attached on the front (film) side of the substrate mount shielding. The new shielding, a cylindrical copper tube (2" ID), was implemented to reduce the total amount of blackbody radiation on the surface of the substrate and to serve as a mounting fixture for the end of the capillary tubing. The end of the new capillary tubing was firmly mounted to the new shield tube with a customized brass clamp, but this led to issues when flowing Argon as the temperature of the capillary was low enough to freeze Argon inside the capillary, effectively clogging it. As a result, only Neon films could be grown in pSAM v2.0 as the base temperature of the shielding (31 K), and therefore the capillary tubing, is not low enough to freeze and become clogged with solid Neon. For pSAM v2.1, the end of the capillary tubing was remounted with Kapton tape, which has very poor thermal conductivity, instead of brass in order to thermally insulate it from the copper shielding. The pSAM configurations are summarized in Table 3.3, which also includes the measured distance between the substrate and the end of the capillary tubing for each configuration. Figure 3.5 details the differences between the two substrate mounts.

3.3.3.1 Growth Rate

The growth rate follows a nonlinear relationship with the gas handling pressure as is displayed in the left column of Figure 3.19, which includes data from approximately 30 separate film growths. As the pSAM vacuum is maintained by pumping during growth ($< 10^{-4}$ Torr), it is reasonable

Table 3.3: Table of pSAM configurations.

Version	Tubing Distance	Base Temp.	Pressure	Notes
v1.4	2.8 cm	5.4 K	10^{-8} Torr	Original substrate mount with cryogenic grease. End of capillary tubing is unfixed.
v2.0	1.9 cm	5.8 K	10^{-8} Torr	New capillary tube. Redesigned substrate mount. End of capillary tube clamped to new shielding tube. Capillary clogs with frozen Argon.
v2.1	2.3 cm	5.8 K	10^{-8} Torr	Remounted end of capillary tube with Kapton tape. Clogging problem fixed.
v2.2	2.2 cm	4.4 K	10^{-8} Torr	Replaced Al-mylar shielding. Moved Temperature sensor to 2^{nd} stage heat exchanger.

to expect a growth rate that varies linearly with gas handling pressure, as would be expected for freely flowing gases. Free molecular flow of gases is characterized by the mean free path between collisions of gaseous atoms being large compared to the size of the enclosing volume, but that is generally only the case for pressures below 1 Torr [63]. As the capillary tubing inside pSAM has an inner diameter of only 1 mm and is roughly 50 cm in length, and the gas handling pressure is in excess of 100 Torr, we interpret the nonlinearity as a consequence of gas flow through the capillary tubing being viscous.

The gas handling system was not substantially changed between pSAM configurations, so the variation of growth rates between pSAM configurations is attributed to differing distances between the end of the capillary tubing and the substrate surface. The Neon growth rate variation between pSAM configurations is consistent with the noble gas beam intensity following an inverse square law with distance. This behavior is similarly evident in the Argon growth rate but does not appear to be true for Krypton, as the growth rate is observed to vary by less than 20% between v1.4 and v2.1 while the inverse square law predicts a $1 - (2.8\,\text{cm}/2.3\,\text{cm})^2 \approx 50\,\%$ variation. One possible explanation for this inconsistency can be found by considering the different condensation temperatures between noble gases along with the presence cryogenic shielding in vicinity of the

substrate.

A linear relationship is observed if the growth rate is plotted as a function of pSAM pressure, as displayed in the right column of Figure 3.19. This linearity implies that the pSAM pressure during film growth can be used as a relative measure of the amount of gas flowing into pSAM that does not freeze onto a cryogenic surface. Gas exiting the capillary tubing will have some probability of sticking to the substrate or substrate mount, the cryogenic shielding, or colliding with other gas atoms and escaping to be pumped away. Neon is the simplest case to consider as it can only freeze on the substrate or substrate mount, since the base temperature of the cryogenic shielding (31 K) is too high to solidify Neon. Rough measurements suggest that 80% of Neon freezes somewhere with the remainder being pumped away, using the manufacturer's advertised pumping speed of the turbo pump and ambient pressure to calculate the volume of gas pumped away during growth.

Krypton on the other hand is likely to freeze anywhere on the substrate, mount, or shielding structure due to its' significantly higher freezing point around 40 K. This results in lower pSAM pressure relative to Argon or Neon during film growth as very little gas is able to escape without freezing. Attaching the new shield tube for pSAM v2.1 resulted in significantly lower ambient pressures during Krypton growth relative to v1.4 due to the addition of a cold surface surrounding the capillary tubing. The picture for Argon is slightly more complicated, as the temperature of the cryogenic shielding is 35-36 K when the substrate is set to Argon film deposition temperatures, which range from 24-36 K in this study. The vapor pressure of solid Argon exceeds 10^{-6} Torr at temperatures above 30 K, resulting in noticeably higher ambient pSAM pressures during film growth especially at higher deposition temperatures. The growth rate relative to pSAM pressure is plotted as a function of deposition (substrate mount) temperature in the top row of Figure 3.21, where each data point represents a single film growth. The parameter χ_{GR} is the slope extracted from a linear fit to the growth rate vs pSAM pressure data in fig 3.19. In general, the growth rate is shown to be independent of deposition temperature, and the Argon vapor pressure increase is clearly evident for deposition temperatures above 30 K.

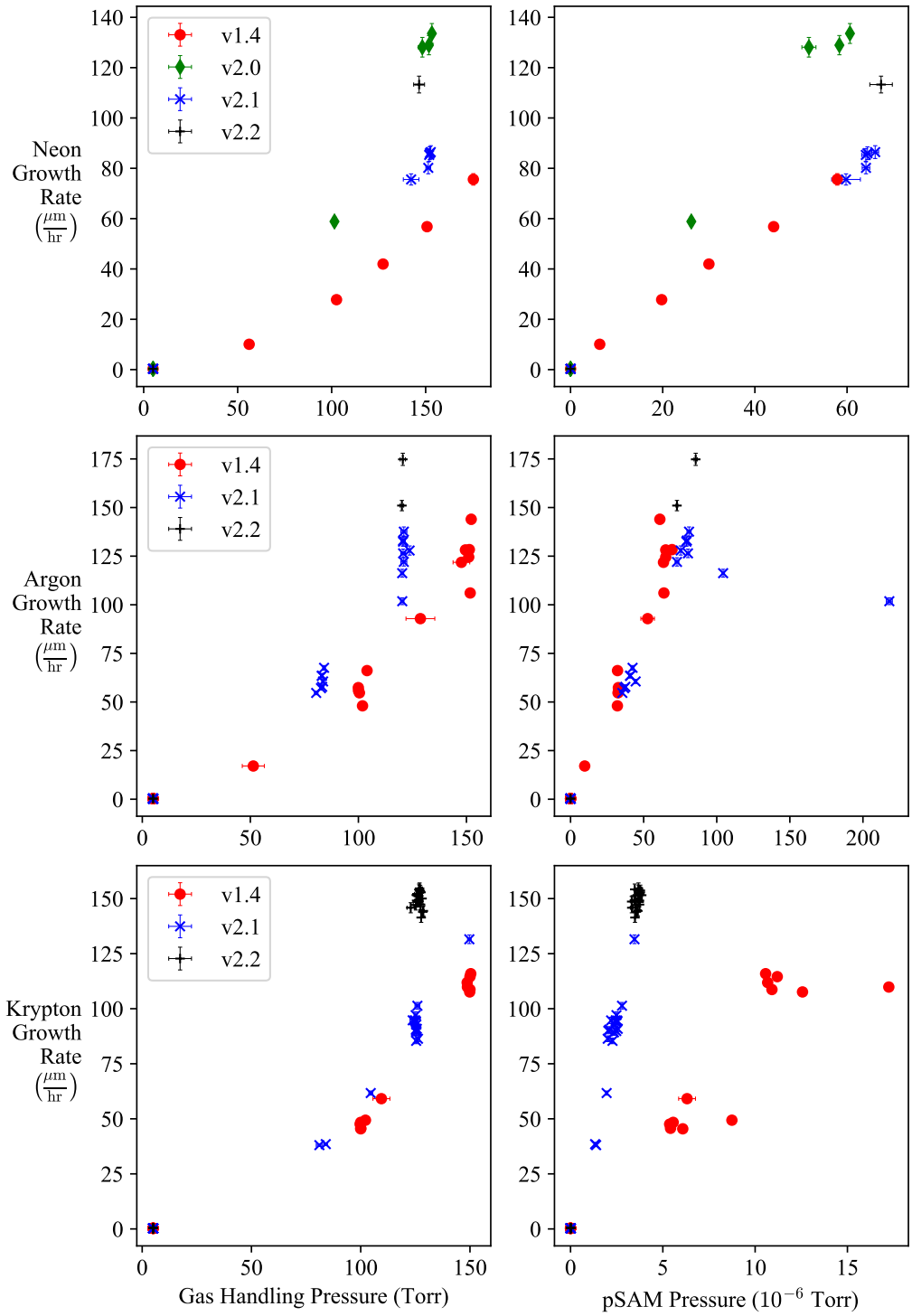

Figure 3.19: Measured Neon, Argon, and Krypton growth rates as a function of Gas Handling pressure (left column) and pSAM pressure (right column) for different pSAM configurations and deposition temperatures.

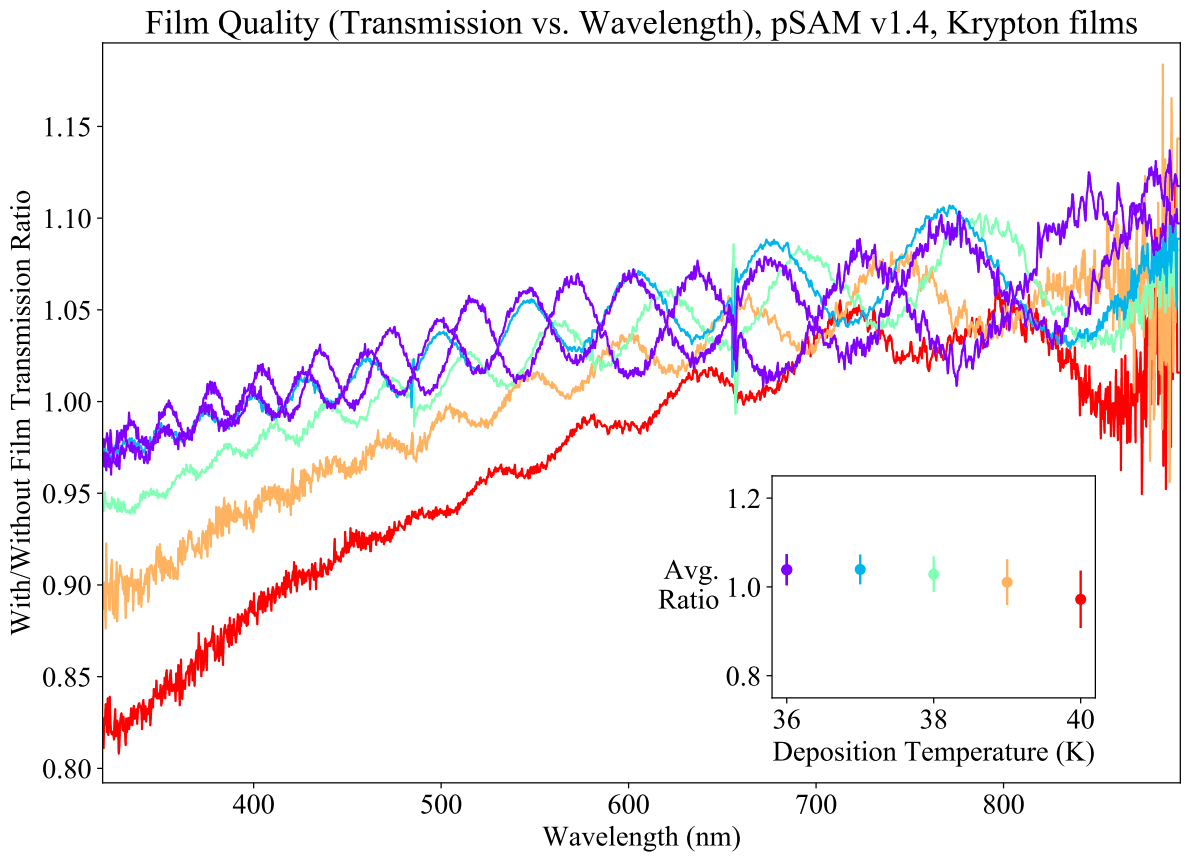

Figure 3.20: Intensity of light transmitted through 6 separate krypton films deposited at different temperatures (two films deposited at 36 K are plotted), relative to the intensity of light transmitted through the bare substrate (no film), as a function of wavelength. The oscillations evident in each trace are due to thin film interference in the secondary film on the back of the substrate. The inset plot shows the average transmission (error bars denote the standard deviation) for each film as a function of deposition temperature.

3.3.3.2 Optical Clarity

The optical clarity of a film is quantified by measuring the intensity of broadband light from the DH-2000 transmitted through the film and substrate relative to a clean (no film) substrate, as measured by a spectrometer. A set of typical film clarity measurements for krypton films is included in Figure 3.20. The noble gas films behave as a kind of anti-reflective coating on the substrate, as the transmission of film and substrate can be as high as 110% for exceptionally clear films. The clarity of 100 μm noble gas films is sensitive to substrate temperature during deposition. Though

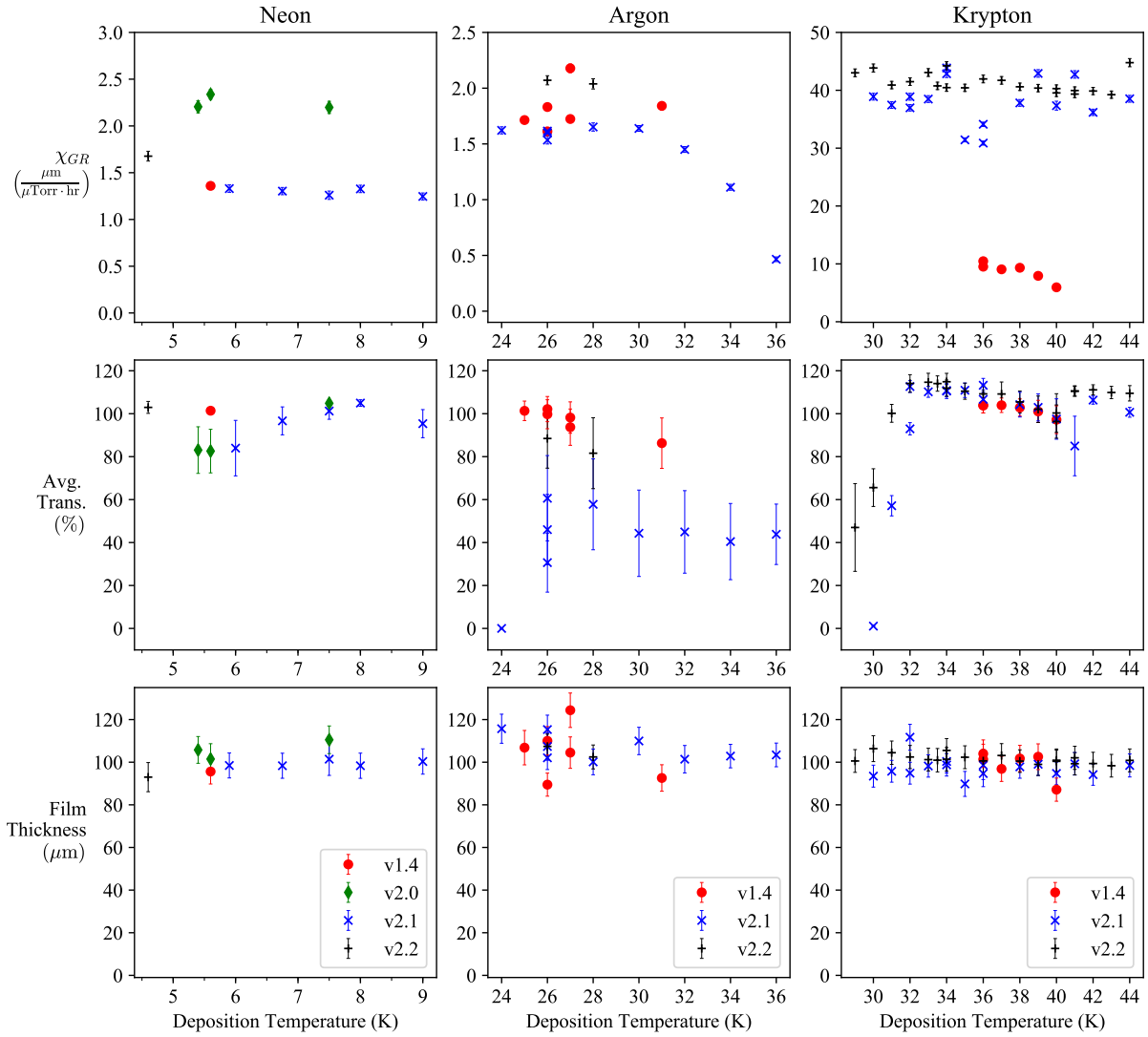

Figure 3.21: Collection of growth parameters as a function of deposition temperature. Top row: growth rate relative to pSAM pressure. Middle row: average transmission of film and substrate relative to only substrate. The error bars denote the transmission over the range of wavelengths measured with the spectrometer. Films were generally more transparent to IR, and more opaque to UV. Bottom row: thicknesses of films analyzed in this work.

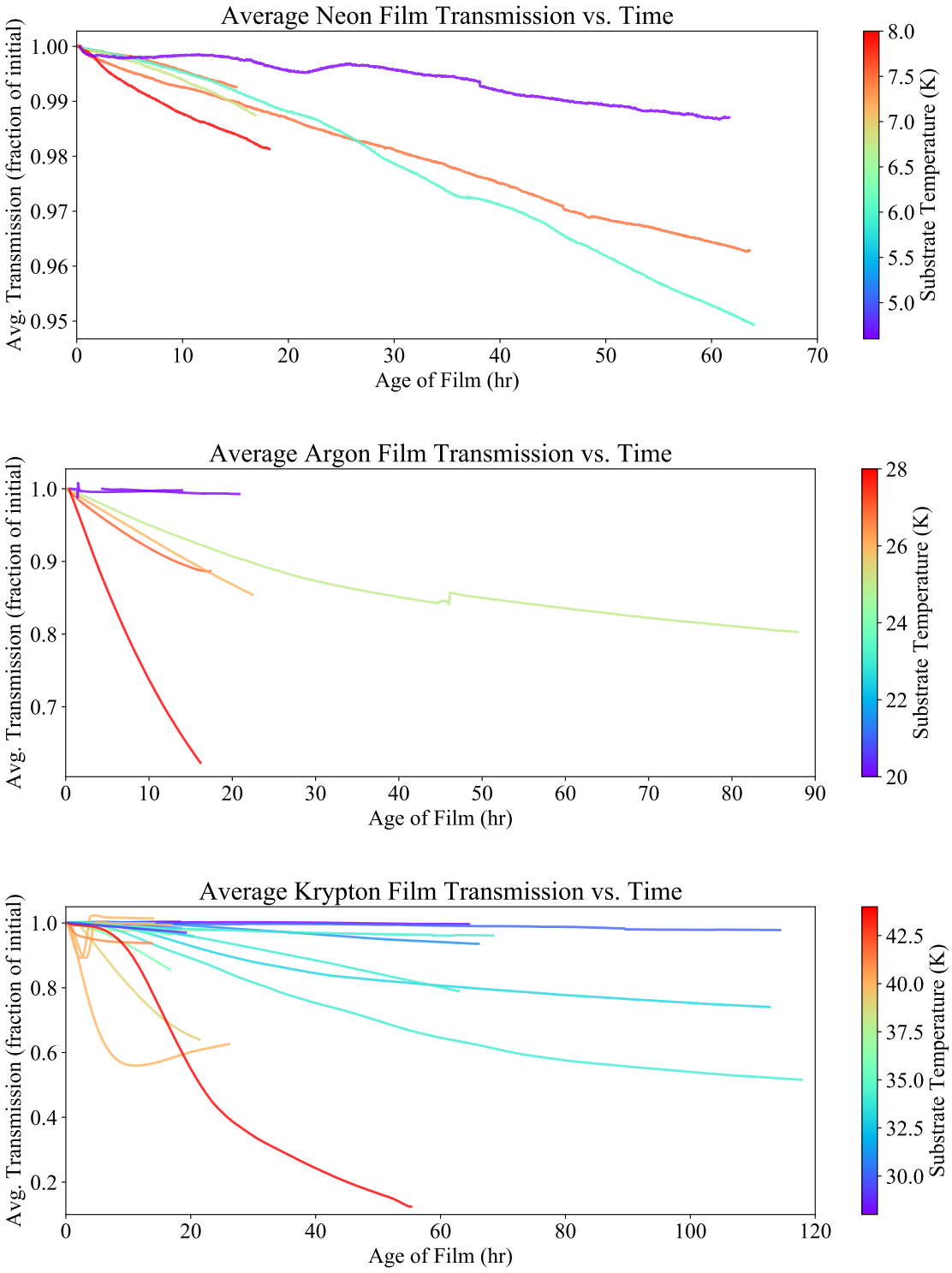

Figure 3.22: Film clarity as a function of time and temperature for neon, argon, and krypton. Film clarity is relative to the initial transmission to decouple variations in initial film transmission from the time dependent behavior. Holding a film at lower temperatures tends to 'freeze in' the initial film transparency.

films generally remain transparent below 20 μm, they become increasingly opaque with increasing thickness outside of a small temperature window for each film type, where the transmission is maximized. Films showing any opacity are more opaque to shorter wavelength light and generally remain transparent to wavelengths longer than 700 nm, except for films having below 90% average transparency. The ideal temperatures T_{id} are all above the characteristic temperatures T_{ch} reported in [28], included in Table 3.4, but below the temperatures where sublimation of the accumulated frozen gas becomes significant. Annealing films after deposition causes them to become more opaque. The averaged transmission of white light for Ne, Ar, and Kr films as a function of deposition temperature are plotted in Figure 3.21. Figure 3.23 contains pictures of films that exhibit common characteristics.

Neon films were grown over a limited temperature range, as the base (lowest) temperature was limited to 4.6 K and sublimation of Neon becomes significant at temperatures higher than 9 K. The only Neon films grown during v1.4 configuration were at the base temperature and were highly transparent by eye and to white light. Interestingly, the films were slightly opaque at the base temperature for the v2.0 and v2.1 configurations, and the highest transparency deposition temperature was achieved at 8 K. A film grown at 4.6 K in v2.2 shattered at a thickness of 60 μm during growth, but was otherwise transparent. The specific cause of the discrepancy between configurations has yet to be identified. The white light transmission of Neon films maintained at deposition temperatures (6 – 8 K) decreased at a rate of 0.02 – 0.1 %/hr, with lower temperatures generally maintaining initial transparency for longer (see the top plot in Figure 3.22). Effects of cooling the films after growth were not studied due to the limited available temperature range.

Argon films were deposited at temperatures ranging from 24-36 K and show a stark difference between pSAM configurations. Films during v1.4 were most transparent at 25 K, becoming steadily more opaque with increasing temperature, and in general were found to be slightly less transparent to visible wavelengths $\lambda < 700$ nm than Neon or Krypton. Films maintained at deposition temperatures became increasingly opaque with time, at a rate of 0.02 – 4 %/hr, worsening with increasing temperature (see the middle plot in Figure 3.22). Cooling films to 20 K after growth

allowed the transmission to remain constant for more than 12 hours. Cooling 100 μm films below 20 K would cause them to shatter.

Films grown during v2.1 were significantly more opaque than v1.4, scarcely breaking 50% transparency at the best deposition temperature, and a film deposited at 24 K was nearly completely opaque (transmission < 0.5%). Similar to Neon, T_{id} was shifted higher by a few degrees for v2.1 relative to v1.4. The films during v2.1 are visibly cloudy in the center of the substrate and become more transparent toward the edge. The opacity of the v2.1 films is likely related to the addition of the cylindrical copper tube to the shielding structure around the front substrate surface and capillary tube. The shielding structure is at a temperature corresponding to a high vapor pressure for solid Argon ($T_{shield} \approx 36$ K). The presence of low temperature Argon gas continuously subliming from the shielding surface may be negatively affecting the film transparency.

Krypton films were deposited at temperatures ranging from 29-44 K and show clarity behavior consistent across v1.4, v2.1 and v2.2. Films exhibited the highest white light transmission when deposited near 34 K, with a slightly decreasing transmission with increasing temperature. Films become rapidly opaque at temperatures below 32 K, which corresponds to T_{ch} reported in [28]. Small speckling became visible in films at temperatures of 32 K and below. A film grown at 6 K was completely opaque and brittle, taking on the appearance of snow or frost, and a section of the film dislodged from the substrate during growth. Curiously, krypton films grown near 40 - 41 K exhibit wispy, frost-like structures visible in the film that disappear with time as the films become cloudy. Films maintained their initial transparency for more than 100 hours if temperature was held below 30 K. Films maintained at $35 - 36$ K exhibited decreasing transparency at a rate of $0.1 - 0.2$ %/hr of their initial transparency (see the bottom plot in Figure 3.22). Cooling the films to after deposition was effective in maintaining transparency, however cooling 100 μm Krypton films below 30 K caused them to shatter independently of the cooling rate.

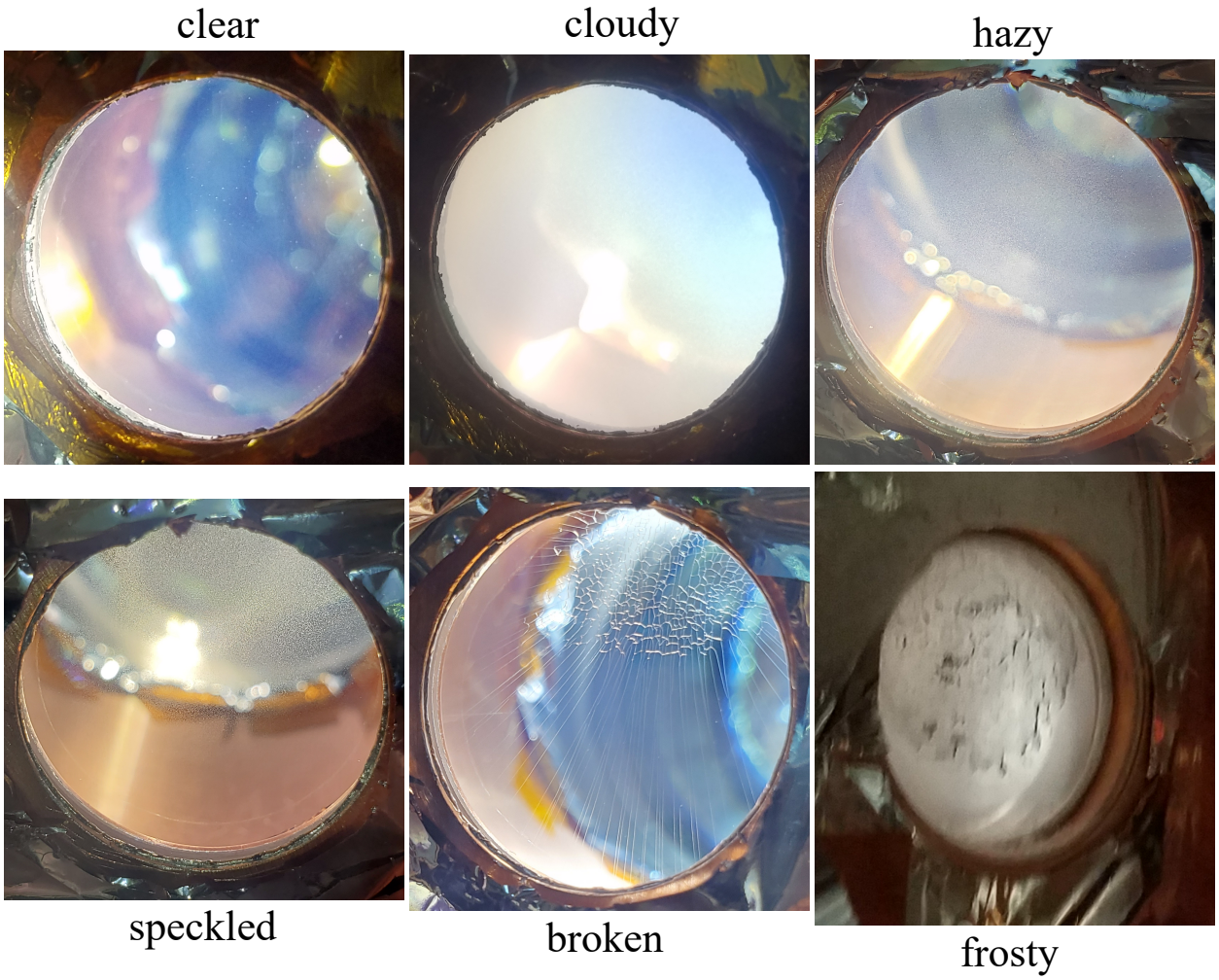

Figure 3.23: Pictures of films exhibiting different characteristics. The pictures were taken through the rear viewport on the pSAM imaging chamber (except for the bottom right), so the film is on the far side of the substrate.

Table 3.4: Table of solid noble gas film properties. T_{subl} is defined as the temperature at which the vapor pressure is 10^{-4} Torr.

	Neon	Argon	Krypton	Source
T_{ch} (K)	5 ± 1	18 ± 1.5	29 ± 2	[28]
vp_{ch} (Torr)	9.4×10^{-15}	1.1×10^{-17}	6.5×10^{-14}	[26]
T_{id} (K)	8 ± 0.5	27 ± 2	35 ± 2	this work
vp_{id} (Torr)	2.2×10^{-7}	5.4×10^{-9}	3.0×10^{-10}	[26]
T_{subl} (K)	10.0	36.2	50.8	[26]
d_0 (μm)	19	22	27	[28]
d_0 (μm)	20	26	19	this work

3.3.3.3 Fringe Contrast

The amplitude of interference fringes in transmitted laser light decreases with increasing film thickness, a phenomena also reported in [28]. The fringe contrast, defined as the difference in transmitted laser power for an adjacent minima and maxima, is typically $10 - 15\%$ for the initial interference fringes as displayed in Figure 3.24. This contrast steadily decays with increasing thickness until a maximum thickness where fringes become indistinguishable, d_0. The fringe contrast decay and maximum thickness (d_0) as a function of deposition temperature are also displayed in Figure 3.24. The maximum thicknesses reported in [28] are included in Table 3.4 alongside the average d_0 of all film growths reported in this work. The loss of contrast is attributed in [28] to a loss of intensity within the film due to absorption and scattering. Since interference fringes are indistinguishable for most films beyond thicknesses of 40 μm, and the gas handling pressure is held constant, the growth rate is assumed to remain constant for the remainder of the growth for the purposes of calculating the final thickness. Locations of minima and maxima are extracted during post-growth analysis using the signal processing algorithm `argrelextrema`, part of the SciPy package in Python [64]. The algorithm typically begins reporting erroneous extrema when the fringe contrast falls below 0.5%, where fringe amplitudes approach the noise floor for the photodiodes.

The initial fringe contrast generally decreases with increasing deposition temperature, but interestingly the fringe contrast decay increases proportionally with temperature, leading to relatively constant d_0. The initial fringe contrast can be exceptionally low at higher deposition temperatures, in the range from $1 - 5\%$, but contrast is typically sustained beyond 10 μm. Krypton films deposited in pSAM v2.1 exhibit a drastic, low frequency oscillation in fringe contrast, attributed to an interference beating effect with in the secondary film on the back of the substrate, which results in a systematically smaller d_0. In the absence of the beating effect, fringes are observable out to thicknesses of 30μm. A single Argon film deposited at 27 K sustained observable fringes at thicknesses beyond 80 μm, suggesting a larger d_0 may be achievable. A significant change was observed between pSAM configurations when considering the maximum thickness at which fringes

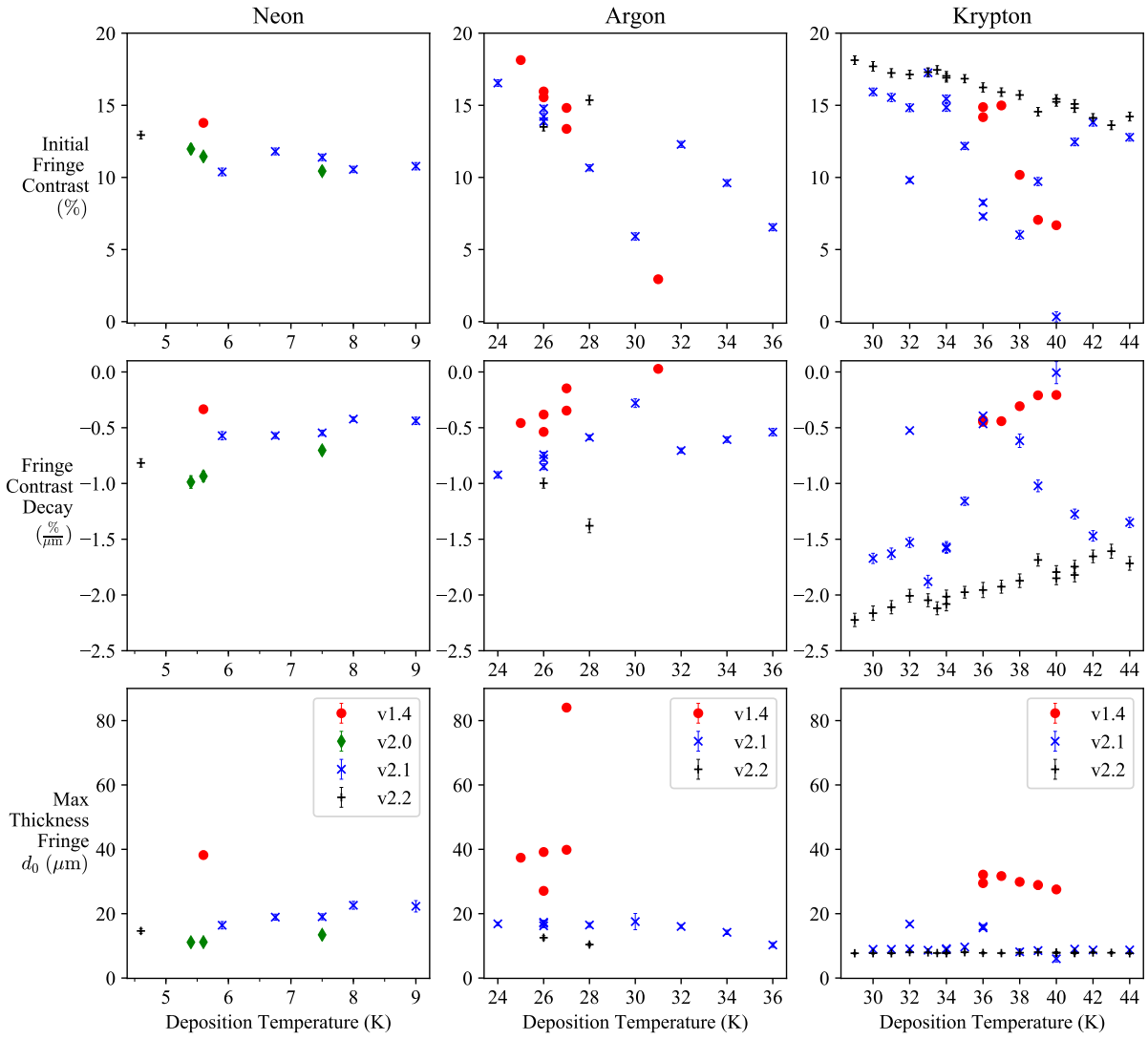

Figure 3.24: Initial fringe contrast, contrast decay, and maximum thickness with an observed fringe plotted as a function of deposition temperature.

could be observed, consistently across all film types. Values of d_0 in v1.4 are larger by roughly a factor of 2 compared to v2.0 and v2.1 The laser diode system detailed in Figure 3.15 was partially disassembled between configurations v1.4 and v2.0 to allow for the removal of pSAM from the laser table. A plausible source of the systematic difference between pSAM configurations could be found in the realignment of the laser diode system performed after subsequent re-installation of pSAM on the laser table. A slightly longer focal length lens was utilized as focusing lens # 2 in v2.0 and v2.1, mainly for convenience.

3.3.3.4 Film uniformity

The thickness of a Krypton film was measured along several points along a vertical line through the center of the substrate. Thin film interference fringes were observed when monitoring the intensity of reflected and transmitted laser light focused on the substrate from a continuous wave Ti:Sapphire laser (MSquared SOLSTiS), whose wavelength was continuously varied between $\lambda = 770 - 800$ nm (487 cm^{-1}, or 14.6 THz scan width). Similar to the thickness measurement during growth, film thickness can be determined from the position of extrema using the relation

$$t = \frac{M_{ab}\lambda_a\lambda_b}{2(\lambda_a - \lambda_b)\sqrt{n_1^2 - \sin^2\theta_0}}, \tag{3.4}$$

where λ_a and λ_b are the wavelengths of two extrema, θ_0 is the angle of incidence, n_1 is the index of refraction of the film material, t is the film thickness, and M_{ab} is the number of fringes separating the extrema [62]. For example, adjacent maxima would correspond to $M_{ab} = 1$, and a maximum at λ_a separated from a minimum at λ_b by two minima and maxima would correspond to $M_{ab} = 2.5$. The number of fringes observed, and consequently the uncertainty of a given measurement, is determined by the width of the scan and the thickness of the film. Observation of one complete fringe in the 487 cm^{-1} window requires a thickness of at least 7.6 μm for a Krypton film ($n_1 = 1.38$, $\theta_0 = 7°$). A larger scan width, thereby increasing the number of fringes observed, could be used to reduce uncertainty in thickness, but the width of scans was limited to 30 nm in the interest of time (approximately 10 min/scan).

No fringes were observed when this technique was applied for 100 μm Argon and Krypton films, consistent with maximum fringe thicknesses reported in the fringe contrast section. The uniformity measurement was performed on Krypton films during v1.4 and v2.1 with center thicknesses measured during growth of 15 μm. Thickness measurements were taken at points along a vertical line through the center of the substrate. The interference fringes observed in reflection at each point for the v1.4 uniformity measurement are shown in Figure 3.26, and the thickness at each point is plotted in Figure 3.25. The film is significantly thicker near the top of the substrate closest to the end of the capillary tubing, which is located at $y = 13$ mm and the horizontal distance listed in Table 3.3.

The fringes also had the greatest contrast near the top of the substrate. Although fringes were observed across the entire substrate for the v1.4 measurement, the fringe contrast fell below 0.5 % near the bottom, relative to an order of magnitude higher near the top. Interestingly, the v2.1 measurement only yielded fringes at the top of the substrate, and clear fringes were not observed below 5.4 mm during the initial scan. To explore the possibility of a thickness dependence on the presence of fringes, an additional 5 μm of Krypton was deposited and the scan was repeated, but fringes were again only observed near the top of the substrate, though at lower contrast and disappearing altogether at 5.4 mm. The thickness measurements plotted at $y = 0, -5.4$ mm in the right panel of Figure 3.25 come from the fringes observed during the initial and subsequent krypton depositions. It can be inferred from this measurement that the rapid disappearance of fringes for scans below 7.2 mm does not seem to be dependent on the thickness of the film. The lack of fringes could be due to the local nonuniformity of the film where the laser interference occurs. This nonuniformity over the beam spot size may be sufficient to destroy any measurable interference signal on the downslope of the distribution, whereas the film thickness seems to have plateaued (more uniform) at the top of the substrate, allowing for measurable interference fringes. This is consistent with observing fringes across the entire substrate in v1.4, as the increased separation between substrate and capillary tubing resulted in a more uniform film.

The measured thickness distribution on the film is fairly consistent with both uniform and cosine

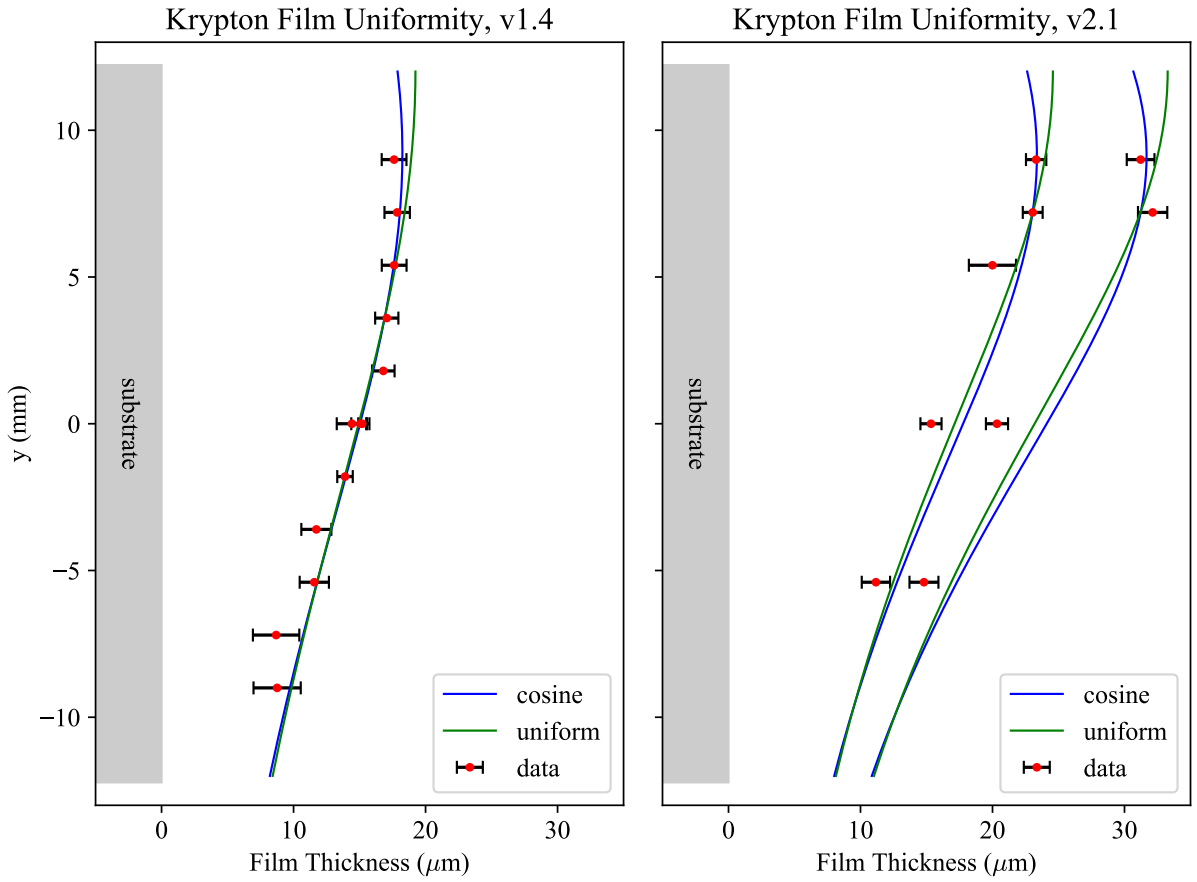

Figure 3.25: Thickness of a Krypton film as a function of position along a vertical line through the center of the substrate, as measured in pSAM v1.4 (left) and v2.1 (right). The included lines depict the predicted thickness distribution assuming uniform and cosine intensity distributions for gas leaving the end of the capillary tubing. It should be noted that the vertical and horizontal axis have different scales. For v2.1, interference fringes were only observed at the top of the substrate. Attempts at other positions near the middle and bottom of the substrate yielded no interference pattern, and a second measurement was performed after depositing an additional 5 μm onto the film, similarly yielding interference fringes only near the top.

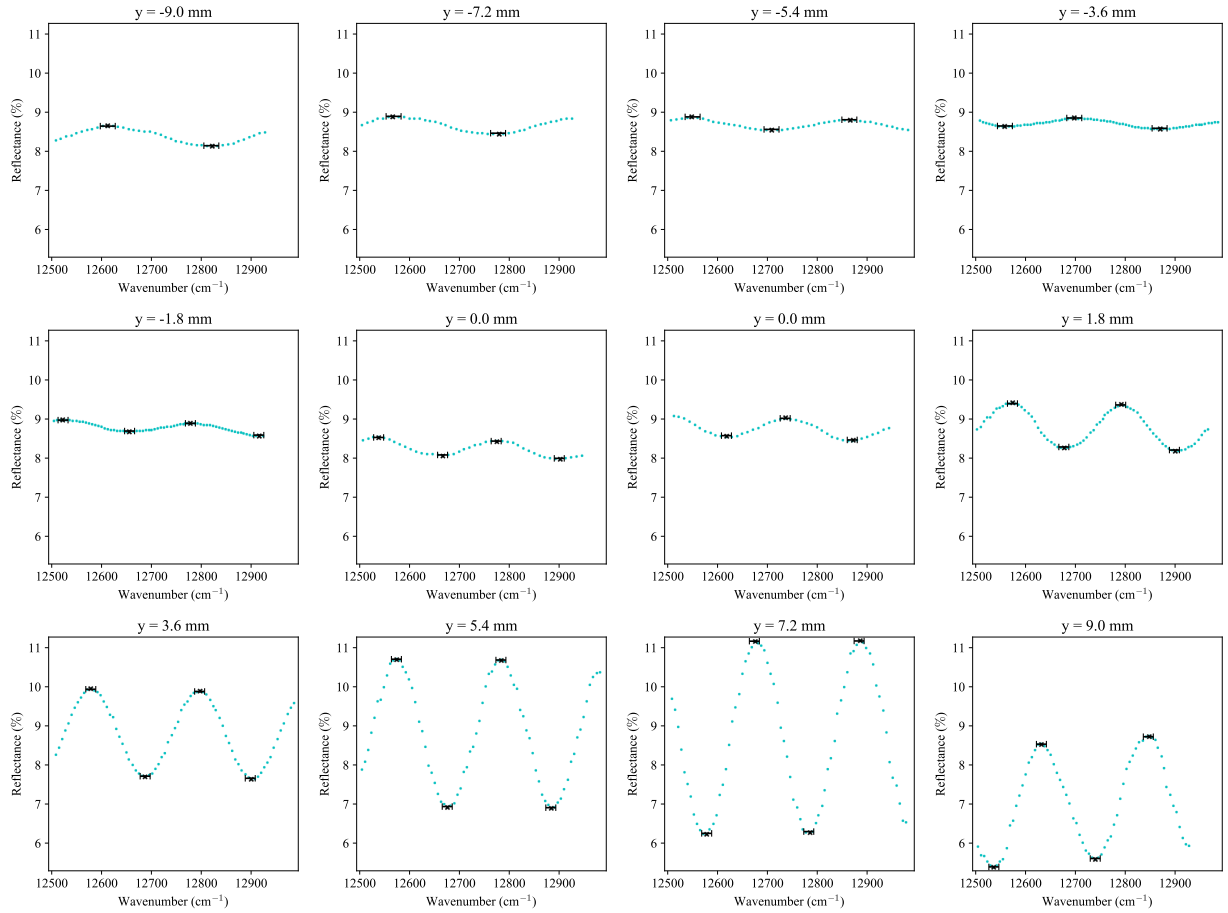

Figure 3.26: Set of wavelength scans for the Krypton film uniformity measurement performed in pSAM v1.4, which illustrates typical interference patters for a wavelength scan. The amplitude of the fringes was largest at the top of the substrate.

intensity distributions from of the end of the capillary tubing, which implies that the film uniformity is dominated by an inverse square law from the end of the capillary tubing. The cosine distribution predicts a slightly sharper peak, but the behavior on the downslope of the peak is too similar to the uniform distribution to distinguish within the precision of these measurements. The capillary tubing for v2.1 is 20% closer to the substrate, likely causing the film to be noticeably less uniform in v2.1, and suggestive of a sharper intensity distribution than attributable to a cosine. Attaining a more uniform film can be accomplished by increasing the distance between substrate and tubing, though at the cost of using more gas. Alternatively, increasing the number of tubes symmetrically around the substrate could decrease the nonuniformity.

3.3.3.5 Film purity

Quantifying the amount of impurities in the noble gases flowing into pSAM can be accomplished via direct measurement with the residual gas analyzer (RGA). Neon, argon, and krypton gases were flowed into pSAM at room temperature by stepping the gas handling system buffer volume pressure between 2 – 10 Torr, while continuously measuring the partial pressures of the most abundant residual gases in pSAM for 5 minute intervals. The vacuum pumps on pSAM were running, and the gas handling pressure was purposely limited to low pressure (10 times lower than during a film growth) to keep the pressure inside pSAM below 10^{-5} Torr, as the RGA is limited to a maximum pressure of 10^{-4} Torr (with the electron multiplier off). The purity of the gas was measured without any additional purification measures (getter purifier was bypassed, and liquid nitrogen cold trap was at room temperature) to establish a baseline. The purity measurements are summarized in Table 3.5. The RGA is sensitive to partial pressures on the order of 10^{-9} Torr with the electron multiplier powered off, which is necessary when operating at such high pressures, and so the sensitivity of the purity measurements was limited to 0.3%.

As a baseline, neon gas was flowed into pSAM while at a temperature of 20 Kelvin which sufficiently low to freeze nearly all impurity gases. As expected, the resulting purity measurements were consistent with the labeled gas bottle purity (99.999%) within the sensitivity of the RGA, since the most abundant residual gases (nitrogen, oxygen, water, CO_2, etc) would freeze to the substrate before having a chance to contact the RGA sensor. However, measurements performed with pSAM at room temperature showed impurity levels well in excess of the labeled gas purity. Neon and krypton were measured to have impurities at the level of 5%, and argon significantly better at 1%. In all cases the impurities were primarily molecular nitrogen, with trace amounts of the other components of air. The purity generally improved with gas flow rate, suggesting the impurities may be acquired in the gas handling buffer volume and cold trap, and that the purity may be significantly better at the gas flow rates used during film growth (Gas Handling pressures above 100 Torr). Unfortunately, a purity measurement is not possible at such flow rates due to the aforementioned pressure limitations of the RGA.

Table 3.5: Purity of noble gases flowing into pSAM as measured with the RGA.

G.H. Pressure Torr	Neon (20 K) %	Neon (r.t.) %	Argon (r.t.) %	Krypton (r.t.) %
2	99.4(9)	94.8(3)	98.8(5)	94.9(7)
4	99.4(8)	94.8(4)	99.0(4)	94.8(5)
6	99.5(9)	95.3(4)	99.1(3)	95.1(4)
8	99.5(8)	95.7(4)	99.2(3)	95.7(4)
10	99.6(8)	96.2(4)	99.3(3)	96.3(3)

3.3.3.6 Noble Gas Use and Sticking Probability

One method to measure the total amount of gas used during a film growth is to use the vacuum pressure and the pumping speed of the turbomolecular pump (TMP, an Oerlikon TurboVac 50). The ideal gas law translates the TMP pumping speed $S = 55\,\mathrm{L/s}$ and vacuum pressure P into a molar flow rate $\dot{n}$ via

$$\dot{n} = \frac{SP}{RT}, \tag{3.5}$$

where T is the gas temperature and $R = 8.314$ J mol^{-1} K^{-1}. Integrating this quantity over the duration of the film deposition will give the amount of gas that is wasted during growth (pumped away). Similarly, integrating this quantity as the cold components are warmed will yield the total amount of gas that is frozen somewhere on the cold components. It is however not clear what the temperature of the noble gas is, either during deposition or sublimation. During growth, gas entering pSAM is expected to be at room temperature, but likely cools somewhat in the narrow capillary tubing that snakes inside the approximately 35 K copper shielding structure. The gas atoms subliming from the substrate mount as the film is melted can be assumed to be the temperature of the substrate mount on average, but it is not clear what the average gas temperature is in the vicinity of the pressure gauge and TMP, after having interacted with the 35 K copper shielding structure and the 300 K vacuum vessel. The mean free path of gas atoms at 10^{-4} Torr (typical maximum pSAM pressure during growth) is on the order of $0.1 - 1$ m, equal to or larger than the size of the vacuum vessel itself, so the gas atoms should not have sufficient self-interaction to create a temperature gradient between the cold components and the vessel walls.

Neon is ideal to use for this measurement since its' low sublimation temperature (10 K) means it will only freeze to the substrate mount, unlike argon and krypton which can freeze to the copper shielding structure. Neon's 10 K sublimation temperature is also significantly separated from the common components of air, so it is reasonable to assume the measured vacuum pressure is almost entirely due to neon and not nitrogen or any other gases. For a 100 μm film grown in pSAM v1.4, a total of 81 ± 16 mmol of neon was used based on integrating Equation 3.5 through the growth and sublimation, assuming a neon gas temperature of 30 ± 5 K and including a 15% manufacturers uncertainty in the pressure. Of that total, 8.5 mmols (10%) was pumped away during growth, with the remainder coming off during sublimation. As the molar flow rate is inversely proportional to temperature, assuming a neon gas temperature of 300 K would reduce the total to 8.1 mmol. It is reasonable to expect the temperature of neon gas is the same during growth as it is during sublimation, so the waste factor of 10% is likely independent of the assumed temperature. Based on a rough calibration of the gas handling system, an estimated 84 ± 3 mmol of neon was used, which suggests that the neon gas temperature in pSAM is closer to 30 K.

There are roughly 3.6 mmol of neon in a 1 in diameter, 100 μm thick solid neon film, so the amount of neon used that actually ends up frozen to the substrate is around $\epsilon = 3.6/81 \approx 4\%$. With the capillary tubing distance of 2.8 cm in v1.4, the probability of gas emanating from the end of the tube hitting the substrate is approximately 9% assuming a uniform distribution, and 17% for a cosine distribution. Therefore the 'sticking probability', defined as the percentage of atoms hitting the substrate that actually freeze to it, is in the range of 25 – 50% depending on the intensity distribution out of the tube.

3.3.4 Conclusions

A study by Schulze and Kolb [28] reports the density and refractive index of Ne, Ar, Kr, and Xe solid films over a wide range of condensation conditions by varying parameters such as substrate temperature, growth rate, and film thickness. They report no significant dependence of the density or refractive index on the film growth rate or thickness. However, they report a significant dependence

on the density and refractive index below a characteristic temperature for each gas. They conclude that at temperatures above the characteristic temperature (reproduced in Table 3.4), the solidifying noble gas atoms have sufficient mobility to form *'well-ordered crystallites with a close packed structure'*. At temperatures below the characteristic temperature, the nucleation rate increases, resulting in a *'reduction of the crystallite size'*, effectively reducing the density and refractive index. Their commentary on film transparency is limited, other than to say that films become cloudy above thicknesses of 20-30 μm.

Though the density and refractive index was not measured in pSAM, the cloudy and frosted appearance of argon and krypton films grown at temperatures at or below the characteristic temperature is consistent with the density behavior described in [28]. In contrast, depositing optically transparent 100 μm films of solid noble gases in pSAM is consistently achieved so long as the substrate is held within a temperature window during deposition, specific to each noble gas. The relevant windows are 7.5 – 8.5 K for neon, 25 – 27 K for argon, and 33 – 35 K for krypton. The initially transparent films become cloudy if the substrate temperature is maintained at the deposition temperature, but cooling the substrate after growth by 3 – 4 degrees K effectively freezes-in the initial transparency for more than 100 hours. Cooling the films by more than a few degrees K causes the films to shatter. Efficiently depositing the noble gas onto the substrate is best achieved by setting the tubing close to the substrate, at the cost of a more nonuniform film, as the intensity distribution of gas from the capillary tubing seems to be dominated by the inverse-square law.

CHAPTER 4

CALIBRATED FLUORESCENCE SPECTROSCOPY OF MATRIX ISOLATED RUBIDIUM ATOMS

4.1 Introduction

As a commissioning experiment for pSAM, a cross section measurement for the reaction $^{84}\mathrm{Kr}(p,\gamma)^{85}\mathrm{Rb}$ has been chosen due to a few favorable properties. Since the beam (krypton) is a noble gas, any unreacted beam will be implanted in the solid noble gas film (also krypton, in this case) and be optically undetectable. This reaction has a large cross section (of the order 1 mb at 2.5 MeV/u center of mass energy) which will ensure relatively fast creation of a large number of product atoms to aid in detection. Rubidium is an alkali atom with a cycling 5s ^{2}S$\rightarrow$5p ^{2}P transition at a readily accessible excitation wavelength, and exhibits a large wavelength shift between excitation and emission (see Table 2.3) when embedded in solid krypton. In this chapter, measurements of the absorption and fluorescence spectra of matrix isolated rubidium in solid krypton are presented and compared to previous measurements [21, 38].

In order to detect the number of product atoms captured in the film for a nuclear reaction cross section measurement, the intrinsic brightness of a matrix isolated rubidium atom needs to be measured. To that end, the fluorescence cross section $\sigma_f = P/I$ of a rubidium atom in krypton will be measured, where P is the power emitted by an atom under resonant excitation light of intensity I. Measuring this cross section requires implanting a known number of rubidium atoms in a krypton film and measuring the total fluorescence power emitted by those atoms under laser excitation. The number of atoms emitted by a source of rubidium atoms will be measured with a technique called atomic beam fluorescence (ABF), where resonant laser excitation intersects the atomic beam in vacuum. The vacuum fluorescence intensity from this intersection region is then used to calculate the intensity of the atomic beam. Knowledge of the atomic beam intensity and the krypton film growth rate allows for calculation of the rubidium number density in the krypton film.

4.2 Experimental Setup

A diagram of the experimental setup during solid krypton film growth with rubidium co-deposition is shown in Figure 4.1. Rubidium metal is contained in a titanium crucible fitted with a cylindrical nozzle. The high vapor pressure of rubidium ensures a significant density of rubidium gas in the crucible, which effuses out through the nozzle. The nozzle opening has dimensions of 10 cm in length and 1 mm in diameter in order to create a narrow, collimated beam of rubidium atoms. The total flux of rubidium out of the nozzle can be controlled by increasing the vapor pressure of the source rubidium through adjusting the temperature of the titanium crucible, which can be set between room temperature and 400 Celsius with the use of a resistive heating element.

Laser light from MSquared SOLSTiS Ti:Sapphire laser was aligned normal to the rubidium atomic beam and to intersect it at a distance of 35 mm from the end of the nozzle. The laser wavelength is measured with a HighFinesse WS6-600 wavelength meter. The laser beam profile was Gaussian with a diameter of 5.4 mm with a 5 MHz linewidth. The laser wavelength was scanned through the Rubidium D1 transition, and the emitted fluorescence power was measured with an avalanche photodiode (APD, Thorlabs APD410A2) located 95 mm above the intersection volume. As the fluorescence signal is small, an optical chopper (Thorlabs MC2000B) is employed to pulse the laser excitation at a frequency of 1 kHz, and the optical chopper reference signal and the APD output are sent to a lock-in amplifier (SRS Model SR530) to improve the sensitivity of the measurement. The measured fluorescence intensity is utilized to calculate the intensity of the atomic beam. The transmitted laser power is also measured with a Thorlabs PM120VA power meter. Typical ABF scan parameters and settings are listed in Table 4.1.

The rubidium atomic beam is implanted in a solid krypton during film deposition onto a sapphire substrate in the pSAM growth chamber. Krypton film growth has been previously described in Chapter 3. Optical absorption measurements are acquired with an Oceanview DH-2000 white light source and Flame Spectrometer during growth and rubidium implantation. Flow of rubidium into the film is controlled by opening and closing a gate valve between the rubidium source and the substrate.

Table 4.1: Table of ABF laser scan parameters.

Avalanche Photodiode (APD410A2) properties		
Responsivity @ 795 nm	Transimpedance Gain	Conversion Gain
13.75 $\frac{A}{W}$	500 $\frac{kV}{A}$	$6.875 \times 10^6 \frac{V}{W}$

Lock-in Amplifier (SRS SR530) settings (25 °C rubidium source)			
laser power	sensitivity	time constant	approx. signal amplitude
0.3 mW	100 μV	30 ms	2 V
4.0 mW	500 μV	30 ms	7 V

Rubidium D_1 laser scan parameters		
center λ (nm)	scan width	scan rate
794.9769	10 GHz	20 $\frac{MHz}{s}$

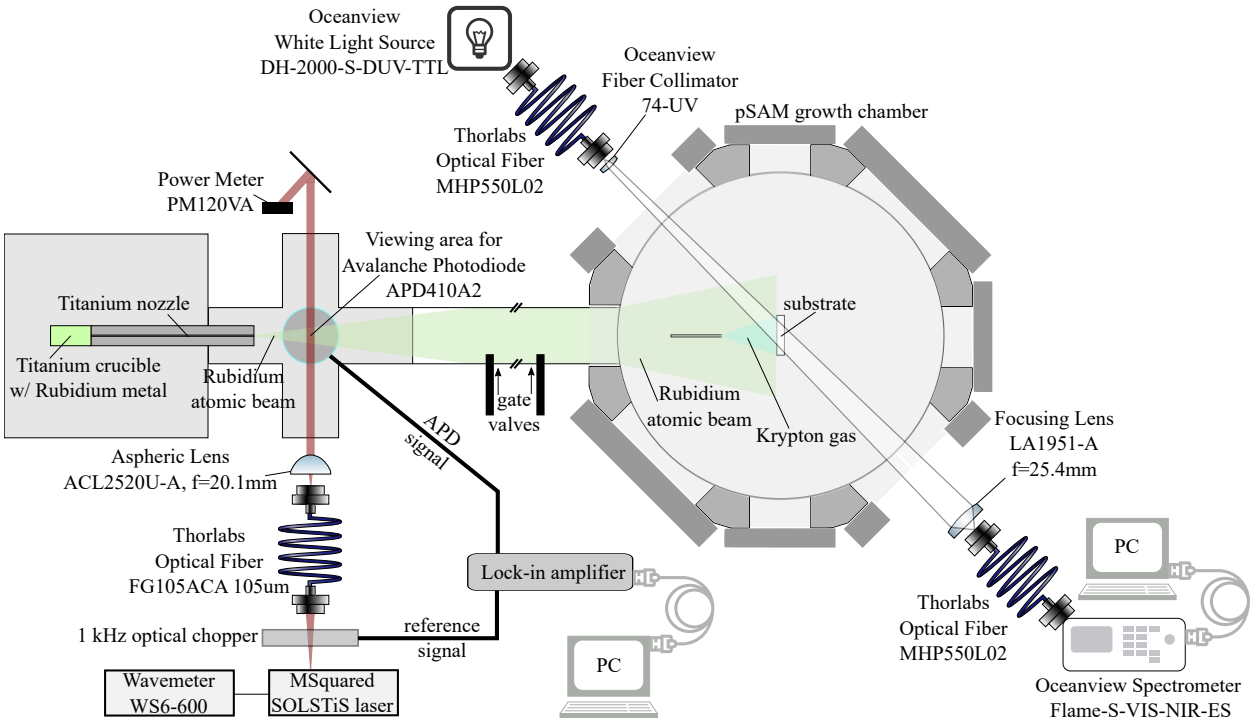

Figure 4.1: Experimental setup for rubidium atomic beam fluorescence and white light absorption of matrix isolated rubidium during a solid krypton film growth.

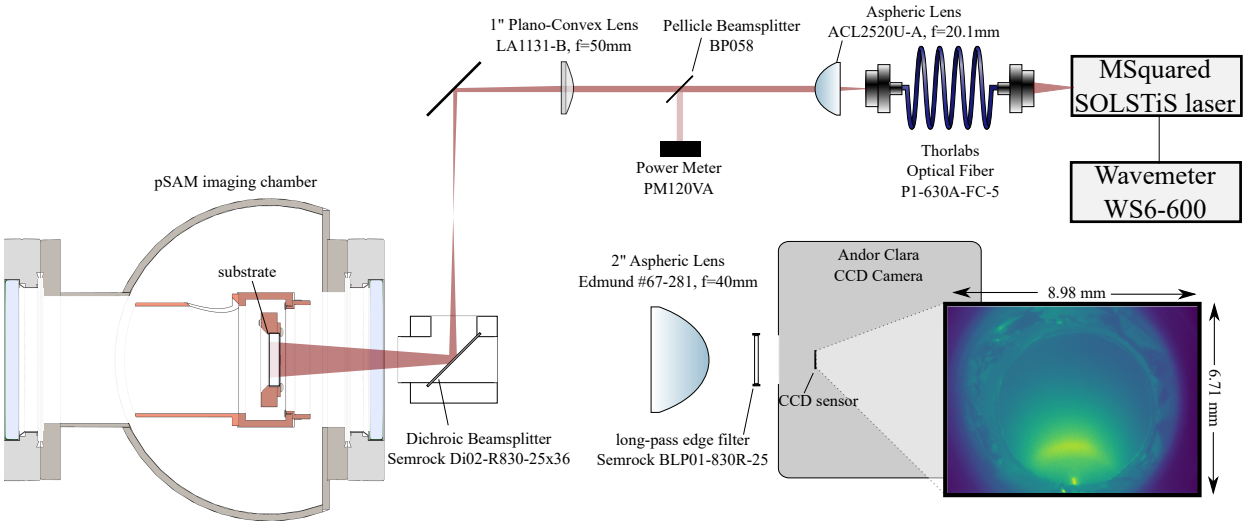

Figure 4.2: Experimental setup for fluorescence imaging of matrix isolated rubidium samples. Included is an actual image of the substrate illuminated by background light from the ion gauge. The capillary tubing for noble gas deposition is just visible at the bottom edge of the substrate (the image is inverted).

After film growth the substrate is moved to the imaging chamber for fluorescence imaging, as shown in Figure 4.2. Fiber coupled light from the SOLSTiS is collimated by an aspheric lens and sent through a focusing lens to expand the beam profile to the size of the substrate. The front surface of the substrate is imaged onto an Andor Clara CCD camera sensor with a 2 inch Aspheric lens (Edmund #67-281, f=40 mm) placed to create a 1/4-sized image of the substrate on the CCD sensor. Reflected and scattered laser excitation light is filtered by two optical color filters, a dichroic beamsplitter (Semrock Di02-R830-25x36) and a long-pass edge filter (Semrock BLP01-830R-25), both of which pass light of wavelength longer than 830 nm.

4.3 Results

Three rubidium-doped krypton films were grown at a deposition temperature of 8 Kelvin and a growth rate of 5.3, 4.7, and 4.7 μm/hr. To prepare the samples, an initial 1-μm layer of krypton was deposited on the substrate, which was followed by a layer of codeposited rubidium and krypton for a duration of 1452, 693, and 1542 s, respectively. Another layer of only krypton was then deposited until a total film thickness of approximately 5 μm was reached. This sample preparation procedure

was adapted from [21]. Samples were attempted at krypton growth rates between 13–140 μm and deposition temperatures of 34 K and 37 K, but no absorption or laser-induced fluorescence due to rubidium was observed.

4.3.1 Vacuum Rubidium Spectrum

The fluorescence power as measured by the APD is plotted as a function of excitation laser frequency in Figure 4.3 for a single scan. The scan is well represented with a fit of eight Voigt profiles and the measured hyperfine levels and splittings agree with the literature values, as summarized in Table 4.2. The Voight line profile is a convolution of Gaussian and Lorentzian lineshapes, and is defined as

$$V(\nu;\sigma,\gamma) = \int_{-\infty}^{\infty} \frac{1}{\sigma\sqrt{2\pi}} \exp\left(-\frac{\nu'^2}{2\sigma^2}\right) \frac{\gamma/\pi}{(\nu-\nu')^2+\gamma^2} d\nu', \tag{4.1}$$

where ν is the frequency, σ is the standard deviation of the Gaussian, attributed to Doppler broadening, and $\gamma = 2.875\,\text{MHz}$ is the half-width at half-maximum of the Lorentzian, which is half the natural linewidth of the transition.

Based on the amplitude of the spectra for each isotope, the measured isotopic ratio for ^{85}Rb is 0.637(69) and for ^{87}Rb is 0.363(39), while the reference data reports an isotopic ratio of 0.7217(2) and 0.2783(2) for ^{85}Rb and ^{87}Rb [2]. The fitted Voigt profiles have an average standard deviation of 178 MHz due to Doppler broadening, which corresponds to a velocity spread of v = $c\sigma/\nu_0$ = 140 m/s.

4.3.2 Rubidium Deposition Rate

The number of atoms exiting the nozzle can be calculated from the measured fluorescence intensity. The power emitted by a single atom P_{atom} under two-level resonant excitation light with intensity I is

$$P_{atom} = h\nu \left(\frac{\Gamma}{2}\right) \frac{I/I_0}{1+I/I_0} \tag{4.2}$$

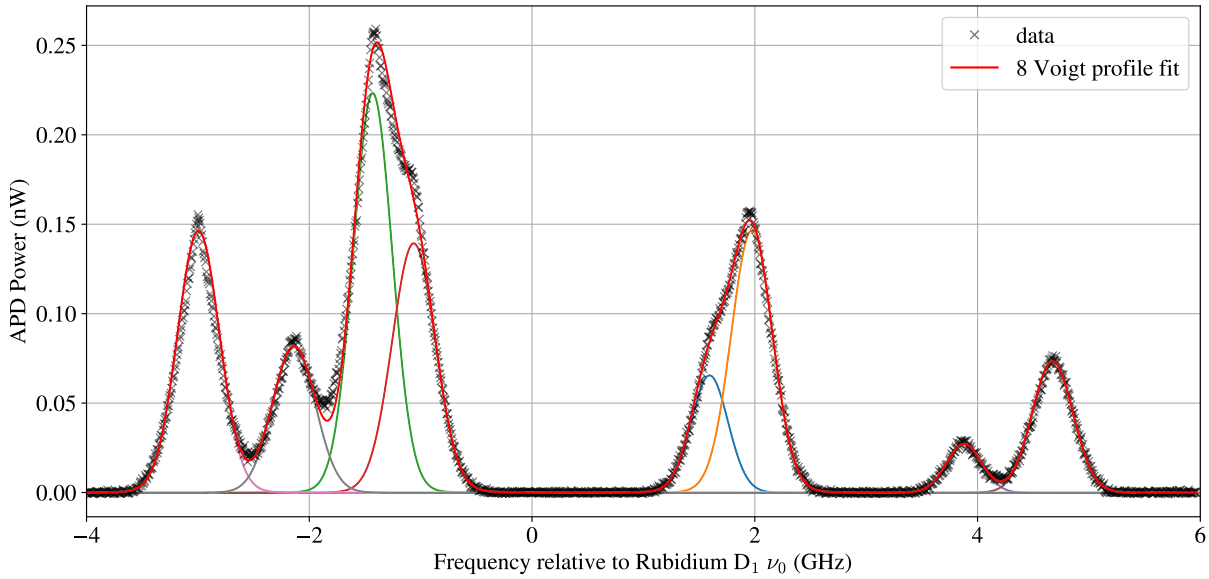

Figure 4.3: Fluorescence power as measured by the APD as the frequency of excitation light is scanned through the Rubidium D_1 transition.

Table 4.2: Rubidium D_1 hyperfine structure. Reference data is taken from [2]. Reference value uncertainties are generally less than 100 kHz. Wavelength measurements are precise to 7 MHz, with an absolute calibration accuracy of 600 MHz.

	Rubidium D_1 Transition ($5^2S_{1/2} \rightarrow 5^2P_{1/2}$)				
Wavelength	λ = 794.979 014 933(96) nm				
Frequency	ν_0 = 377.107 385 690(46) THz				
Lifetime	τ = 27.679(27) ns				
Natural linewidth	$\Gamma = 2\pi \cdot 5.75$ MHz				
Isotope shift	$\nu_0(^{87}\text{Rb})$ - $\nu_0(^{85}\text{Rb})$= 77.583 MHz				
^{85}Rb $\nu - \nu_0$, F → F' =	2 → 3	2 → 2	3 → 2	3 → 3	avg. shift
reference (GHz)	1.5599	1.9215	-1.4758	-1.1142	
measured (GHz)	1.5917	1.9715	-1.4296	-1.0618	0.0451
^{87}Rb $\nu - \nu_0$, F → F' =	1 → 2	1 → 1	2 → 1	2 → 2	avg. shift
reference (GHz)	3.8769	4.6717	-2.9919	-2.1359	
measured (GHz)	3.8388	4.6555	-2.9958	-2.1791	0.0253
level splitting	^{85}Rb $5^2S_{1/2}$	^{87}Rb $5^2S_{1/2}$	^{85}Rb $5^2P_{1/2}$	^{87}Rb $5^2P_{1/2}$	
reference (GHz)	3.0357	6.8347	0.3616	0.8166	
measured (GHz)	3.0274	6.8383	0.3738	0.8254	
difference (GHz)	-0.0083	0.0036	0.0122	0.0088	

where h is the Planck constant, ν is the frequency of the emitted photon, Γ is the excited state decay rate, and I_0 is the saturation intensity, which is defined as the intensity at which the fluorescence power is half of the saturated power $P_{sat} = h\nu\Gamma/2$. The total power measured by the APD is given by

$$P_{APD} = \int \epsilon_\Omega(x,y,z)\, P_{sat}\, \frac{I(x,y,z)/I_0}{1 + I(x,y,z)/I_0}\, n(x,y,z) \cdot dV, \tag{4.3}$$

where the integral is over the volume where the laser light of intensity $I(x,y,z)$ intersects the distribution of atoms emitted from the nozzle, described by the number density $n(x,y,z)$. The solid angle efficiency ϵ_Ω is the ratio of power detected by the APD sensor to the total power emitted,

$$\epsilon_\Omega = \frac{A_{APD}}{4\pi r^2}, \tag{4.4}$$

valid for $4\pi r^2 \gg A_{APD}$, where $A_{APD} = 0.196\,\text{mm}^2$ is the area of the APD sensor, and $r \approx 100\,\text{mm}$ is the distance from the APD sensor to a volume element.

As the angular intensity $J(\theta)$ of rubidium atoms out of the nozzle is unknown, two different models are used to calculate an upper and lower limit on the number of rubidium atoms collecting in the krypton film. Each model is displayed in Figure 4.4. The first model is a simple cosine distribution to simulate a broad, diffuse atomic beam,

$$J_1(\theta) = S_1 \frac{\cos\theta}{\pi} \tag{4.5}$$

where J_1 is the angular intensity in atoms/sr/s, S_1 is the total rate of atoms emanating from the nozzle in atoms per second, and θ is the polar angle with respect to the axis of the nozzle. The second model is taken from [65], and is derived from the distribution atoms which traverse a cylindrical channel of the same dimensions as the nozzle with radius $r = 0.5$ mm and $L = 100$ mm, while neglecting interatomic collisions,

$$J_2 = \frac{S_2}{C} j(\theta), \tag{4.6}$$

where C is a normalization constant, and

$$j(\theta) = \begin{cases} \alpha\cos\theta + \frac{2}{\pi}\cos\theta\left[(1-\alpha)R(q) + \frac{2}{3q}(1-2\alpha)(1-(1-q^2)^{3/2})\right]; & q \le 1 \\ \alpha\cos\theta + \frac{4}{3\pi q}(1-2\alpha)\cos\theta; & q \ge 1 \end{cases} \tag{4.7}$$

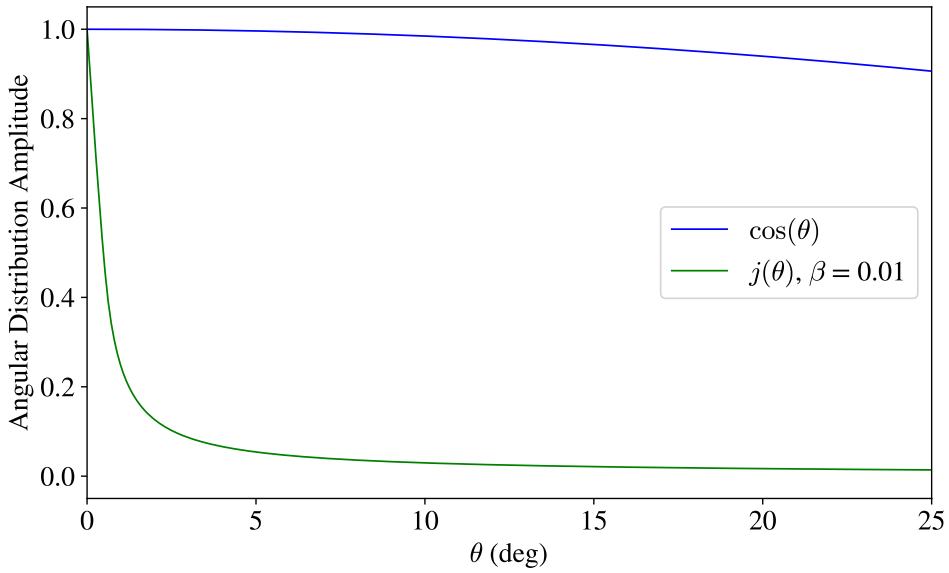

Figure 4.4: Angular intensity distribution models plotted as a function of angle relative to the centerline ($\theta = 0$) intensity.

for

$$q = \frac{L}{2r}\tan\theta, \quad R(q) = \arccos q - q\sqrt{1-q^2}, \tag{4.8}$$

and

$$\alpha = \frac{1}{2} - \frac{1}{3\beta^2}\left(\frac{1-2\beta^3+\left(2\beta^2-1\right)\left(1+\beta^2\right)^{1/2}}{\left(1+\beta^2\right)^{1/2}-\beta^2\sinh^{-1}(\frac{1}{\beta})}\right) \quad \text{with} \quad \beta = \frac{2r}{L}. \tag{4.9}$$

The number density is calculated from the angular intensity via

$$n(x,y,z) = \left(\frac{J(\theta)}{\mathrm{v}}\right)\frac{1}{x^2+y^2+z^2} \tag{4.10}$$

where (x, y, z) is the position relative to the end of the nozzle, and $\mathrm{v} = \sqrt{8k_BT/\pi m}$ is the average velocity of the rubidium atoms with mass m and temperature T.

The saturation intensity was determined by scanning the laser through the Rubidium D_1 resonance for different laser powers. The saturation intensity is extracted from a best fit to the integrated APD signal as a function of laser intensity, as displayed in Figure 4.5. With the saturation intensity and the integrated APD power, the total atomic beam current for each model, S_1 and S_2, can be

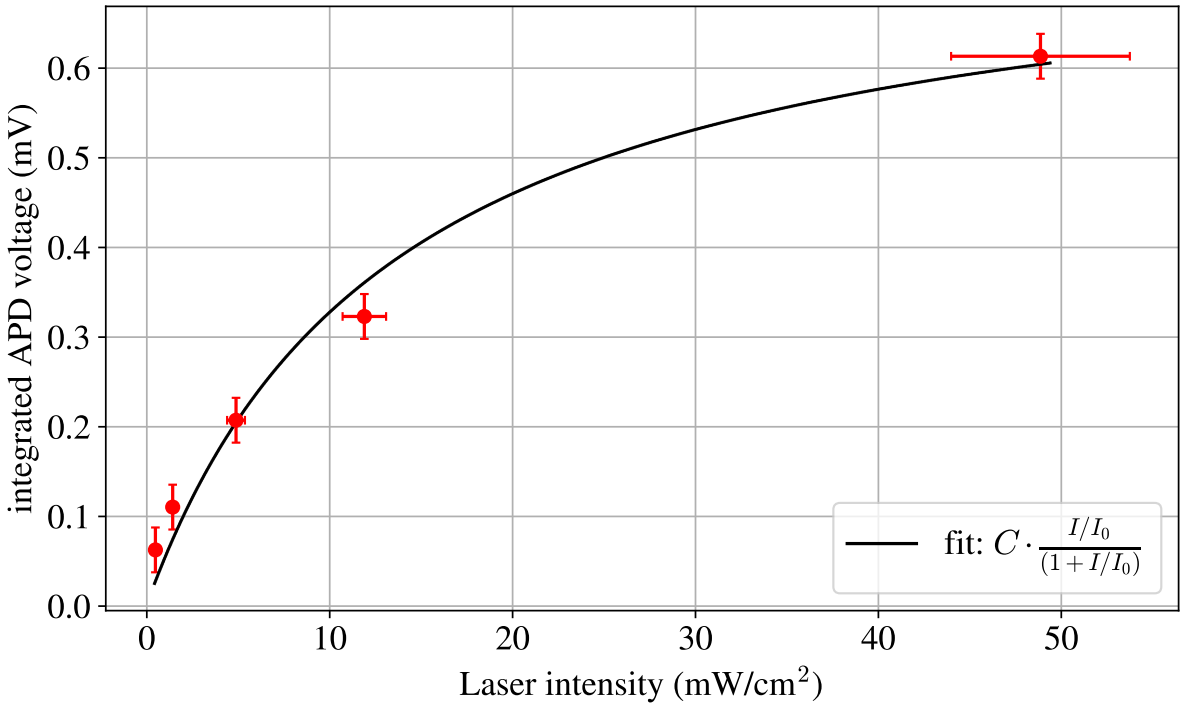

Figure 4.5: Integrated APD voltage as a function of laser intensity. A best fit to this data yields a saturation intensity $I_0 = 13.6 \pm 2.9$ mW/cm^2

calculated from Equation 4.3. The power density for each angular distribution model as detected by the APD is plotted in Figure 4.6.

Three krypton films were grown with different quantities of rubidium atoms embedded, controlled with the rubidium source temperature (rubidium current) and deposition time. The results are summarized in Table 4.3, including total atomic current out of the source S, number of atoms in the film N_{film}, rubidium number density in the krypton film n_{film}, and rubidium concentration. Upper and lower limits were determined by the J_2 and J_1 angular distributions, respectively. The number of rubidium atoms implanted in the krypton film was calculated by integrating the rubidium atomic beam intensity over the substrate in pSAM, assumed to be a circle of radius 1 cm at a distance of 85 cm from the rubidium nozzle. The largest (and dominant) source of uncertainty in the number of atoms is from the uncertainty in the saturation intensity, which contributes around 20–30 %. Uncertainty in the laser beam radius contributes a small amount (< 5 %), and the uncertainty in the

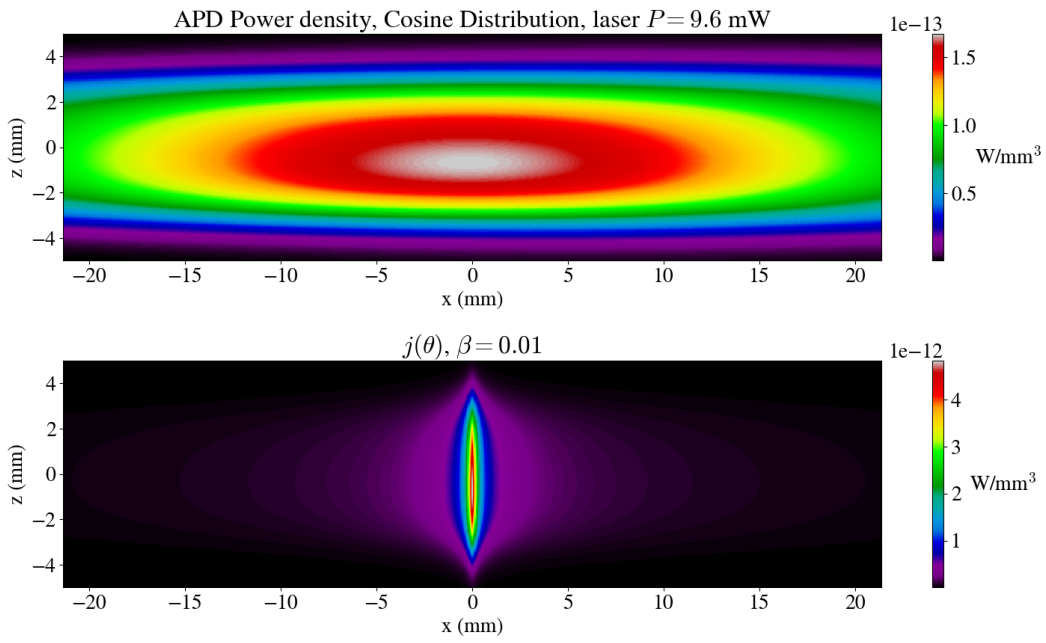

Figure 4.6: Plot of the modeled power density as viewed by the APD for each angular distribution. The plotted values are the integrand of Equation 4.3 in the $y = 0$ plane, where the center of the atomic beam and laser intersect. In this coordinate system, the nozzle tip is located at $z = -35$ mm, and the laser beam is along the x-axis centered at $z = 0$ mm. The APD sensor is located above the plotted x-z plane at $y = 96$ mm.

Table 4.3: Summary of rubidium in krypton sample concentrations.

T_{source} (°C)	dep. time (s)	Kr growth rate (μm/hr)	${}^{upper}_{lower}S$ (Rb atoms/s)	N_{film} (Rb atoms)	n_{film} (Rb atoms/cm^3)	Rb conc. (ppm)
25	1452	5.29	2.6×10^{13}	2.9×10^{13}	3.8×10^{16}	1.9
			3.1×10^{12}	6.0×10^{12}	7.9×10^{15}	0.39
116	693	4.72	1.1×10^{14}	5.6×10^{13}	1.8×10^{17}	9.0
			1.3×10^{13}	1.1×10^{13}	3.7×10^{16}	1.8
220	1542	4.65	7.9×10^{14}	8.3×10^{14}	1.3×10^{18}	65
			9.4×10^{13}	1.7×10^{14}	2.7×10^{17}	13

substrate position contributes approximately 10 %.

Table 4.4: Rubidium in Krypton absorption peaks.

λ (nm)	FWHM	note
650	30	high Rb density
705	16	high Rb density
720	12	blue triplet
731	12	blue triplet
744	30	blue triplet
765	24	red triplet
787	24	red triplet
813	24	red triplet
879	75	high Rb density

4.3.3 Rb in Kr Absorption Spectra

Absorption spectra obtained using the setup in Figure 4.1 for all three rubidium doped krypton films are displayed in Figure 4.7, and are in good agreement with previously reported spectra [38, 21]. The presence of the red and blue triplets are obvious, and additional peaks are observed for the film with the highest density of rubidium, $T_{source} = 220$ °C, that are not detected in the lower density samples. The observed peaks are listed in Table 4.4.

The absorbance $A(\lambda)$ of the film is defined as

$$A(\lambda) = -ln(T(\lambda)) = \sigma_a(\lambda)nl \tag{4.11}$$

where $T(\lambda)$ is the transmission at wavelength λ, $\sigma_a(\lambda)$ is the absorption cross section, n is the number density of rubidium atoms in the film, and l is the path length of of light through the film. Using the calculated number density of rubidium atoms in the film and the thickness of the rubidium-doped layer, it is possible to extract an upper and lower limit on the absorption cross section, plotted in Figure 4.8. The absorption cross section agrees well between the three samples.

4.3.4 Rb in Kr Fluorescence Spectroscopy

The observed fluorescence spectrum of the rubidium doped krypton film grown with $T_{source} = 220$ °C is plotted in Figure 4.9 for laser wavelengths in the range from 700 – 760 nm, with the laser scan

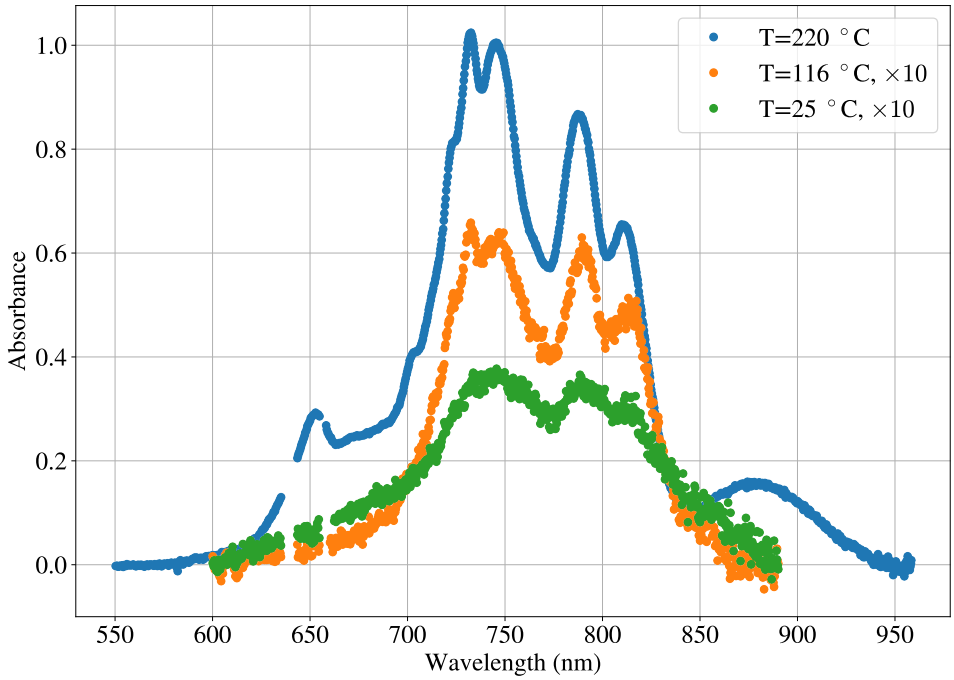

Figure 4.7: Absorption spectra of the three rubidium doped krypton films. The absorbance for films with a lower concentration of rubidium have been multiplied by 10 to aid in visibility.

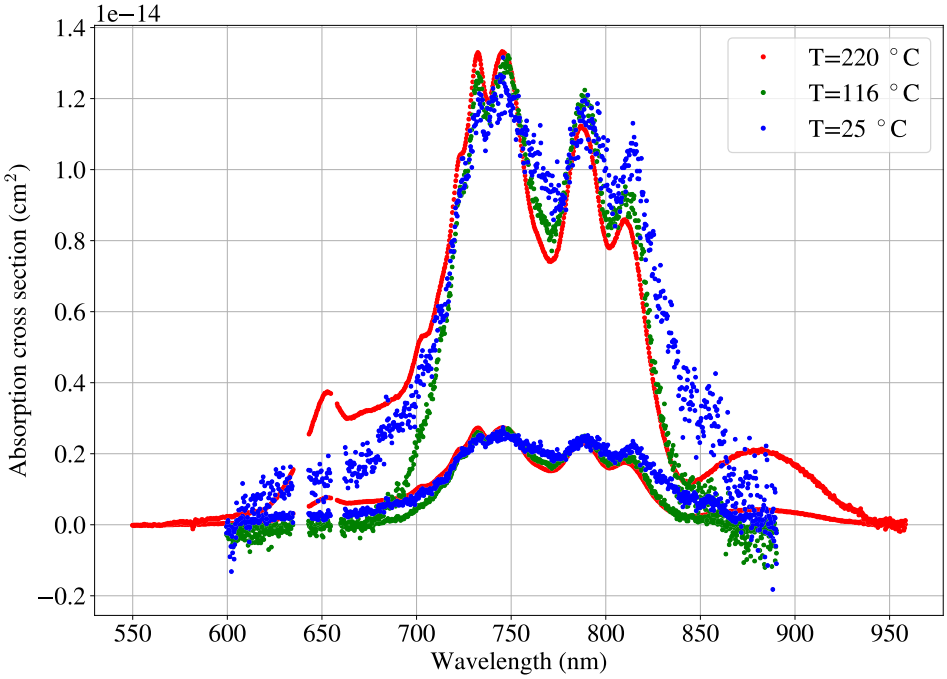

Figure 4.8: Absorption cross section of rubidium in solid krypton assuming the cosine (upper limit) and $j(\theta)$ (lower limit) angular distributions out of the rubidium source.

Table 4.5: Table of laser-induced fluorescence scan parameters for spectra in Figure 4.9.

CCD acquisition parameters		
exposure time	integrations	mode
0.8 s	6	Extended NIR
PreAmp gain	pixel readout rate	sensor temperature
1x	1 MHz (16-bit)	- 55 °C
laser scan parameters		
λ range (nm)	scan rate	
700 – 760 nm	20 $\frac{\text{GHz}}{\text{s}}$	

Table 4.6: Rubidium in Krypton laser induced fluorescence peaks, with uncertainties given in parenthesis. Resonance strength is given with respect to the amplitude of the strongest resonance at 730 nm.

λ (nm)	FWHM	strength
700.9(3)	4.1(5)	0.061(6)
714.3(5)	9.6(1.1)	0.240(9)
720.6(3)	6.6(2)	0.74(4)
730.0(3)	8.0(2)	1.000
742.5(3)	10.9(2)	0.940(8)

parameters and CCD acquisition settings listed in Table 4.5. The wavelength of the fluorescence light was not measured, but is assumed to be above 830 nm due to the longpass filters used to attenuate stray excitation light (see Figure 4.2). A recent paper reports the emission wavelength for rubidium in krypton to be 923 nm with a 37 nm FWHM for excitation in the blue triplet [21]. As the detection efficiency of the CCD camera drops rapidly for wavelengths above 950 nm, it is assumed the fluorescence measured by the CCD is 923 nm light. The fluorescence spectrum is well represented by a fit to five Gaussian functions. The average peak locations, widths, and amplitudes for all three samples are reported in Table 4.6. After measurements were completed on the first film, it was evaporated and a krypton film was grown while the atomic rubidium source was blocked. Laser induced fluorescence scans performed on the bare substrate and on the empty krypton film showed no appreciable fluorescence above background.

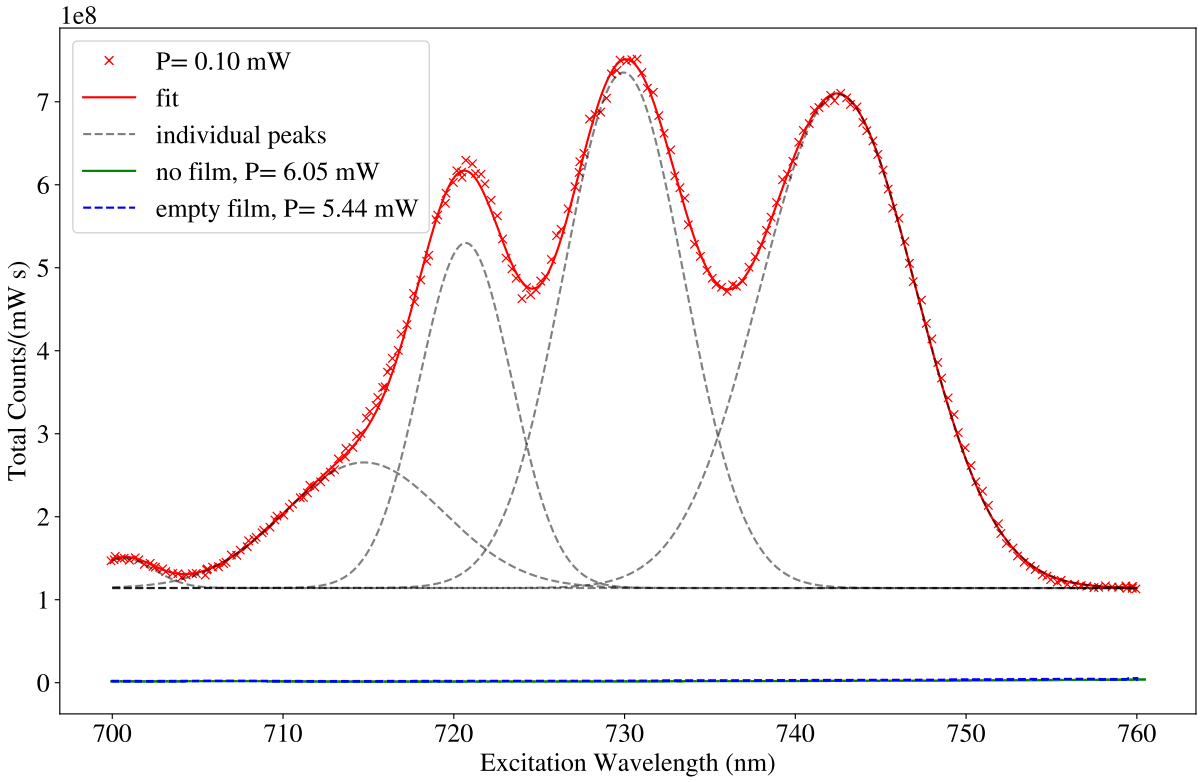

Figure 4.9: Laser-induced fluorescence spectrum for rubidium in solid krypton. The y-axis units are the total CCD count rate summed over the entire substrate and normalized to the laser power.

For each rubidium-doped krypton film, the fluorescence power was measured at 730 nm excitation wavelength over a range of laser powers, with an approximately 1-cm radius Gaussian beam profile. The third film's fluorescence yield was also measured with a higher intensity laser beam with an approximately 0.25-cm radius Gaussian beam profile. For all three films, the fluorescence yield was found to increase linearly with the laser intensity, as displayed in Figure 4.11. Due to the linear relationship, we can assume the atoms are far from saturation, and the fluorescence power per atom can be written as

$$\frac{P_{total}}{N} = \sigma_f I \tag{4.12}$$

where N is the number of atoms illuminated by laser light with intensity I, σ_f is the fluorescence cross section, and P_{total} is the total fluorescence power emitted from the laser region as measured

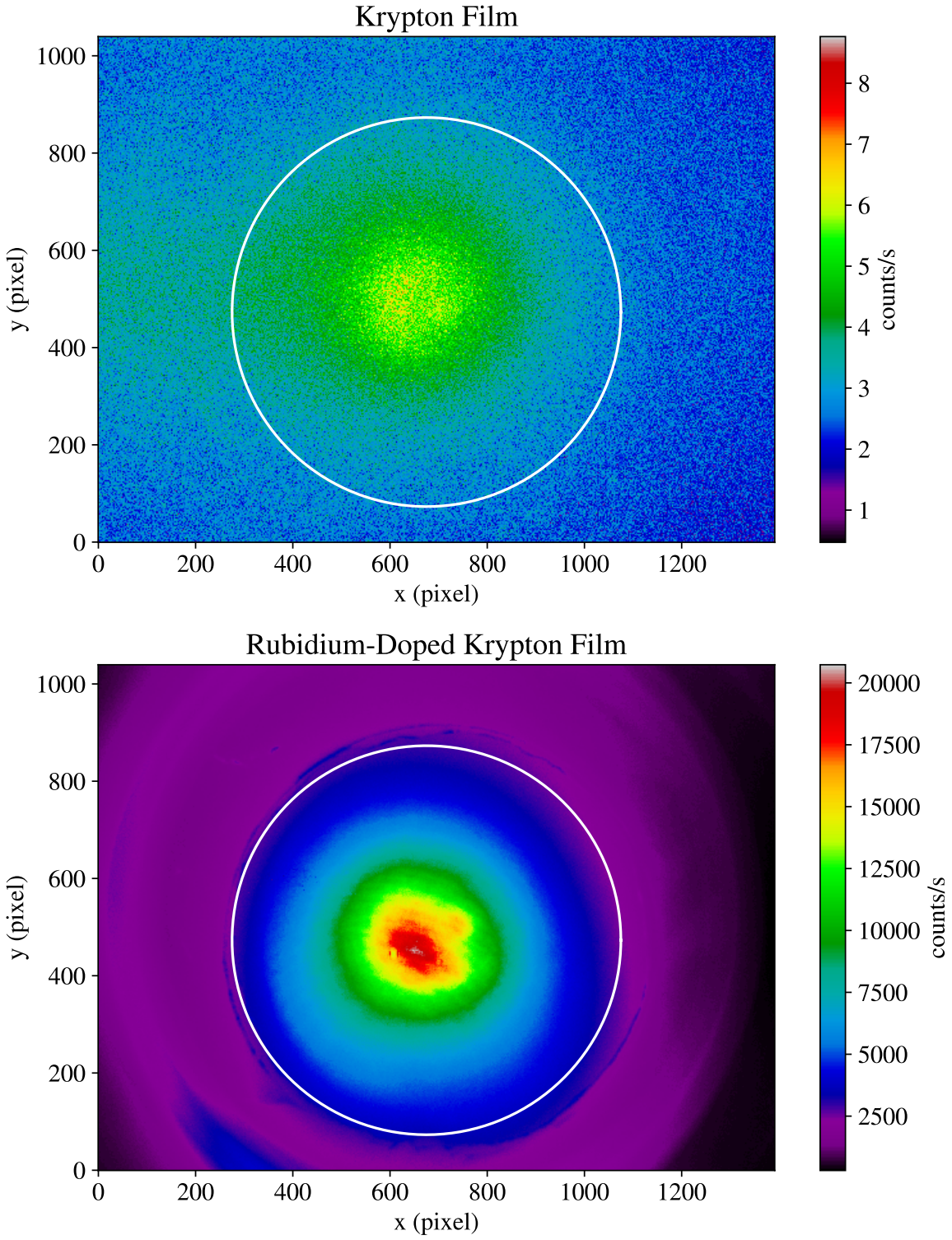

Figure 4.10: CCD images of the substrate under 1 mW of 730-nm laser light with a roughly Gaussian profile. The top image is of a substrate with a krypton film, while the bottom image is of a rubidium-doped krypton film. The white circles denote the extent of the substrate.

by the CCD camera. This total fluorescence power was calculated from

$$P_{total} = \frac{hc}{925\,\text{nm}} \cdot \frac{R_{total}}{\epsilon_\Omega} \cdot C_{CCD}(\lambda = 925\,\text{nm}) \tag{4.13}$$

where $\frac{hc}{925\,\text{nm}}$ is the assumed energy of the fluorescence photons, R_{total} is the total CCD count rate in the laser region, $\epsilon_\Omega = 0.0027$ is the solid angle efficiency of the CCD sensor relative to the substrate surface, and $C_{CCD}(\lambda)$ is a wavelength-dependent calibration factor for converting CCD counts to number of photons, which has been measured separately (see Appendix A).

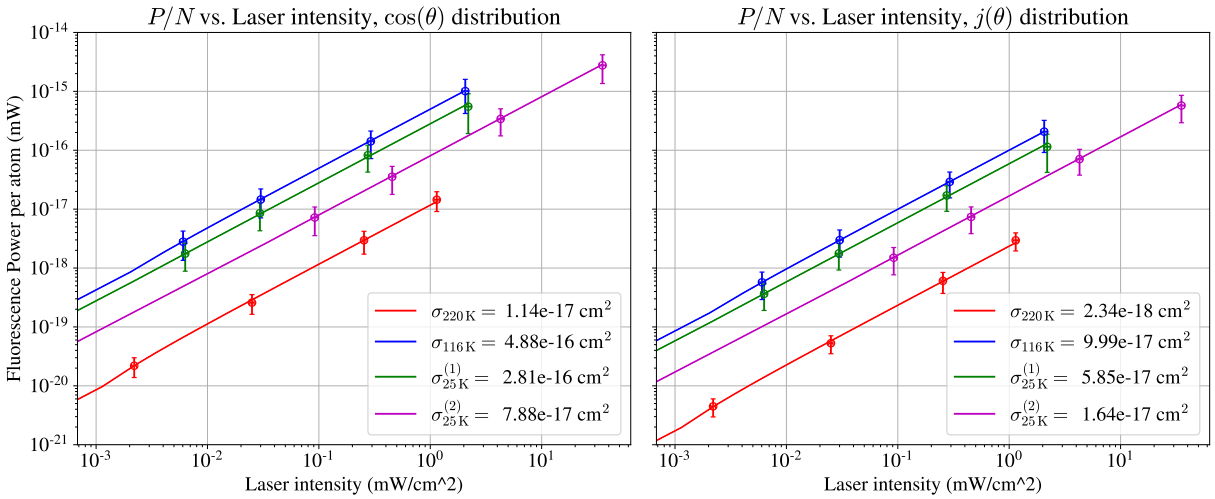

Figure 4.11: Fluorescence power per atom as a function of laser intensity for each film and for the upper and lower bounds on the predicted number of atoms in the film. The slope of each line is the fluorescence cross section σ_f.

Based on this simple model, the slope of a linear fit to the fluorescence power as a function of intensity yields the fluorescence cross section σ_f. Interestingly, each sample exhibits a markedly different σ_f as displayed in Figure 4.12. The film with the highest number density of rubidium was measured to have a fluorescence cross section an order of magnitude lower than the other two films. Even the high- and low-intensity measurements on the third film (lowest number density) are significantly different if constrained to the same rubidium angular distribution. In this third film, increasing the intensity by a factor of 16 yielded a fluorescence power increase of only a factor of 4.

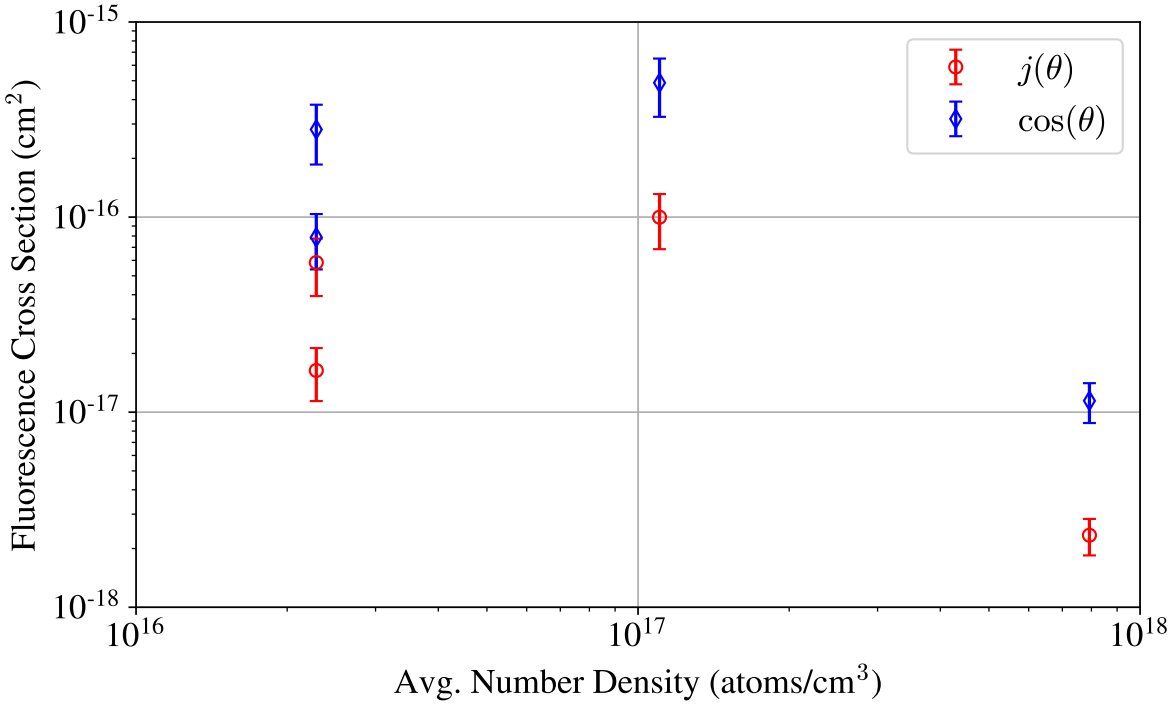

Figure 4.12: Fluorescence cross section measurements for each of the three rubidium-doped krypton films, plotted vs. the average number density calculated from the two atomic angular distribution models.

4.4 Conclusions

The absorption cross section for rubidium in solid krypton is dominated by two triplets of peaks, corresponding to two different trapping sites in the krypton lattice, as has been reported by others [21]. The absorption cross section of rubidium doped solid krypton films was measured for three different rubidium concentrations and all three were found to be consistent in magnitude. Based on this, the atomic beam fluorescence method is a reasonably accurate tool for measuring the intensity of the atomic beam source. The two extreme cases for the angular distribution of rubidium atoms out of the source yield a factor of 5 difference in the absorption cross section. Although the actual angular distribution is unknown, a cosine distribution model is most likely the reality based on the Doppler width of the ABF spectra. The Doppler width of peaks was measured to be consistent to a velocity spread of 140 m/s which roughly corresponds to an angular width of 22 degrees for 220

Table 4.7: Measured cross sections and quantum efficiencies at $\lambda_{\text{excitation}} = 730$ nm.

T_{source} (°C)	σ_a (cm^2) $\cos(\theta)$	σ_a (cm^2) $j(\theta)$	σ_f (cm^2) $\cos(\theta)$	σ_f (cm^2) $j(\theta)$	ϵ_{QE}, $\lambda_{\text{emission}} > 830$nm $\cos(\theta)$	ϵ_{QE}, $\lambda_{\text{emission}} > 830$nm $j(\theta)$
25	1.2×10^{-14}	2.4×10^{-15}	2.8×10^{-16}	5.8×10^{-17}	2.3×10^{-2}	2.4×10^{-2}
			7.9×10^{-17}	1.6×10^{-17}	6.6×10^{-3}	6.7×10^{-3}
116	1.3×10^{-14}	2.5×10^{-15}	4.9×10^{-16}	1.0×10^{-16}	3.8×10^{-2}	4.0×10^{-2}
220	1.3×10^{-14}	2.6×10^{-15}	1.1×10^{-17}	2.3×10^{-18}	8.4×10^{-4}	8.8×10^{-4}

°C gaseous rubidium atoms having an average velocity of 345 m/s. For the sharply peaked $j(\theta)$ distribution, angular width is expected to be approximately 2 degrees, which would correspond to a much smaller Doppler width of 12 m/s.

The laser induced fluorescence spectrum was likewise found to be consistent with the literature, however, the fluorescence cross section was not found to behave predictably with rubidium concentration. Although the fluorescence power was linearly dependent on the laser intensity for all three rubidium doped krypton samples, the fluorescence cross section varied by more than an order of magnitude between the different samples. If we define the quantum efficiency as the ratio of the fluorescence and absorption cross sections, $\epsilon_{QE} = \sigma_f/\sigma_a$, then ϵ_{QE} can be used as a measure of the amount of fluorescence light emitted for a certain amount of excitation light absorption. In a vacuum, $\epsilon_{QE} = 1$ due to energy conservation. In a medium, however, ϵ_{QE} can be less than 1 since absorbed energy can be transferred nonradiatively through lattice phonons. The measured quantum efficiency for the samples in this study are summarized in Table 4.7. As the quantum efficiencies in this study are on the order of 0.08–4 %, it seems nonradiative decay dissipates a significant portion of the absorbed laser excitation. In addition, this quantum efficiency seems to vary greatly between films with different rubidium concentrations, as well as for different laser beam spot sizes or locations on the film.

CHAPTER 5

BEAMLINE FEASIBILITY STUDIES

5.1 Introduction

There are a number of outstanding questions regarding the implementation of the single-atom microscope method (SAM) in a beamline nuclear reaction cross section measurement. Most importantly, as product ions are highly ionized, it is not clear what percentage of them will become fully neutralized as they penetrate and become stopped in the solid noble gas film. Depending on the product species, a singly ionized charge state can render the trapped atom optically undetectable due to unfavorable spectra. Determining this neutralization efficiency is necessary for an accurate cross section measurement, and depending on the species of interest, ensuring a high neutralization efficiency will favorably impact the SAM detection efficiency.

Another unknown is the effect that unreacted energetic ion beam will have on the noble gas thin film. Atoms are knocked out of the film as each incoming ion collides with the solid noble gas lattice in a process called sputtering. Significant sputtering could be deleterious to the SAM detection efficiency by damaging the lattice or removing significant amounts of the film such that there is insufficient remaining thickness to trap incoming product atoms. The sputtering yield, which is the ratio of ejected to incoming atoms, has not been measured for a heavy ion beam at astrophysical energies of the order of a few MeV per nucleon. Results at lower energies suggest significant thickness losses only for beam intensities above 10^9 ions/cm^2/s, described with greater detail in Chapter 2.

This chapter presents the results of the first beamline tests for the SAM detection scheme, in which the optical properties of a krypton film are studied before, during, and after bombardment by energetic krypton and rubidium ion beams. This represents an important first step towards commissioning pSAM by measuring the cross section of the ^{84}Kr$(p,\gamma)^{85}$Rb reaction. The commissioning experiment will utilize a krypton beam incident on a proton target, and the product rubidium atoms

and unreacted krypton beam are both captured in a krypton film on the pSAM substrate. In this precursor experiment, the krypton beam will be used to simulate the effects of the unreacted beam on the film, and the rubidium beam will be used to determine the neutralization efficiency of the product rubidium ions as well as confirm the spectrum of matrix isolated rubidium in krypton.

5.2 Experimental setup and procedure

For the measurements described in this chapter, the prototype single-atom microscope (pSAM) was attached to the general-purpose ReA3 beamline at the National Superconducting Cyclotron Laboratory (NSCL) at Michigan State University [66, 67, 68]. The experimental setup is similar to that in Chapter 4 except the ReA3 beamline is attached to the pSAM growth chamber in place of the neutral rubidium atomic source, as shown in Figure 5.1. During film growth and ion-beam implantation, the transmission of white light, fiber-coupled from an Oceanview DH-2000 white light source, is continuously monitored with a Flame Spectrometer (model Flame-S-VIS-NIR-ES).

The ion beam from the ReA3 facility passes through a 1-cm aperture connected to an ammeter used to monitor the portion of the beam current which strikes the aperture. A retractable Faraday cup downstream of the aperture is periodically inserted for a brief time to measure the beam current passing through the aperture. The beam current while the Faraday cup is retracted is inferred by correlation with the aperture current, assuming the portion of the total beam that is blocked by the aperture remains constant.

A $^{84}Kr^{31+}$ beam with an energy of 1.7 MeV per nucleon and 2-Hz bunched current of approximately 1×10^6 particles per second (pps) was implanted in 100-μm thick krypton films for durations of 3, 12, and 53 hours. A $^{85}Rb^{31+}$ beam, also with energy 1.7 MeV per nucleon and a current of approximately 1×10^6 pps, was implanted in krypton films for durations of 0.7, 10, 15, and 11 hours. The 0.7-hr ^{85}Rb implantation was performed on the same film used in the 53-hr ^{84}Kr implantation. After the ion beam implantation, the laser-induced fluorescence was measured for excitation wavelengths between 700–760 nm. Following the ion-implanted film fluorescence measurement, the film was sublimed and a fresh krypton film was grown for the subsequent ion beam

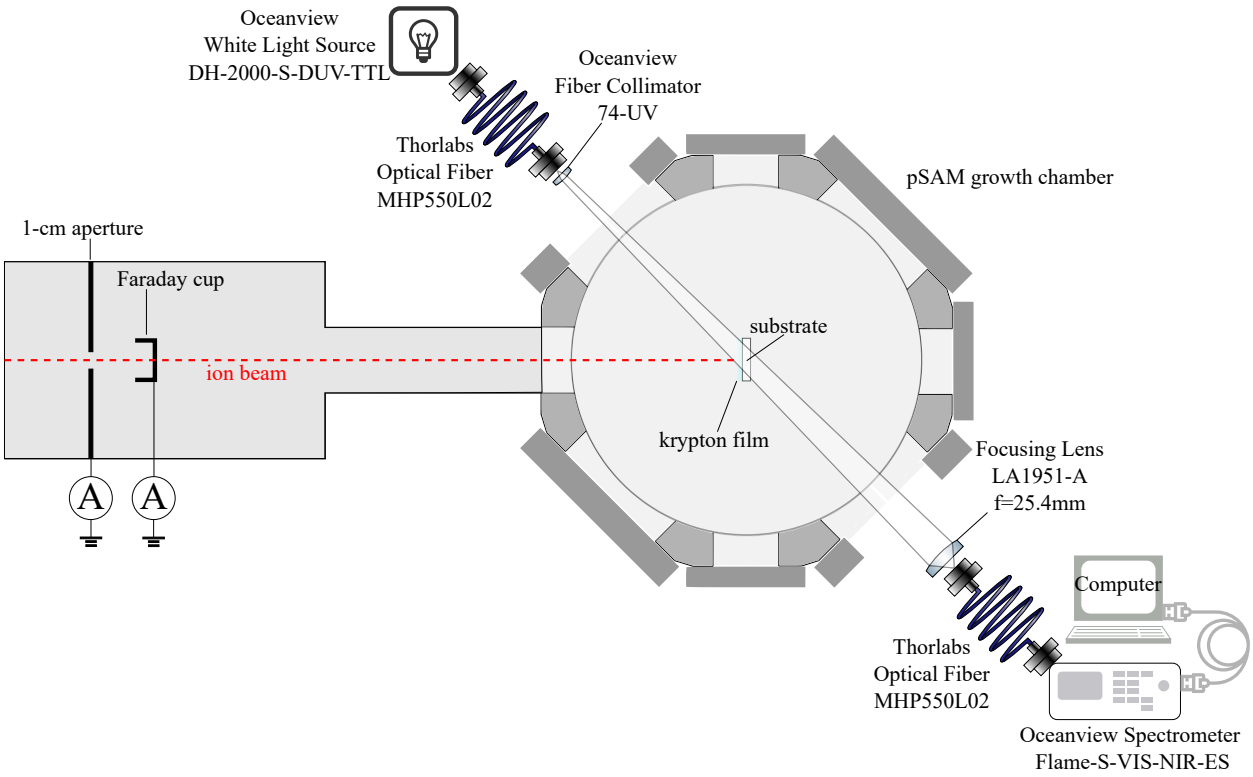

Figure 5.1: Diagram of the white light transmission measurement during ion-beam implantation.

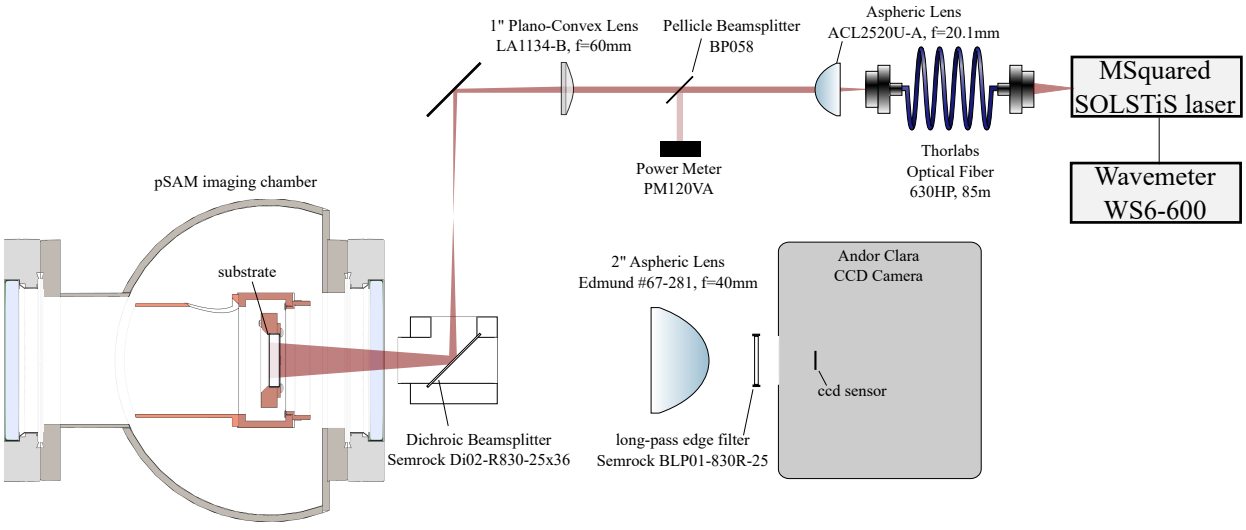

Figure 5.2: Diagram of the laser-induced fluorescence imaging setup.

implantation. Laser-induced fluorescence measurements were performed on the bare substrate after sublimation and on the fresh krypton film to establish the optical background.

The solid krypton films were deposited at a rate of 160 μm/hr with a substrate temperature of 34 K, and were cooled after deposition to 30 K at a rate of 1 K per minute. The fluorescence imaging setup used is included in Figure 5.2 and is nearly identical to the setup used in Chapter 4. Laser light from an MSquared SOLSTiS laser transported through an 85 m optical fiber (630HP), collimated with an aspheric lens, and directed onto the substrate with a mirror and dichroic beamsplitter. Upstream, the laser beam was given a divergence with the use of a focusing lens such that it was expanded to the size of the substrate, with an average intensity of 1.5 mW/cm^2. Fluorescence light from the substrate is collected by a large aspheric lens placed behind the substrate such that a 1/4-sized image of the substrate was formed on the sensor of an Andor Clara CCD camera. The dichroic beamsplitter and a long-pass edge filter, which both block light of wavelength below 830 nm, are used to attenuate any scattered or reflected laser light.

5.3 Results

5.3.1 Beam effects on film clarity

The initial white light transmission for the films is included in Figure 5.3, which shows excellent agreement between all films, with an average of 1.09 in the wavelength range 400–1000 nm. A plot of the average transmission for each film as a function of time during all ion implantations is in Figure 5.4, which also includes the average transmission for a film without an ion beam. Unfortunately, the white light source developed an intermittent instability, however, the trend is still clear. Under ion beam irradiation, the clarity of the film decreases at a slower rate than under no irradiation. This observation is confirmed with a visual inspection of the film after a significant period of beam implantation, shown in Figure 5.5. The area in which the ion beam is implanted in the film appears to remain transparent while the remainder of the film becomes cloudy. There was no measurable absorption spectra for the ^{85}Rb-implanted films, likely due to an insufficient number of implanted rubidium atoms.

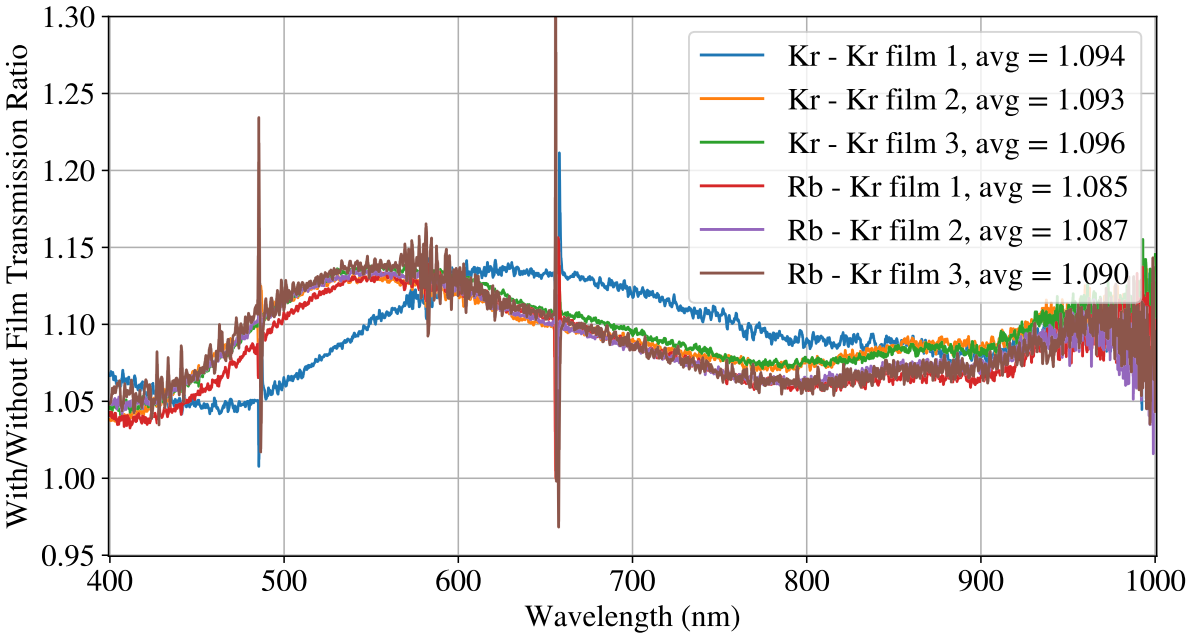

Figure 5.3: Initial transmission of light through the substrate and solid krypton films relative to transmission through just the substrate. The oscillation in the transmission is due to thin film interference in the roughly 400-nm thick krypton film which forms on the back of the substrate.

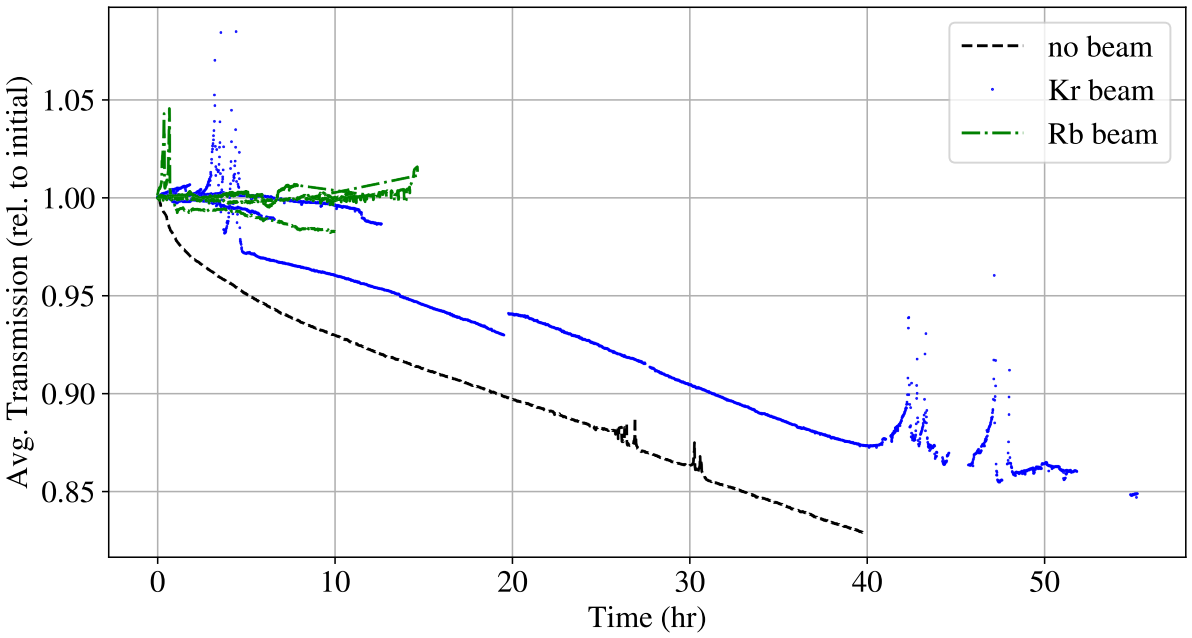

Figure 5.4: Average transmission of the films as a function of time during ion implantation. The spikes and discontinuities are due to a light source instability and not due to sudden changes in the film.

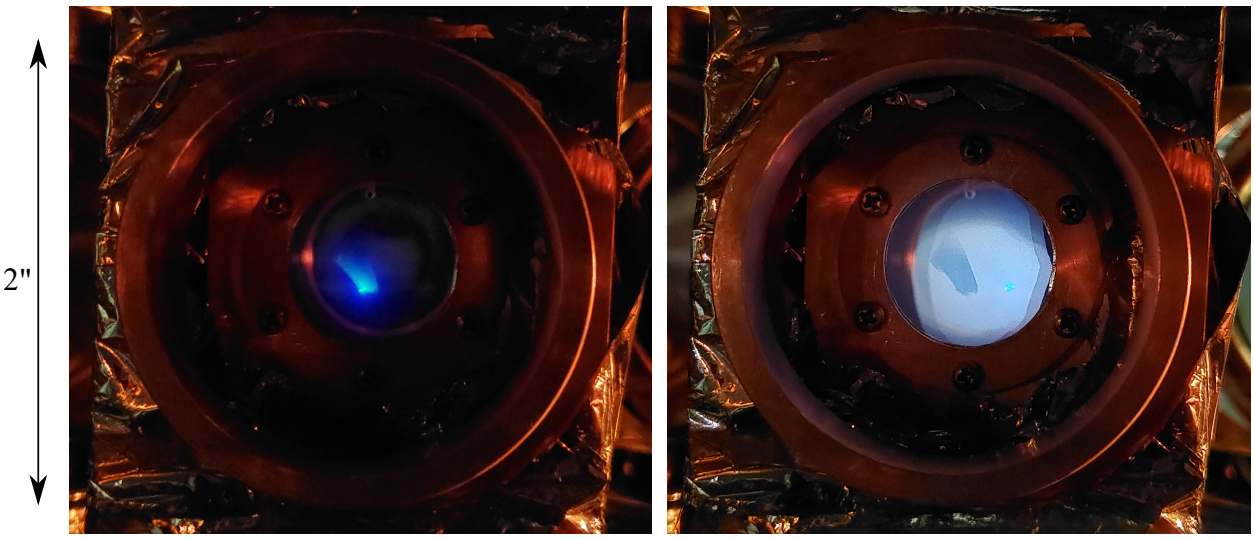

Figure 5.5: Left: As the ^{84}Kr beam collides with the film, visible fluorescence light is emitted. The white light source was blocked for this picture. Right: After 50 hr, the ^{84}Kr beam is focused onto a different spot on the film. The impression of the beam in the previous location is a large clear area in the otherwise cloudy film. The new beam location can be seen as a green spot to the right of the previous. The white light source was on and is clearly visible as an oval shape occupying most of the substrate area.

5.3.2 Ion-Beam induced luminescence

As shown in Figure 5.5, the impact of the ion beam on the film produces visible fluorescence light. The violent collision of the energetic ions causes ionization of the atoms in the film, and high energy electromagnetic radiation is emitted as the liberated electrons are recaptured. This in turn causes visible fluorescence in the film and substrate. With the white light source blocked, the spectrometer was used to take spectra with and without ion beam irradiation. The difference of the two spectra is plotted in Figure 5.6 for different implantation times during the 54-hr ^{84}Kr implantation. The spectrum consists of four main features, listed in Table 5.1, and was the same for both the ^{84}Kr and ^{85}Rb beams. The peak at 694 nm is attributed to the fluorescence of a common sapphire impurity, chromium, and the broad peak at 417 is attributed to lattice defects in the sapphire. The peaks at 525 nm and 564 nm are attributed to transitions of atomic nitrogen and oxygen, respectively, which are impurities in the solid krypton film. The amplitude of the atomic nitrogen and oxygen lines increases drastically in the first few hours of film irradiation, likely as a result of the molecular

Table 5.1: Ion-beam induced luminescence spectrum peaks. Peak locations have an uncertainty of 0.5 nm.

λ (nm)	FWHM	Assignment
416.5	47(4)	sapphire substrate [69]
524.5	1.8(2)	N film impurity (^{2}D$\rightarrow^4$S) [54]
563.8	12(3)	O film impurity (^{1}S$\rightarrow^1$D) [54]
693.0, 694.4	1.9(2)	Cr^{3+} sapphire impurity [56]

nitrogen and oxygen impurities in the krypton film becoming disassociated by the ion beam. The fluorescence of the 525 nm peak is long-lived with a 10-second decay time (see Figure 5.7), and is visible to the eye up to 60 seconds after the ion beam is blocked. The decay times of the other peaks were too short to be measured.

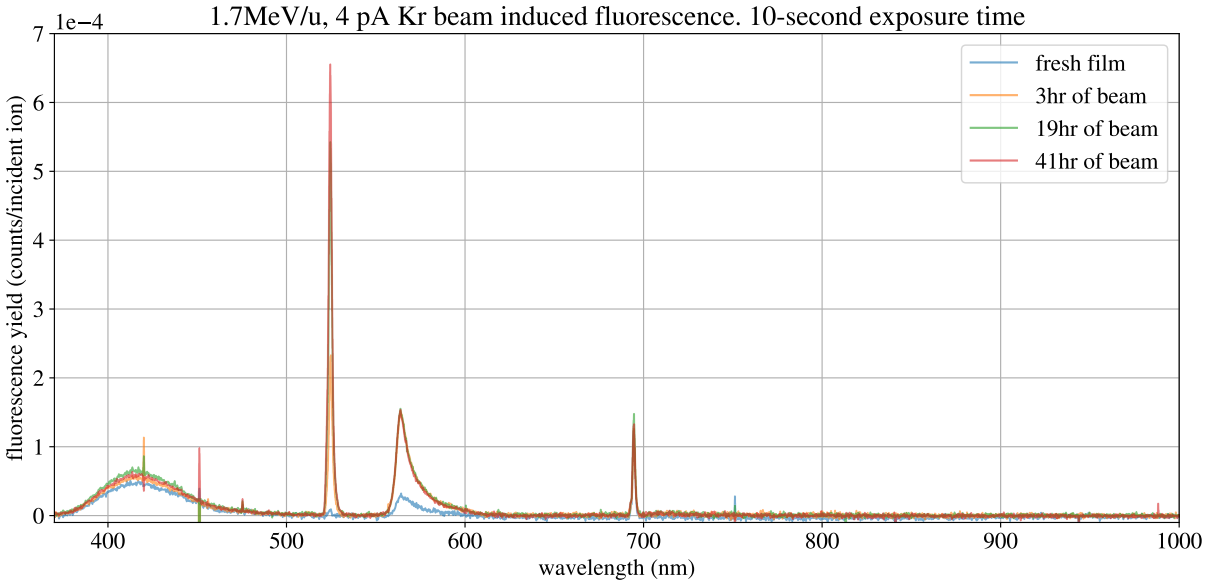

Figure 5.6: Ion-beam induced luminescence spectrum.

5.3.3 Film Sputtering

The vacuum pressure in pSAM showed no measurable difference when either beam was blocked by the Faraday cup and when the beam was hitting the solid krypton film. The vacuum pressure in pSAM with a krypton film at 30 K is typically 2×10^{-8} Torr as measured with the MKS392 Ion

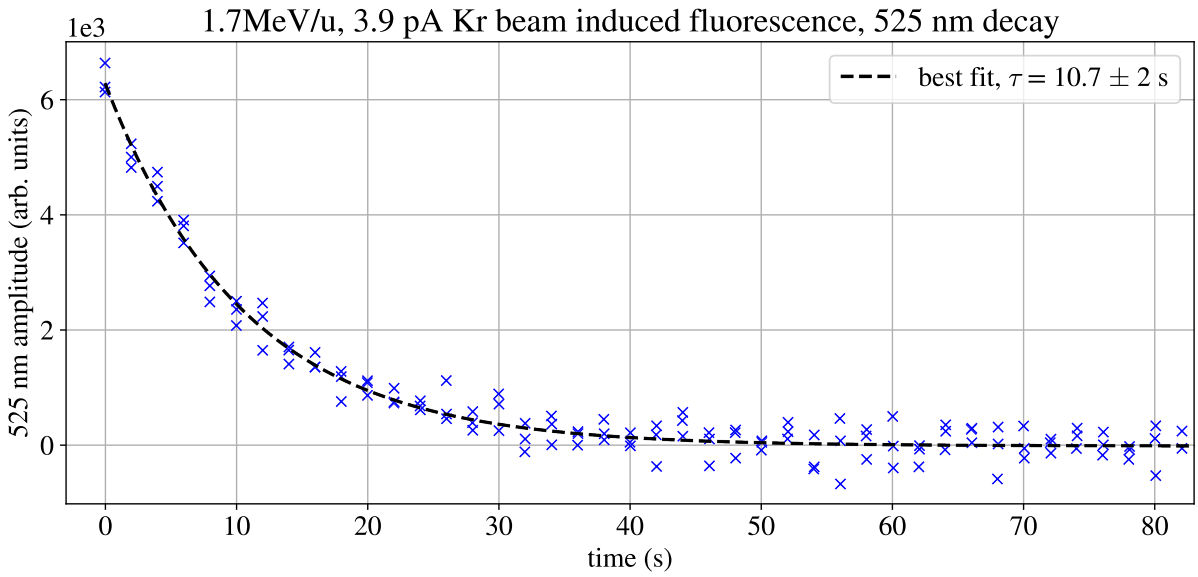

Figure 5.7: Decay of the green luminescence peak associated with atomic nitrogen, which was measured to have a roughly 10-second decay constant.

gauge, which is sensitive down to 10^{-9} Torr. An estimate of the film sputtering rate required to register with the ion gauge can be found by using the molar flow rate in Equation 3.5. Assuming the pressure increases by 1×10^{-9} Torr when the ion beam is hitting the film and a pumping speed of 55 L/s, the film sputtering rate is 3×10^{-12} mol/s. For a ion beam spot with cross sectional area of 0.2 cm^2, this corresponds to the smallest measurable krypton film thickness loss rate being on the order of 0.01 μm/hr. The typical ion beam rate was on the order of 10^6 pps, so we can put an upper limit on the smallest measurable krypton film sputtering yield for these tests to be roughly 10^7 film atoms sputtered per beam ion. This limit on the sputtering yield is orders of magnitude higher than the predicted yield of 10^3–10^5. Improving this measurement requires much higher beam currents or a much more sensitive vacuum gauge coupled with a lower overall vacuum pressure.

5.3.4 Laser induced fluorescence of ion implanted films

Films implanted with the ^{84}Kr beam displayed no significant laser induced fluorescence when compared to a freshly grown film. Figure 5.8 contains CCD images of the substrate under laser

Table 5.2: Table of laser-induced fluorescence scan parameters.

CCD acquisition parameters		
exposure time	integrations	mode
5 s	2	Extended NIR
PreAmp gain	pixel readout rate	sensor temperature
1x	1 MHz (16-bit)	- 55 °C
laser scan parameters		
λ range (nm)	scan rate	
700 – 760 nm	20 $\frac{\text{GHz}}{\text{s}}$	

excitation with a freshly grown solid krypton film and the same film after 53 hr of ^{84}Kr ion implantation (1.3×10^{11} total ions). As expected, the films implanted with the ^{84}Kr beam are generally indistinguishable from a film that has not been exposed to an ion beam. In contrast, a fluorescence image of ^{85}Rb implanted films show a clearly localized ion beam spot as displayed in Figure 5.9. The laser scan parameters and CCD acquisition settings are listed in Table 5.2

The CCD images are processed into a measure of the CCD count rate per incident laser intensity, defined as the fluorescence yield image $Y(x, y)$

$$Y(x, y) = \frac{\rho(x, y)}{I(x, y)}, \tag{5.1}$$

where $\rho(x, y)$ is the CCD image count rate in counts per second, at the array of pixels at position (x, y), and $I(x, y)$ is the excitation laser intensity in mW/mm^2. This fluorescence yield is summed over all pixels within a region of interest (ROI) to arrive at a total fluorescence yield for each image. The mean fluorescence yield over the ROI measured as a function of laser excitation wavelength is plotted in Figure 5.10 for freshly grown, ^{84}Kr beam, and ^{85}Rb beam implanted films. For ^{84}Kr implanted films the ROI encompassed the entire substrate, whereas only the localized ion beam spot was used for ^{85}Rb films to improve the signal to background ratio.

The fluorescence spectrum for the final ^{85}Rb embedded film was studied over several days under the hypothesis that some portion of the ^{85}Rb ions, which remained singly ionized after stopping in the film, would gradually neutralize over time. If such a hypothesis were true, the fluorescence

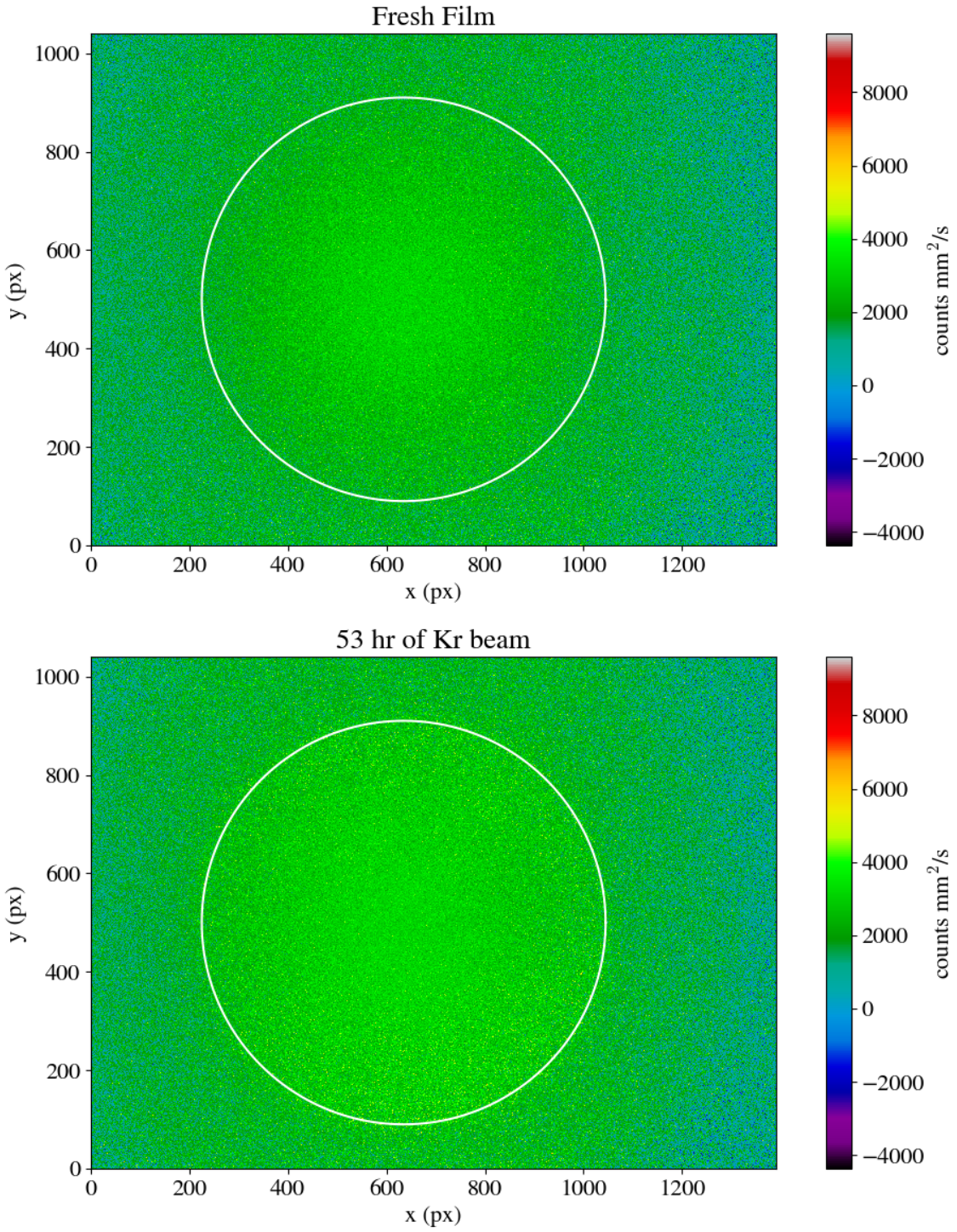

Figure 5.8: Top: CCD image of a freshly grown Krypton film. Bottom: CCD image of the same krypton film after 53 hours of ^{84}Kr ion implantation. The region of interest is shown by the white circle.

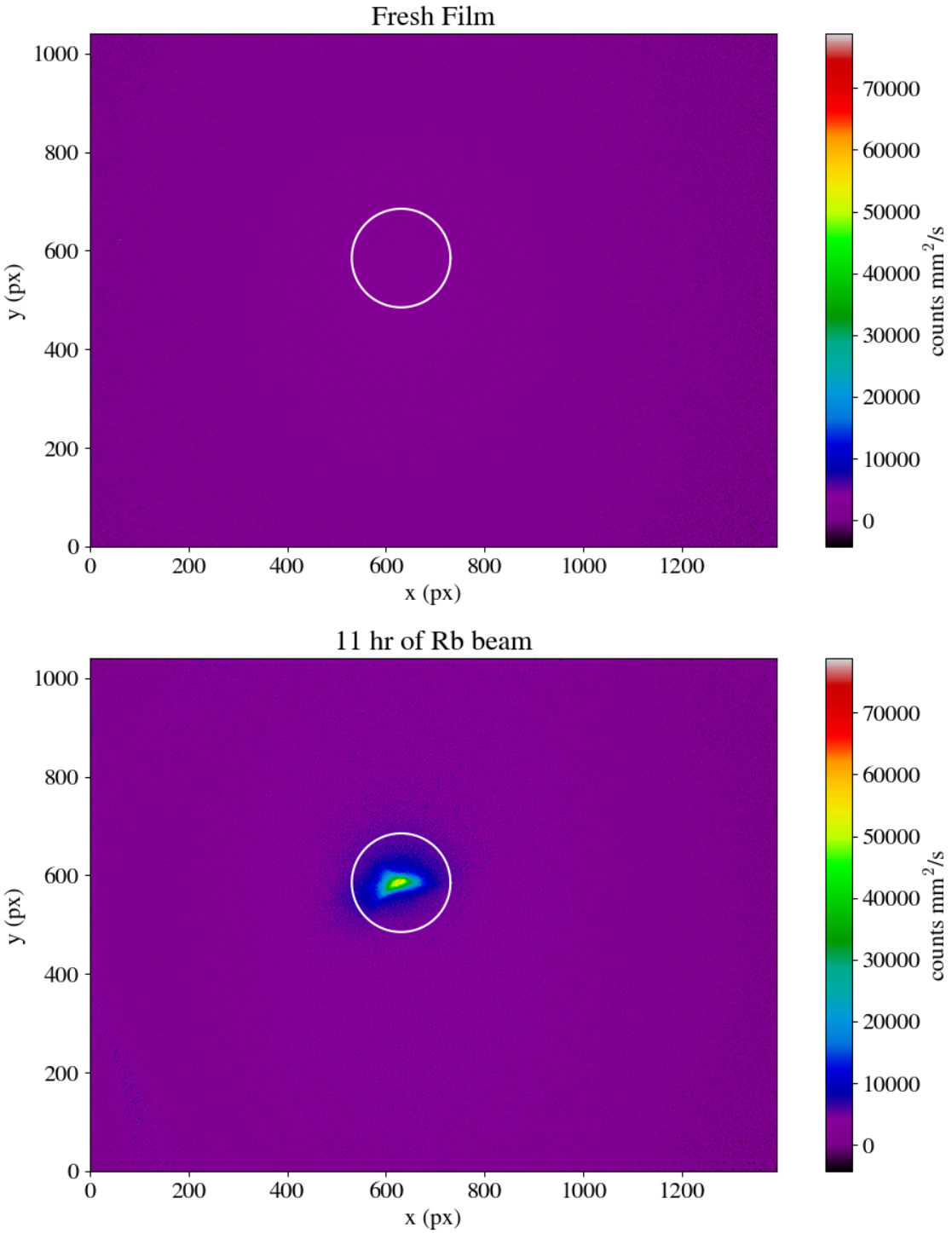

Figure 5.9: Top: CCD image of a freshly grown Krypton film. Bottom: CCD image of the same krypton film after 11 hours of ^{85}Rb ion implantation. The region of interest is shown by the white circle.

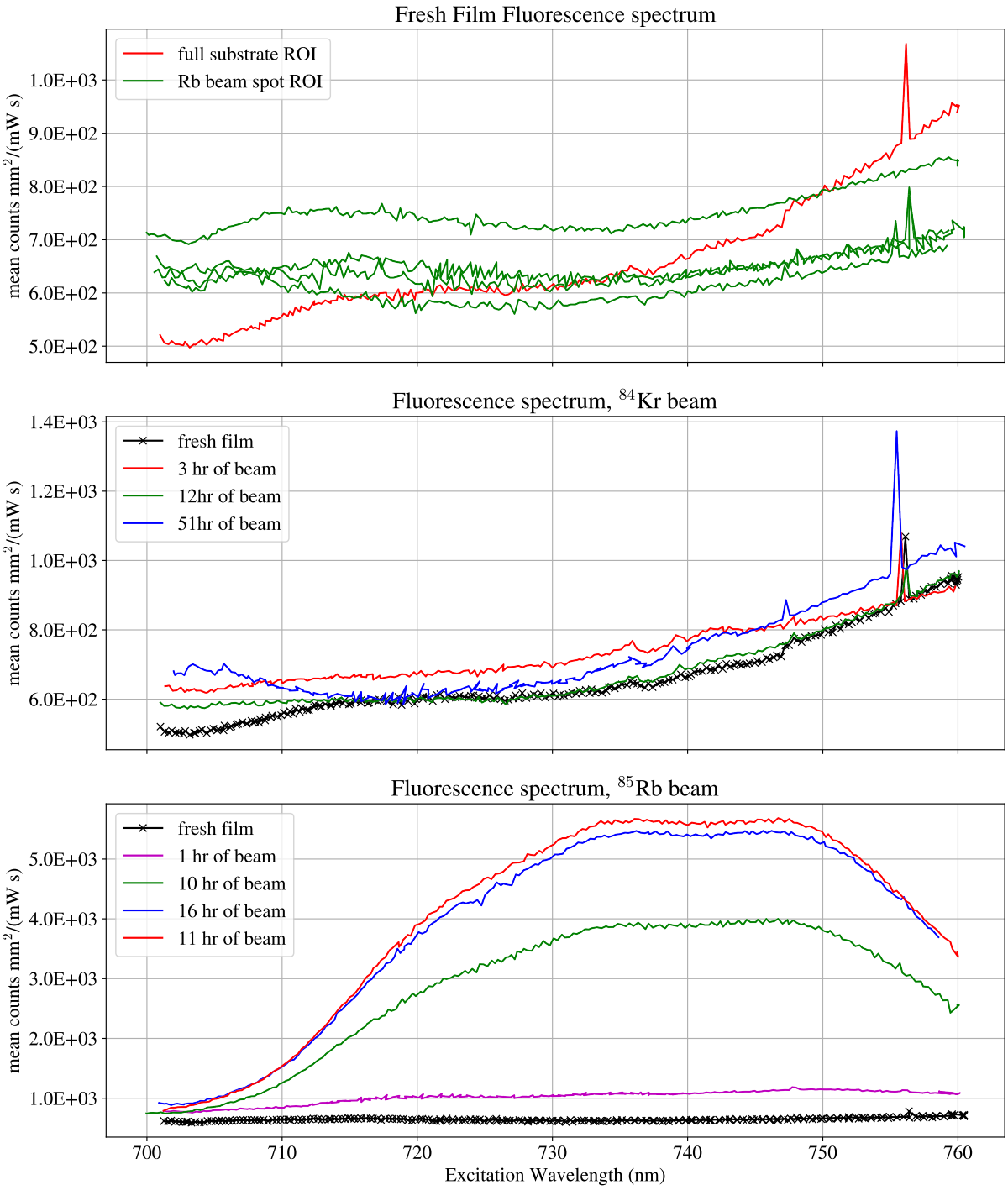

Figure 5.10: Top: Laser-induced fluorescence spectrum for a freshly grown 100-μm krypton film. Middle: Spectrum for ^{84}Kr implanted films. Bottom: Spectrum for ^{85}Rb implanted films.

Table 5.3: List of rubidium in krypton laser induced fluorescence peaks, comparing neutral and ion beam implanted rubidium.

neutral		ion beam	
λ (nm)	FWHM	λ (nm)	FWHM
720.6(3)	6.6(2)	720(1)	12(1)
730.0(3)	8.0(2)	733(1)	14(1)
742.5(3)	10.9(2)	749(1)	20(1)

Table 5.4: Maximum cross sections of ^{85}Rb implanted films, with $\lambda_{\text{excitation}}$ = 750 nm.

			uncertainties (%)		
N_{ions}	n (atoms/cm^3)	σ_f (cm^2)	δN_{ions}	$\delta\epsilon_\Omega$	δC_{CCD}
3.1×10^9	1.5×10^{12}	1.4×10^{-15}	10	11	8
6.6×10^{10}	3.1×10^{13}	6.9×10^{-16}			
8.7×10^{10}	4.2×10^{13}	7.5×10^{-16}			
8.2×10^{10}	3.9×10^{13}	8.3×10^{-16}			

yield would increase with the number of neutral ^{85}Rb atoms. However this was not the case, as shown in Figure 5.11, which shows the fluorescence yield slowly decreasing when the spectrum was measured on a daily basis for a few days after cessation of ion beam implantation. After two days, the film was annealed by raising its temperature to 38 K at a rate of 0.1 K/min, held at 38 K for 10 min, and cooled back to 30 K at 1 K/min while the laser induced fluorescence was measured at an excitation wavelength of 735 nm. Annealing resulted in a fluorescence yield decrease of a few percent as shown in Figure 5.12, which is consistent with the increased opacity of the film as a consequence of the annealing. A more aggressive annealing to 44 K had a similar effect on the fluorescence yield. When combined with the slight decrease in fluorescence yield as the film aged, we can conclude that the fluorescence yield was most likely affected by the increasing opacity of the film, and that neutralization of any trapped rubidium ions was not a measurable effect as a consequence of annealing.

After one day, the spectrum slightly changed shape as the three peaks became more distinct, suggesting that the embedded rubidium atoms do undergo some form of rearrangement in the film. The individual peaks in the spectrum are broader, less distinct, and slightly red-shifted for

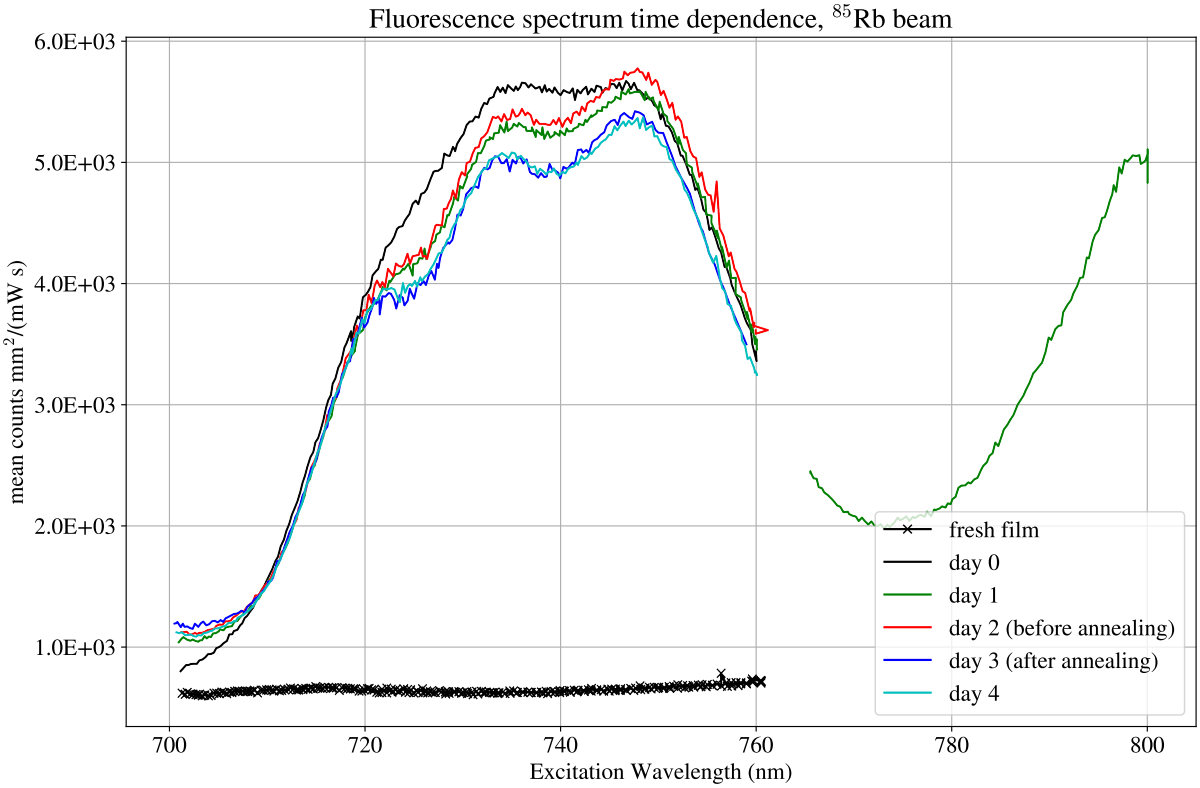

Figure 5.11: Time dependence of fluorescence spectra for a krypton film embedded with ^{85}Rb ions.

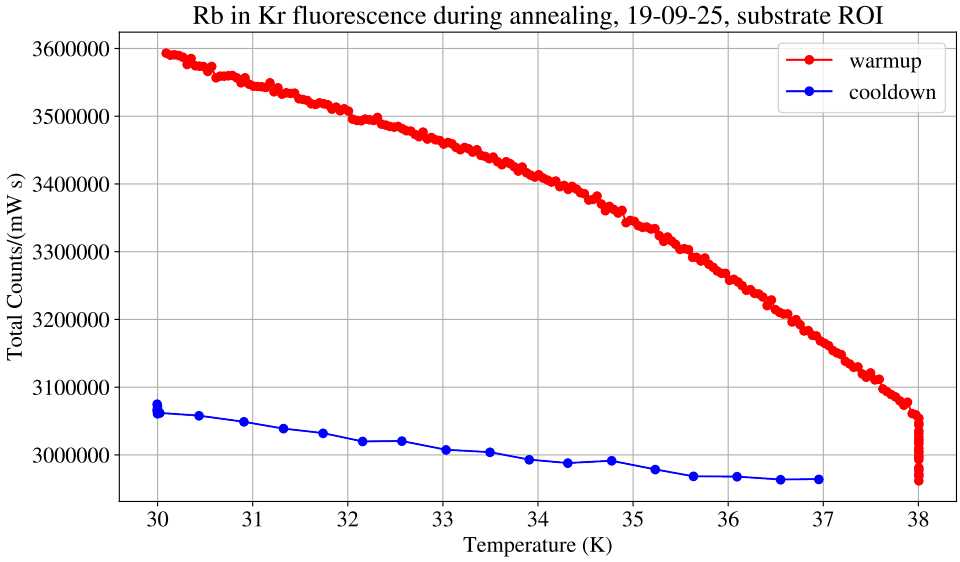

Figure 5.12: Total fluorescence yield during annealing to 38 K and subsequent cooldown to 30 K.

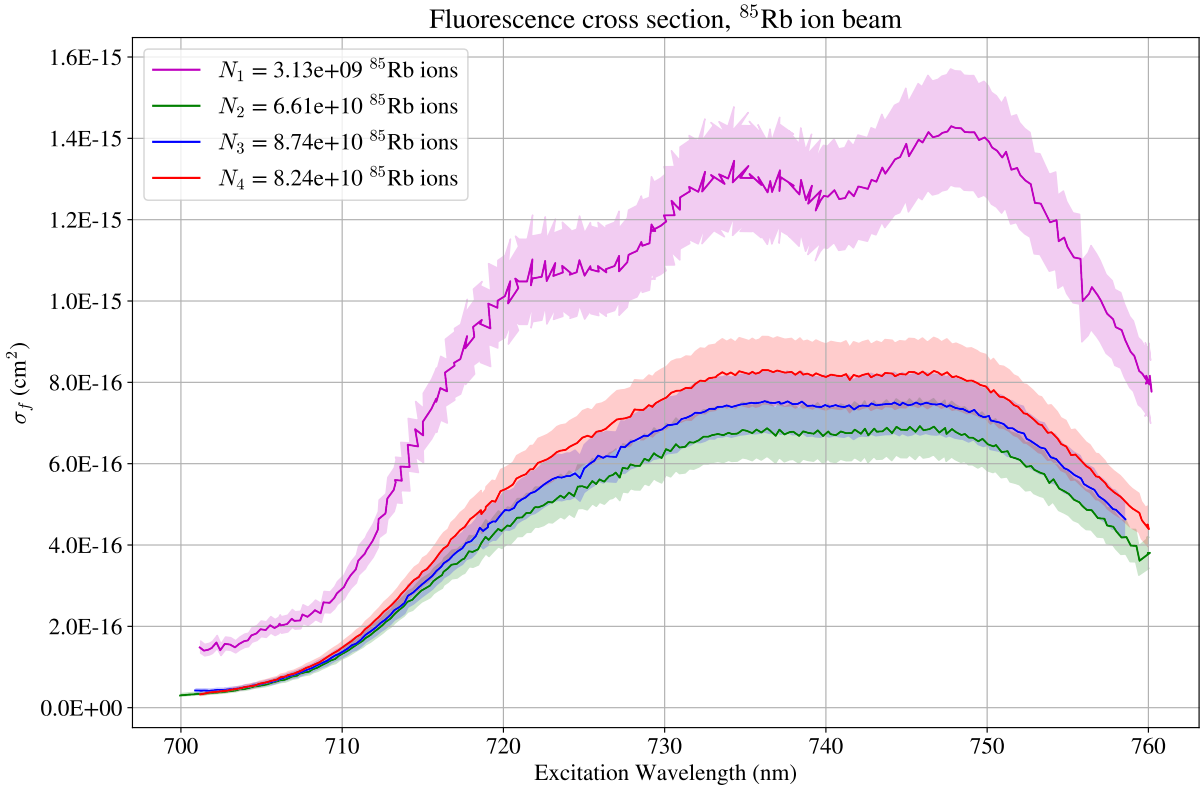

Figure 5.13: Fluorescence cross section for films embedded with ^{85}Rb ions. The shaded bands are from a 10 % uncertainty in the number of atoms implanted.

ion-implanted films compared to the neutral rubidium fluorescence spectrum detailed in Chapter 4. The peak locations are listed and compared to the neutral rubidium spectrum in Table 5.3. One measurement was extended out to 800 nm excitation to explore the tail of the third peak, and the first peak of the red triplet was found. Spectra at wavelengths longer than 800 nm was not possible to measure due to the limitations of the optical filters, and the wavelength range of the fiber employed to transport the laser light. With the total number of implanted ^{85}Rb ions, it is possible to calculate the fluorescence cross section displayed in Figure 5.13, from the total fluorescence yield Y analogous to Equation 4.13,

$$N \cdot \sigma_f = \frac{Y}{\epsilon_\Omega} \cdot \frac{hc}{925nm} \cdot C_{CCD}(\lambda = 925 \text{ nm}). \tag{5.2}$$

the peak fluorescence cross section for each sample is summarized in Table 5.4. The background fluorescence was subtracted for each measurement, calculated by summing the fluorescence yield

Table 5.5: Table of molecular oxygen resonance scan parameters.

CCD acquisition parameters		
exposure time	integrations	mode
5 s	2	Extended NIR
PreAmp gain	pixel readout rate	sensor temperature
1x	1 MHz (16-bit)	- 55 °C
laser scan parameters		
λ range (nm)	scan rate	
755.74 – 755.93 nm	50 $\frac{\text{MHz}}{\text{s}}$	

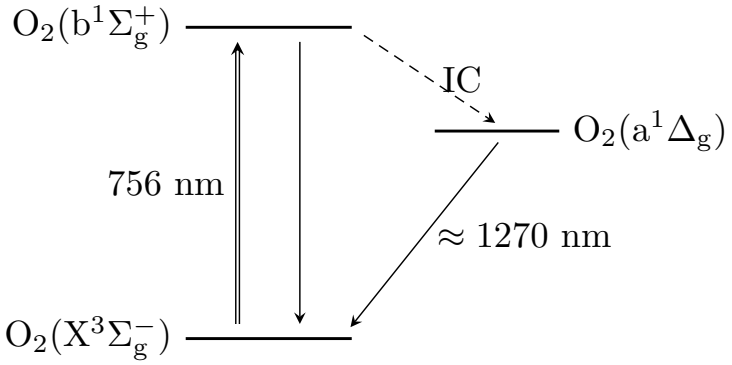

Figure 5.14: Energy level diagram for molecular oxygen transition. After excitation at 756 nm, molecular oxygen nonradiatively transfers via inter-system crossing (IC) to an adjacent lower lying state, and emits near 1300 nm.

over an ROI where the ^{85}Rb ions were not implanted.

5.3.5 Molecular oxygen fluorescence line

Through the course of acquiring fluorescence spectra of the films, a sharp, bright resonance was observed in the proximity of $\lambda_{\text{excitation}}$ = 755 nm in most spectra. This background resonance is sufficiently narrow to have not been observed with the CCD acquisition settings for laser-induced fluorescence spectra in Chapter 4, nor is it present in any white light absorption spectra. A fine wavelength scan through the resonance produced the spectra shown in Figure 5.15, with the laser scan parameters and CCD acquisition settings listed in Table 5.5. The fluorescence light in CCD

images of the substrate appeared to be distributed uniformly throughout the film, and the resonance was not observed in spectra with no krypton film on the substrate. The resonance is centered at a wavelength of 755.835 nm and has a FWHM of 0.017 nm, and appears to consist of at least two closely-spaced peaks. Since the fluorescence light appears uniformly distributed throughout the film, and due to its proximity to a molecular oxygen vacuum resonance, the background resonance is attributed to molecular oxygen impurities in the krypton film [70, 71, 72]. The molecular oxygen attribution can be further confirmed with a measurement of the $\approx$ 1270 nm emission with an infrared spectrometer, modeled by the energy level diagram displayed in Figure 5.14.

5.4 Conclusions

When embedded as an energetic ion beam, the fluorescence spectrum of rubidium in krypton varies from when neutral rubidium is co-deposited with the solid krypton film. In the ion deposition case, the individual peaks in the 700–760 nm triplet are broader, vary in relative amplitude, and the

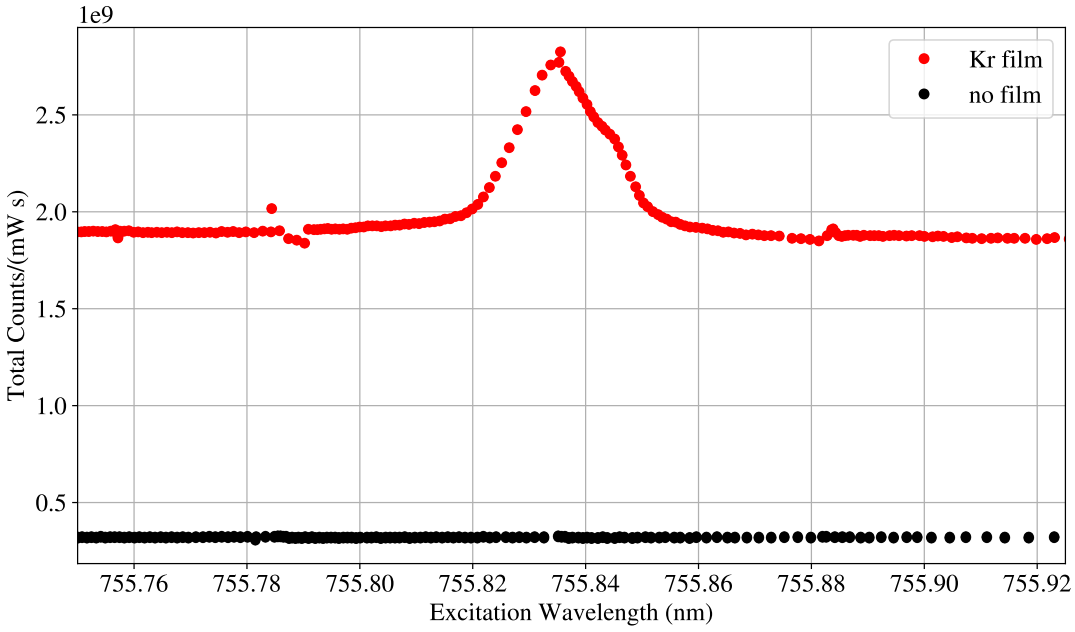

Figure 5.15: Background fluorescence line for a krypton film with rubidium ions embedded. The small spikes in the spectrum denote the ends of laser scan segments and are not actual features of the spectrum.

Table 5.6: Comparison of quantum efficiencies for neutral and ion-implanted matrix-isolated rubidium in solid krypton. Neutral absorption and fluorescence cross sections were calculated from an average of the 25 °C and 116 °C measurements in Table 4.7, and the ion-implanted fluorescence cross section is an average of all the measurements in Table 5.4.

σ_a^n	σ_f^n	σ_f^{ion}	ϵ_{QE}^n	$\epsilon_{QE}^{\text{ion}}$
(cm^2)	(cm^2)	(cm^2)	σ_f^n/σ_a^n	$\sigma_f^{\text{ion}}/\sigma_a^n$
7.7×10^{-15}	1.7×10^{-16}	9.2×10^{-16}	0.02	0.12

smaller peaks that were observed in the neutral rubidium samples are no longer present. However, the fluorescence cross section for the ion-implanted samples are comparable to, and even larger than the largest cross section estimate for the neutral rubidium samples ($\sigma_f^n = 5 \times 10^{-16}$), and the quantum efficiency for ion-implanted rubidium was significantly higher when assuming the same absorption cross section, as summarized in Table 5.6. This suggests that the neutralization efficiency for energetic rubidium ions could be close to unity. Unfortunately, the large variation in neutral rubidium fluorescence cross section measurements makes it difficult to make a quantitative estimate of the neutralization efficiency. Since the largest fluorescence cross sections were generally measured in films with the fewest number of implanted rubidium atoms, it is possible there are diminishing returns with increasing ion implantation times.

The solid krypton films were not significantly damaged by heavy ion irradiation. Sputtering of the film was not catastrophically high, nor did the energy deposited in the film by the ion beam cause significant heating or sublimation, and the ion beam did not adversely affect the transparency of the film. Instead, the ion beam counteracted the natural cloudiness that films acquire with time, and so the krypton films remained relatively transparent wherever the ion beam was implanted. Furthermore, ion beam-induced luminescence light was observed and could be used as a continuous measure of the beam current, assuming the amplitude of the beam-induced fluorescence is related to the power deposited by the beam.

CHAPTER 6

CONCLUSION AND FUTURE STEPS

6.1 Rubidium fluorescence cross section

6.1.1 Neutral Rubidium beam

An accurate measurement of the intrinsic brightness of matrix-isolated rubidium is necessary in order to be able to count the number of embedded atoms in a film. Fluorescence cross section measurements of 10^{12}–10^{14} neutral rubidium atoms that were co-deposited with the solid krypton film varied by up to a factor of 50. The largest cause of the variation is due to uncertainty in the number of rubidium atoms emitted by the effusive oven source. Since rubidium has a very high vapor pressure, a long, narrow nozzle was selected for the source in order to create a collimated and low intensity beam of rubidium atoms. Some heating is necessary to break through the surface oxidation layer on the source metal, however, there was no measurable output from the source until it had been heated to a high temperature, at which point the output became very intense and relatively uncollimated. When the crucible was removed afterwards, rubidium metal was found to have leaked out of a seam in the crucible. Future attempts would benefit from a sealed crucible to prevent leaks, and a shorter nozzle with a wider opening to allow a measurable number of rubidium atoms out of the source without requiring overheating.

Improving our understanding of the atomic beam angular distribution could be accomplished by measuring the atomic beam fluorescence (ABF) at multiple locations along the beam axis to determine the divergence of the beam. A scan of a narrow laser beam in the plane perpendicular to the atomic beam would provide a one-dimensional beam profile. With approximately 5×10^7 rubidium atoms in the laser interaction region, the ABF measurement had a signal-to-noise ratio of 100, so a reduction in the beam intensity by a similar factor should still be measurable without drastic changes to the experimental setup. Further improvements to the measurement could allow

for detection of even smaller intensities. With a brief 1-second implantation time and assuming a reduction by a factor of 100 in the 25° C rubidium deposition rate from Chapter 4, a krypton film could be embedded with only 10^7 rubidium atoms. Distributed evenly across the substrate, this would correspond to an areal density of 0.03 atoms/μm^2 in the film. With a 1:1 image of the substrate formed on the CCD sensor, with pixel area of 40 μm^2, there would be roughly one rubidium atom per pixel. Based on these estimates, the ABF method should be appropriate for creating krypton films with rubidium concentrations small enough to allow for measurements of individual atoms.

More thorough studies of the fluorescence yield of the rubidium-doped krypton films are required, as two fluorescence measurements on the same film but for different laser intensities yielded cross sections that differed by a factor of 3. The fluorescence yield should be measured for significantly higher intensities to construct a comprehensive model for the fluorescence dependence on the intensity of the laser excitation. Measurements of the fluorescence yield at several places on the surface of the substrate could also provide an additional measure of the angular distribution out of the rubidium source. The combination of an improved understanding of the matrix-isolated rubidium fluorescence and of the atomic rubidium source will be necessary to reduce the uncertainty on the fluorescence cross section.

6.1.2 Rubidium ion beam

Fluorescence cross section measurements of 10^9–10^{10} ion-beam implanted rubidium atoms were consistent to within a factor of 2, which is markedly better than the case of neutral rubidium beam, mostly due to only a 10% uncertainty on the number of captured rubidium ions. However, this uncertainty was not sufficient to account for the increased fluorescence cross section of the film implanted with the smallest number of rubidium ions. An improved understanding of the fluorescence at various laser intensities, as mentioned in the previous section, could resolve this discrepancy. Improving a measure of the neutralization efficiency for an energetic rubidium ion beam will require a more precise measurement of σ_f for neutral rubidium.

Discovery of the ion-beam induced fluorescence as well as the strong background resonance of matrix-isolated molecular oxygen offers unanticipated tools to for the single-atom microscope detection scheme. Both phenomena could be used as a measure of the concentration of oxygen impurities in the film, should impurities become an important factor for rubidium single-atom detection or for some species to be studied in the future. Ion-beam induced fluorescence of the substrate has the potential to be used as a measure of the total power being deposited by the ion beam, which can be used to infer the total beam current, an important parameter for calculation of the nuclear cross section. It may be worthwhile to explore the dependence of the beam induced fluorescence on the beam intensity in future beamline experiments.

6.2 Progress towards single-atom sensitivity

The ability to optically detect the atomic nuclear reaction products with sensitivities of the order of 1–10 atoms is crucial for the usefulness of the single-atom microscope (SAM) detection method, as well-developed methods already exist for nuclear cross section measurements with large product atom yields. Although the number of atoms detected in this thesis via fluorescence imaging is large ($> 10^9$), it is possible to estimate the feasibility of achieving single-atom sensitivity. The confidence level at which we can declare a signal exists above the background is dependent on the signal to background ratio. The number of background and signal counts measured over a certain integration time is simply the rate multiplied by the integration time. The uncertainty associated with the signal and background counts are determined according to counting statistics,

$$\begin{aligned} N_s \pm \sigma_s &= R_s t \pm \sqrt{R_s t}, \\ N_b \pm \sigma_b &= R_b t \pm \sqrt{R_b t}, \end{aligned} \tag{6.1}$$

where N_s is the number of counts measured during integration time t, due to an atom emitting at a rate R_s, and N_b is the number of background counts measured during integration time t, due to a background rate R_b.

For large count rates, the distribution of repeated signal measurements approximately follows a normal distribution [73]. The expected fraction (f) of measurements following a normal distribution

that fall within k standard deviations σ of the mean is given by the Error Function:

$$f\left(\mu \pm k\sigma\right) = \mathrm{erf}\left(\frac{k}{\sqrt{2}}\right), \tag{6.2}$$

$$\mathrm{erf}\left(x\right) = \frac{1}{\sqrt{\pi}}\int_{-x}^{x} e^{-u^2}\,du. \tag{6.3}$$

For a given measurement $N_s \pm \sigma_s$, the probability p that the signal is significantly different from zero, called the confidence level, is determined via

$$N_s - 0 = k\sigma_s \quad \rightarrow \quad k = \frac{N_s}{\sigma_s} \tag{6.4}$$

$$p = \mathrm{erf}\left(\frac{k}{\sqrt{2}}\right). \tag{6.5}$$

In reality, we have no means of distinguishing the atom signal from the background during an individual measurement. Having made a measurement of the total signal N_T (atom and background), we must make a separate measurement of just the background rate with no source atoms and subtract to get the single atom signal.

$$N_s = N_T - N_b \tag{6.6}$$

$$\sigma_s = \sqrt{\sigma_T^2 + \sigma_b^2} = \sqrt{R_T t + R_b t} \tag{6.7}$$

From Equation 6.4,

$$k = \frac{(R_T t - R_b t)}{\sqrt{R_T t + R_b t}} = \sqrt{R_T t}\cdot\frac{1 - \frac{1}{\eta+1}}{\sqrt{1 + \frac{1}{\eta+1}}} = \sqrt{R_T t}\cdot\frac{\eta}{\sqrt{\eta^2 + 3\eta + 2}}, \tag{6.8}$$

where $\eta = R_s/R_b$ is the signal to background ratio. Using Equation 6.8 we can determine the integration time t necessary to achieve a confidence level p as a function of signal to background ratio η, which is plotted in Figure 6.1,

$$t = \frac{1}{R_T}\cdot 2\left[\mathrm{erf}^{-1}\left(p\right)\right]^2\cdot\frac{\eta^2 + 3\eta + 2}{\eta^2}. \tag{6.9}$$

For the largest measured fluorescence cross section ($\sigma_f = 1.4\times10^{-15}$ cm^2), over the ion beam ROI with 3.1×10^4 pixels (circular area of radius 100 pixels), containing a total of 3.1×10^9 rubidium

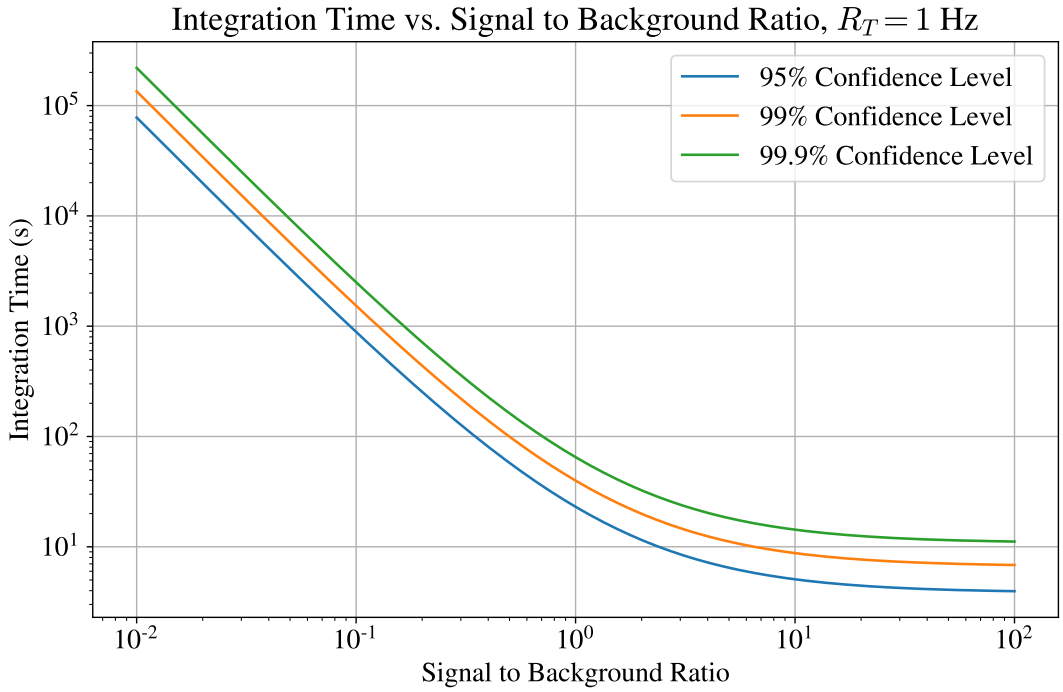

Figure 6.1: Required integration time t as a function of signal-to-background ratio η for different confidence levels, assuming a total signal rate of 1 Hz.

atoms (giving an average of 10^5 atoms per pixel), and with laser intensity $I = 2.5\,\mathrm{mW/cm^2}$, the CCD measured an average signal rate per pixel of $R_T = 25$ counts/s with a background rate of $R_b = 17$ counts/s. This gives an average pixel signal-to-background ratio of $\eta = (R_T - R_b)/R_b = 0.47$, and a signal-to-background ratio per atom of $\eta_\mathrm{a} = 4.7 \times 10^{-6}$. Evaluating Equation 6.9 with η_a, $R_T = 25$ Hz, and a confidence level $p = 0.95$ gives an integration time of $1.4 \times 10^{10}\mathrm{s} = 440\,\mathrm{yr}$. It is important to note that these spectra were acquired under conditions not specifically intended for single-atom detection, and that achieving a more reasonable 60-second integration time, requiring reduction by a factor of 2×10^8, can feasibly be accomplished by maximizing η and increasing the total signal rate. In comparison, a recent publication demonstrating single barium atom detection in solid xenon reported, under 3-s exposure to laser excitation with intensity $I \approx 10^5\,\mathrm{mW/cm^2}$, a background rate of $R_b = 1000$ counts/(mW·s) and a per-atom signal rate of $R_s = 380$ counts/(mW·s), for a signal-to-background ratio of $\eta_a = 0.38$ [57].

A relatively low laser intensity was employed in the rubidium fluorescence measurements in

order to image the entire substrate. Focusing the laser excitation onto a circular area of radius 25 μm could drastically increase the signal rate by as much as a factor of 10^4, assuming both the signal and background rate scale linearly with laser intensity. To make a more conservative estimate, assume the signal rate increases linearly with intensity up to a factor of 10^2. A further factor of ten increase in R_T can be found in increasing the light collection efficiency of the imaging lens by placing it closer to the substrate. The light collection efficiency for the imaging system used during fluorescence imaging was estimated to be 0.0027, which can improve to as high as 0.023 with the current pSAM imaging chamber. Combining these improvements results in up to a factor of 10^3–10^5 increase R_T, and corresponding decrease in the required integration time.

The greatest reduction in t, which scales with $1/\eta^2$ for small η, can be accomplished through maximizing η by minimizing the background rate R_b, which should be reduced by at least a factor of 10^3. The main source of background measured by the CCD is most likely laser light reflected by the substrate that is insufficiently attenuated by the optical filters. The two filters are a dichroic beamsplitter (Semrock Di02-R830-25x36) used to reflect the laser excitation onto the substrate, and a long-pass edge filter (Semrock BLP01-830R-25) placed immediately upstream of the CCD sensor. From the manufacturers specifications, the upper limit for the transmission at 750 nm for the dichroic beamsplitter is approximately 10^{-4} and 10^{-7} for the long-pass filter. These transmissions were independently verified as is displayed in Figure 6.2. Placing the filters in series should provide a transmission on the order of 10^{-11}, however measurements of the series transmission at 725 nm, using the setup in Figure 6.3, results in a combined transmission of only 10^{-7}, as shown in Figure 6.4. The laser power from the SOLSTiS laser was measured before and after the dichroic beamsplitter using calibrated power-meters (Thorlabs PM120VA), and the laser power transmitted by the long-pass filter was measured by the Andor Clara CCD camera, which was previously calibrated (detailed in Appendix A). The dichroic beamsplitter behaves as predicted, with a transmission of 10^{-4}, but the long-pass filter attenuates the laser light transmitted through the beamsplitter by only a factor of 10^{-3} instead of 10^{-7} measured previously. The long-pass filter is significantly less effective for light already attenuated by the beamsplitter.

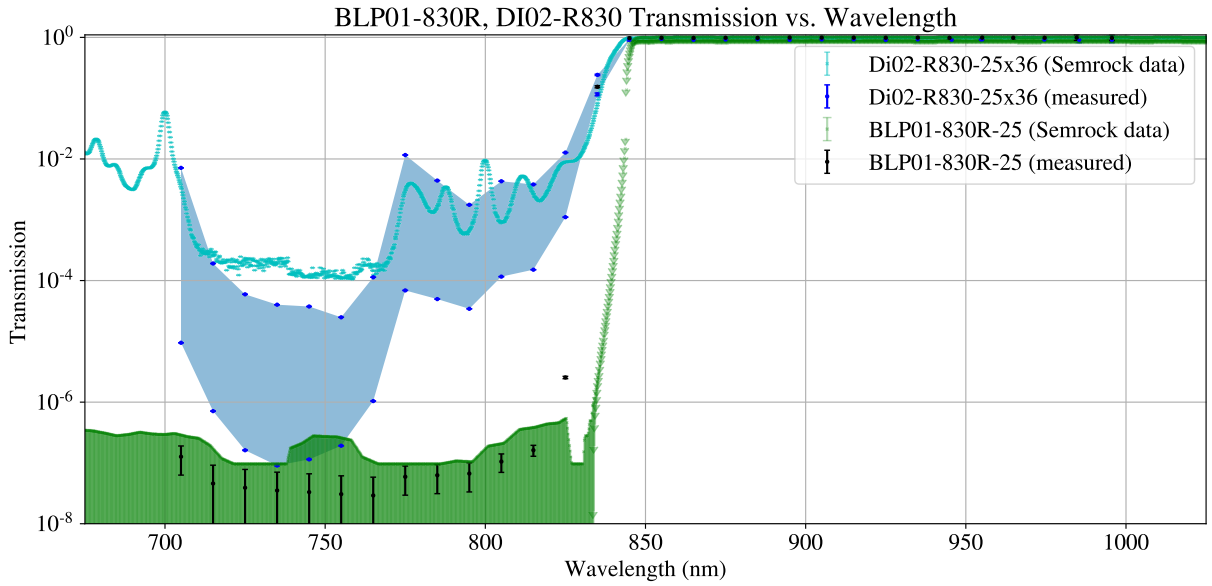

Figure 6.2: Transmission of Semrock filters utilized in fluorescence imaging. The transmission of the dichoic beamsplitter, measured at an incident angle of 45° was strongly dependent on the polarization of the incident light as shown by the shaded blue region. The transmission of the individual elements met or exceeded the manufacturer's specifications.

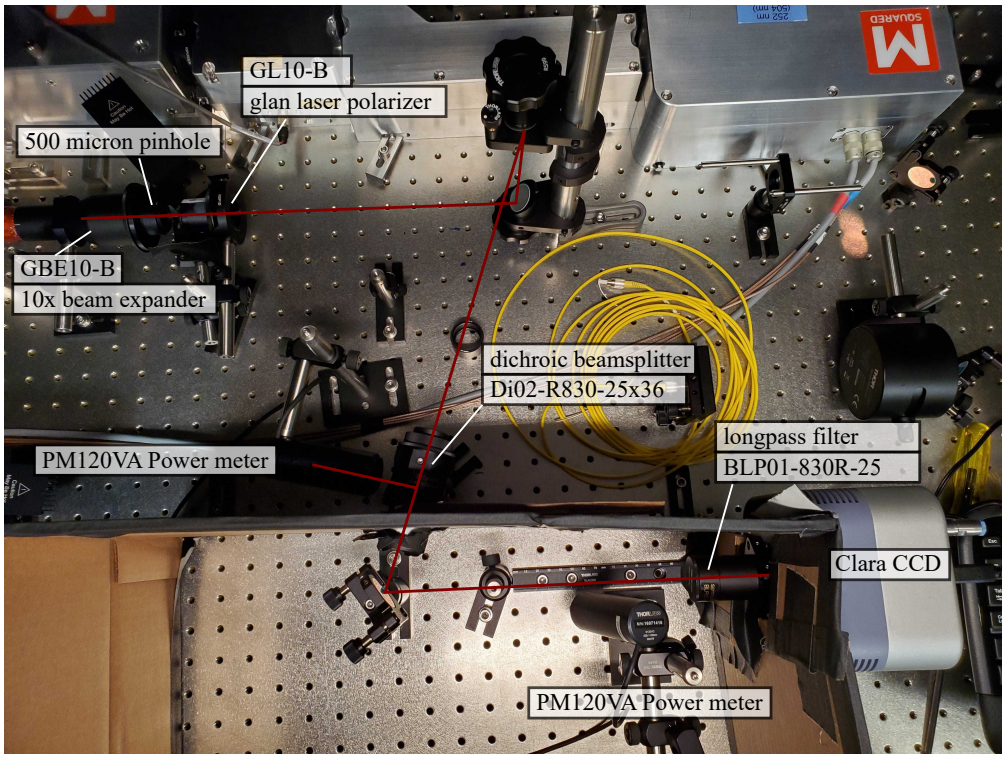

Figure 6.3: Setup used to measure the transmission of the Semrock filters in series.

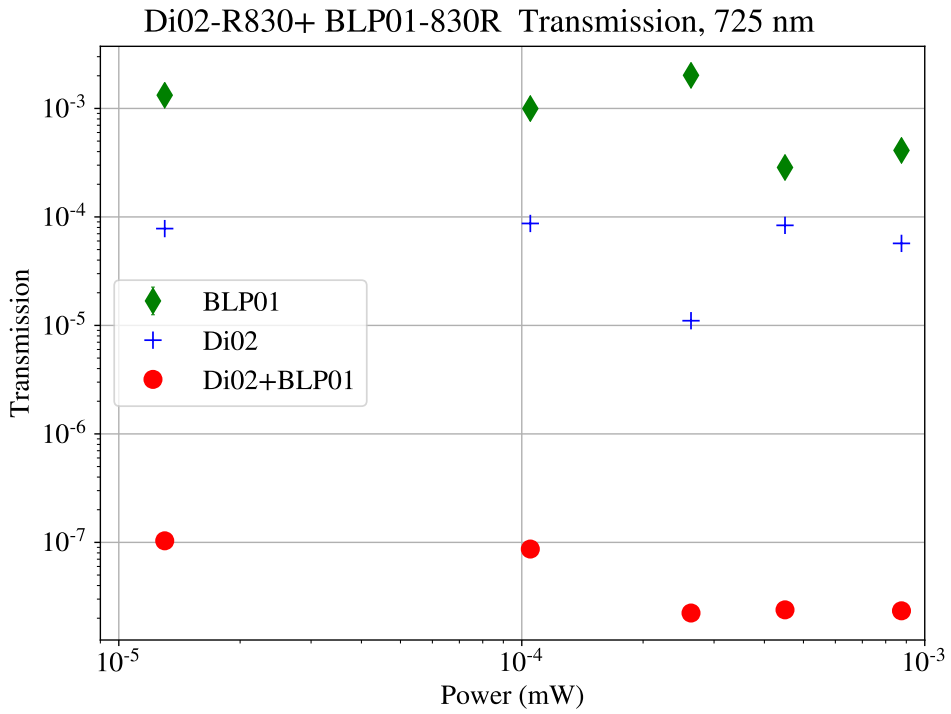

Figure 6.4: Transmission of the Semrock filters measured at different laser powers. The combined transmission of the filters is a factor of 10^4 larger than predicted, based on the individual transmissions.

Using the measured transmission of the filters in series, we can estimate this background rate with

$$R_b = I \cdot \frac{\lambda}{hc} \cdot \delta \cdot \epsilon_\Omega \cdot T \cdot C_{CCD} \cdot \frac{1}{M} \cdot A_{\text{pixel}} \approx 9\,\text{counts/pixel/s} \tag{6.10}$$

where $I = 2.5\,\text{mW/cm}^2$ is the laser intensity, $\lambda/hc = 3.77 \times 10^{15}\,\text{photons/mJ}$, $\delta = 0.08$ is the reflectance of the substrate, $\epsilon_\Omega = 0.1$ is the light collection efficiency assuming 10% of the reflected light is collected by the imaging lens, $T = 10^{-7}$ is the estimated transmission of the optical filters at 750 nm, $C_{CCD} = 0.74\,\text{counts/photon}$ is the CCD efficiency, $M = 0.25$ is the magnification of the imaging system, and $A_{\text{pixel}} = 4.16 \times 10^{-7}\,\text{cm}^2$ is the area of a pixel. This rough estimate is within a factor of 2 of the measured background rate. Unfortunately, the Andor Clara CCD used for these measurements is biased toward the background light in this case, since the efficiency at 750 nm is significantly higher than at 925 nm, which is the rubidium emission wavelength ($C_{CCD}(750\text{nm})/C_{CCD}(925\text{nm}) \approx 5$). The background could also be due to fluorescence in the

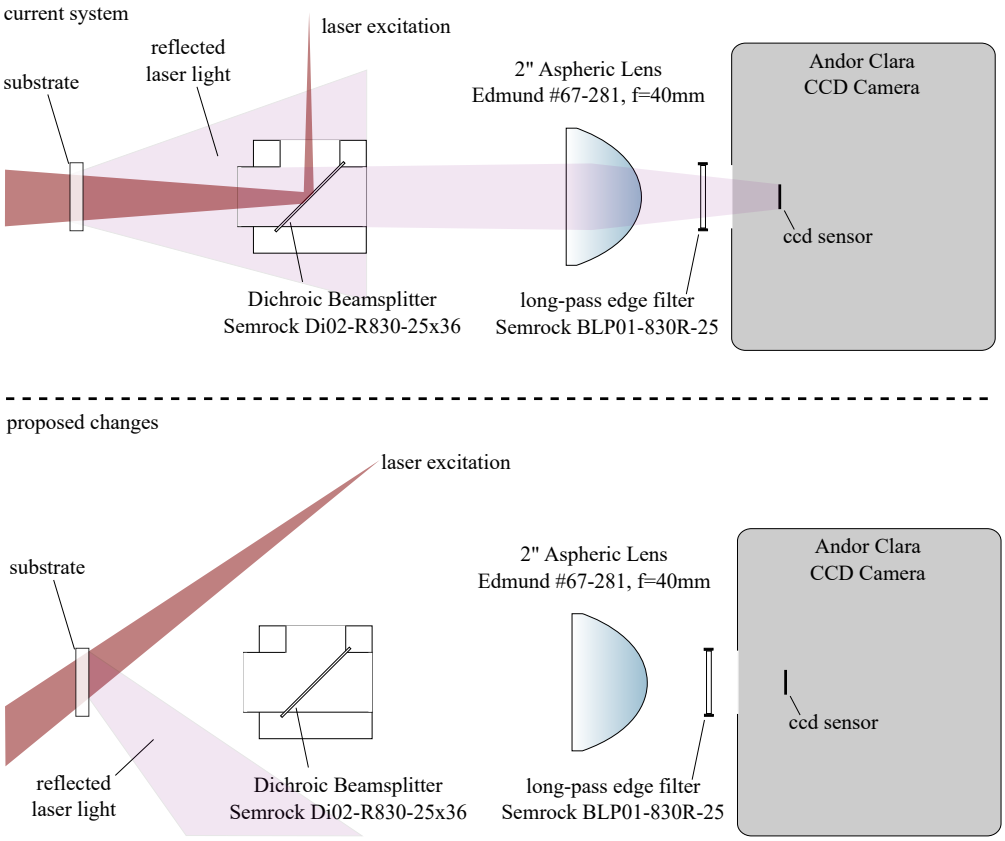

Figure 6.5: Proposed changes to the pSAM imaging system designed to drastically reduce the background rate.

sapphire substrate induced by laser excitation, but there are no known absorption lines for sapphire in this wavelength region.

Assuming the background rate is due to insufficient attenuation of the excitation light, some simple changes to the imaging system would reduce the background by the desired amount. The addition of a second filter upstream of the CCD, with the appropriate optical properties, could alone provide the requisite attenuation by a factor of 10^3. A possibly more effective adjustment is to change the geometry of the imaging system such that the excitation light is no longer aligned along the imaging axis. Such a change would prevent reflected laser light from reaching the CCD sensor. The current imaging system and a possible modification is presented in Figure 6.5. The improvements in integration time for single-atom detection are summarized in Table 6.1.

Table 6.1: List of techniques for reducing the required integration time t for single-atom detection.

Parameter	Reduction in t	Technique
R_T	10	Imaging lens closer to substrate, increasing ϵ_Ω.
R_T	10^2–10^4	Increase laser intensity I.
η	10^6	Additional optical filter, decreasing R_b.
η	10^6	Adjust laser excitation geometry, decreasing R_b.
η	25	Use CCD with favorable efficiency.

6.3 Future outlook

This dissertation outlines the first exciting steps undertaken in commissioning the single-atom microscope as a novel detection method for measurement of nuclear cross sections with astrophysical importance. Assembly and testing of pSAM has demonstrated the ability to repeatably deposit optically transparent solid noble gas films of requisite thickness to capture energetic heavy ions, a key requirement for this technique. $^{84}\mathrm{Kr}(p,\gamma)^{85}\mathrm{Rb}$ has been selected as an ideal nuclear reaction for commissioning pSAM. Further development of the atomic beam fluorescence method for doping a solid krypton film with a known concentration of rubidium atoms is required to arrive at a more precise measurement of the absorption and fluorescence cross section of matrix-isolated rubidium. Beamline tests performed at the ReA3 facility did not identify any unexpected problems, and showed promising results for the neutralization efficiency of highly-ionized energetic rubidium. Before attempting a cross section nuclear cross section measurement, the sensitivity of optical detection needs to improve by several orders of magnitude, though most of that improvement appears feasible.

APPENDICES

APPENDIX A

ANDOR CLARA CCD CALIBRATION

Calibration of the Andor Clara charge-coupled device (CCD) involves determining the photon-to-count conversion ratio, which is a measure of the number of photons required to register a single count on a pixel of the CCD sensor. The CCD sensor has dimensions of 8.98 x 6.71 mm, subdivided into WxH = 1392 x 1040 (=1447680) pixels, each pixel having dimensions of 6.45 x 6.45 μm. The pixels are semiconductor capacitors which convert incoming photons to electrons which are then read out, amplified, and digitized after a given exposure time. The Clara CCD has pixel readout rates of 20 MHz (14-bit digitization) or 1 MHz (16-bit digitization), allowing for pixels to take a value between 0–$2^{14} - 1 = 16383$ or 0–$2^{16} - 1 = 65535$ counts. All CCDs exhibit a constant baseline signal which is independent of exposure time that should be subtracted from a given image, hereafter referred to as dark counts. For the Clara CCD, the dark count is approximately 500 counts per pixel. The dark counts are a smaller portion of the maximum pixel value when using a 1 MHz pixel readout rate (16-bit), allowing for a more sensitive measurement. The downside is that readout of the image takes significantly longer, roughly 1.5 seconds at 1 MHz readout rate compared to 0.07 seconds at 20 MHz.

The Clara CCD possesses an 'Extended IR Mode' which significantly increases the sensitivity of the sensor to infrared light, though it is only useful for exposure times longer than 10 ms. The efficiency of the Andor Clara CCD camera has been measured for both Normal and Extended IR mode, in the wavelength rage from 700 - 1000 nm using the MSquared SOLSTiS laser. As the output of the laser is fairly high power (4 watts), the power needs to be attenuated significantly to avoid overexposing the sensitive CCD. The infrared output from the SOLSTiS was stepped down in intensity through the use of a 10x beam-expander, whose output was spatially filtered with a 500 μm pinhole. For the Extended IR mode calibration, the power was further attenuated using a glan-laser polarizer (Thorlabs GL10-B), before being steered into a 10x second beam-expander and a 200 μm pinhole to further reduce the intensity and total power. The output of the second beam

pinhole was elevated and steered onto the sensor of the Clara CCD,which is encased in a light-tight box to eliminate background light. This setup is pictured in Figure A.1.

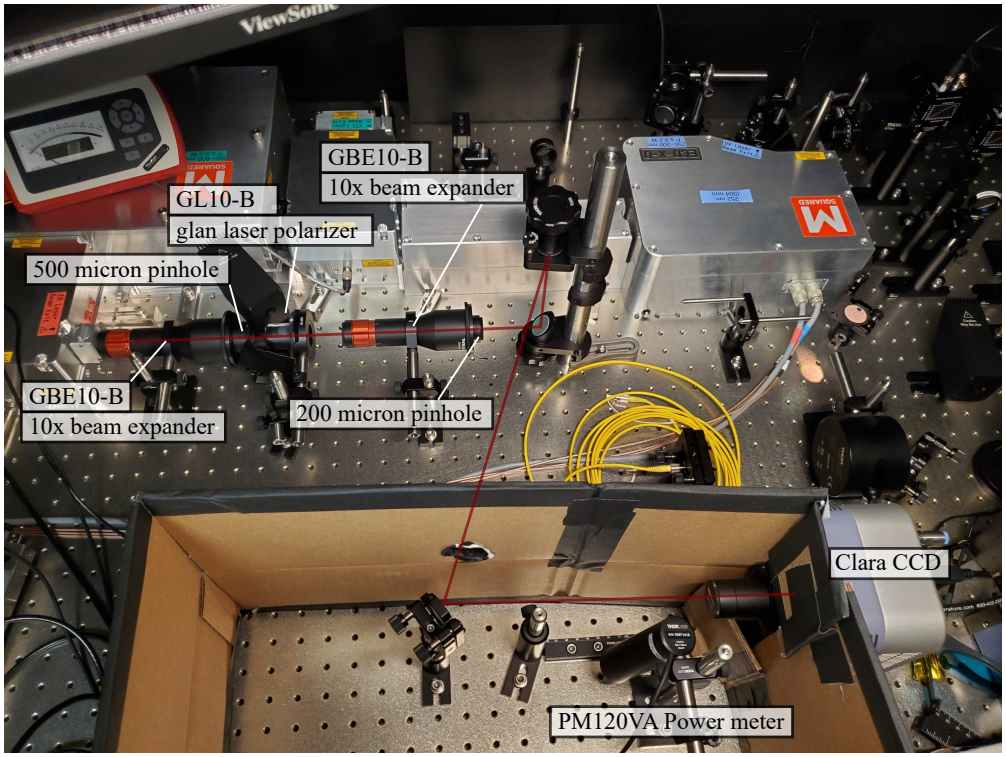

Figure A.1: Experimental setup for the Extended IR Andor Clara CCD calibration.

For this calibration, the SOLSTiS was tuned between 700 and 1000 nm mostly in 10 nm increments (30 total). After tuning to a wavelength, the power immediately before the CCD was measured with a calibrated power-meter (Thorlabs PM120VA), at the position marked T in the diagram above. The power-meter is capable of correcting for its own wavelength dependence, and so the current wavelength was entered into the power-meter before each power measurement. The laser beam profile was well represented by an Airy Disk [74] (pattern resulting from diffraction through the 200 micron pinhole), displayed in Figure A.2.

For each wavelength, the CCD took a kinetic acquisition of 20 frames of the incident beam spot, with an exposure time of 300 milliseconds, and with the PreAmp gain set to 1× in Extended IR mode, and 1 MHz readout rate. For the Normal mode calibration, 100 frames were taken with a 10 ms exposure time and with the PreAmp gain set to 1.5×. Laser power measurements were

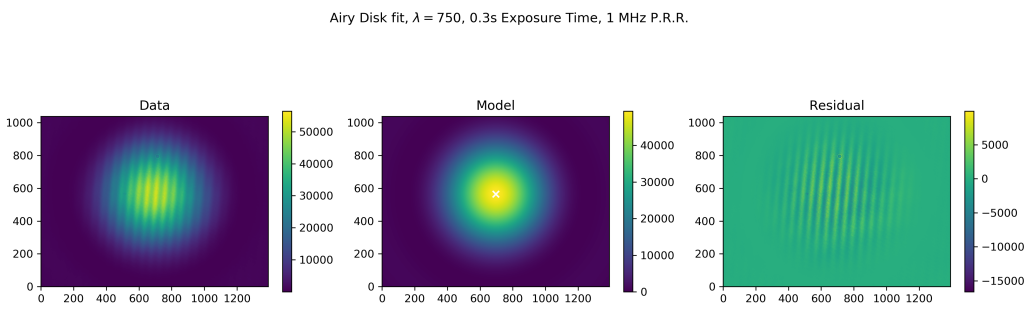

Figure A.2: Sample image from the CCD calibration at 750 nm, with fit to an Airy disk.

recorded before and after each measurement.

The measured laser power was converted to a photon rate via:

$$R_\gamma = P\,\frac{\lambda}{hc}, \tag{A.1}$$

where R_γ is the photon rate in Hz, P is the laser power in Watts, λ is the wavelength in m, $c = 2.9979\times10^8$ m/s is the speed of light in m/s, and $h = 6.626\times10^{-34}$ J $\cdot$ s is the Planck constant. It is assumed that the entire laser beam-spot was captured by the power-meter. I assumed the manufacturers uncertainty for the laser power measurement (3 % for 440–980 nm, 7 % for 981–1100 nm). Uncertainty in wavelength was negligible. The kinetic series images were averaged into a single average frame for the dark, background, and 30 calibration measurements. The averaged dark count frame was subtracted from both the background frame and the 30 calibration measurements. The 30 calibration measurement frames also had the averaged background frame subtracted, though the background was negligible for these measurements. The counts from all pixel were summed to get a total number of counts (N_{CCD}).

The efficiency of the camera is therefore

$$\epsilon = \frac{N_{\mathrm{CCD}}}{R_\gamma\, t_{\mathrm{exp}}}, \tag{A.2}$$

where t_{exp} is the CCD exposure time. The results of both calibrations are plotted in Figure A.3. The measurements are also listed in Table A.1.

Table A.1: CCD count per photon calibration.

Normal Mode, 14-bit, 1.5x Gain			Extended IR Mode, 16-bit, 1x Gain		
λ (nm)	ϵ (counts per photon)	$\delta\epsilon$	λ (nm)	ϵ (counts per photon)	$\delta\epsilon$
			700	0.90057	0.04271
710	0.18912	0.00750	710	0.85368	0.03765
720	0.18047	0.00713	720	0.81893	0.03415
730	0.17047	0.00106	730	0.82407	0.03383
740	0.16341	0.00668	740	0.78049	0.04651
750	0.15075	0.00601	750	0.74270	0.04215
760	0.13794	0.00545	760	0.75887	0.04522
770	0.13160	0.00520	770	0.66040	0.03588
780	0.12013	0.00472	780	0.63982	0.03226
790	0.11419	0.00465	790	0.62149	0.02990
800	0.10354	0.00409	800	0.56824	0.02624
810	0.09550	0.00380	810	0.51806	0.02261
820	0.08595	0.00340	820	0.46627	0.02015
830	0.07997	0.00319	830	0.46274	0.01930
839	0.07073	0.00278	839	0.40600	0.01382
850	0.06426	0.00254	850	0.36791	0.01405
860	0.05746	0.00226	860	0.33689	0.01259
870	0.05305	0.00209	870	0.31951	0.01176
880	0.04494	0.00179	878	0.27128	0.01184
890	0.03977	0.00157	890	0.24170	0.00837
900	0.03340	0.00133	900	0.20927	0.00704
910	0.03094	0.00124	910	0.19001	0.00631
920	0.02796	0.00111	920	0.17135	0.00565
930	0.02347	0.00094	930	0.14439	0.00515
940	0.01944	0.00078	940	0.12098	0.00418
950	0.01708	0.00068	950	0.10405	0.00334
960	0.01385	0.00055	960	0.08817	0.00291
970	0.01165	0.00046	970	0.07186	0.00241
980	0.00930	0.00037	980	0.06017	0.00208
990	0.00755	0.00056	990	0.04748	0.00336
999	0.00627	0.00047	996	0.04082	0.00290

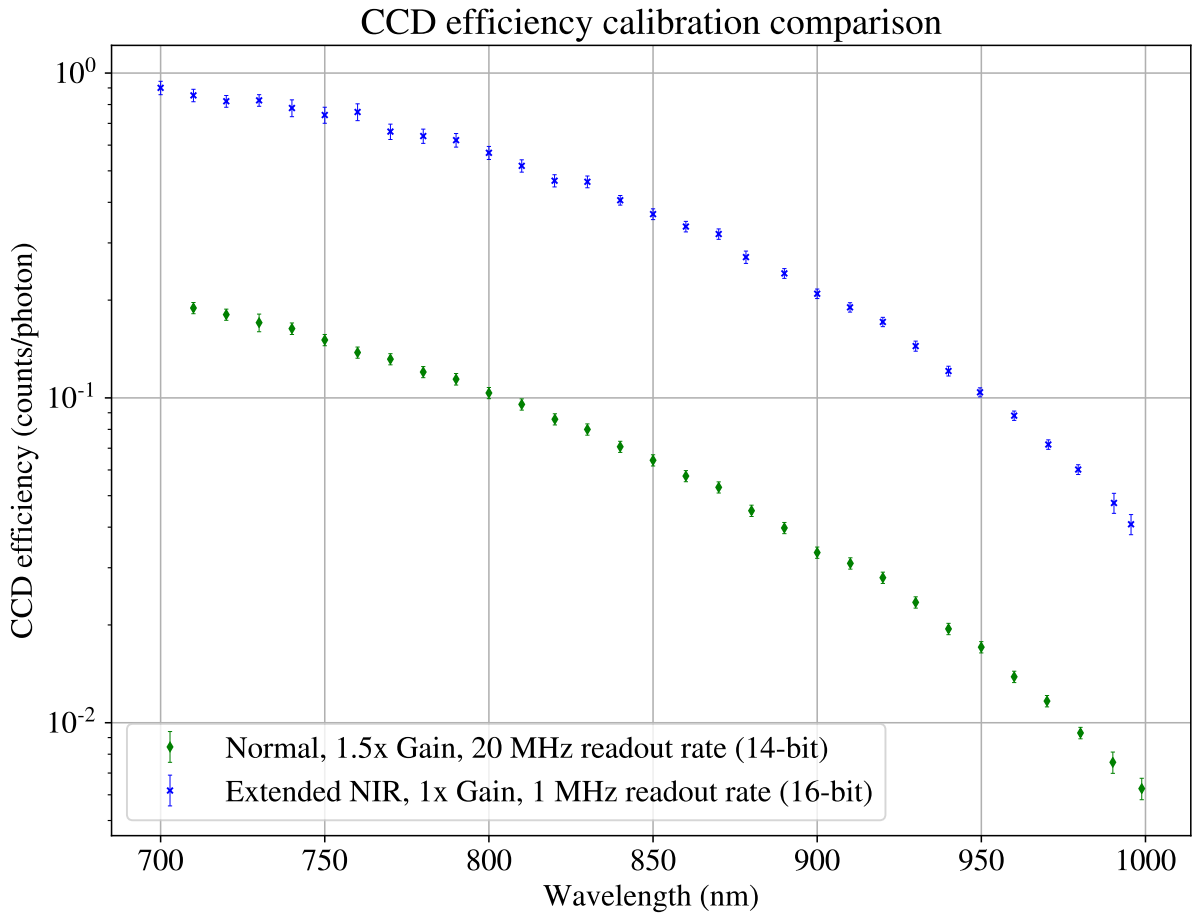

Figure A.3: Measured counts per photon as a function of wavelength for different Clara CCD settings.

APPENDIX B

PULSE TUBE CRYOCOOLERS

The working principle of most closed-cycle cryorefrigeration systems is similar to the Stirling cycle. A working gas (typically helium) is compressed at room temperature, where the heat of compression is removed, and subsequently expands and cools near a cold heat exchanger where heat is extracted from whatever is being cooled. Figure B.1 graphically describes the ideal Stirling cooling cycle, which can be divided into four basic steps:

1. **Compression:** The cold piston begins the cycle close to the low temperature heat exchanger. The warm piston compresses the gas isothermally, and the heat of compression is expelled to the external environment through the high temperature heat exchanger at ambient temperature.

2. **Transfer:** Both pistons move together to isochorically (with constant volume) transfer the room temperature compressed gas through the regenerator, cooling the gas to the low temperature by depositing heat in the regenerator.

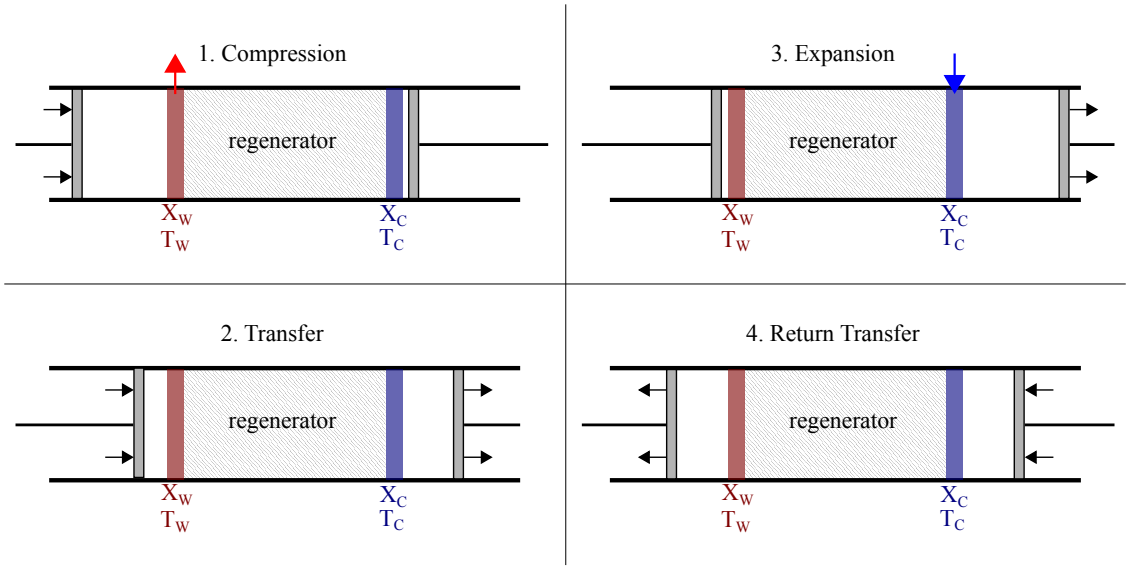

Figure B.1: Diagram of the Stirling Cycle. Arrows indicate piston motion and heat exchanger energy flow.

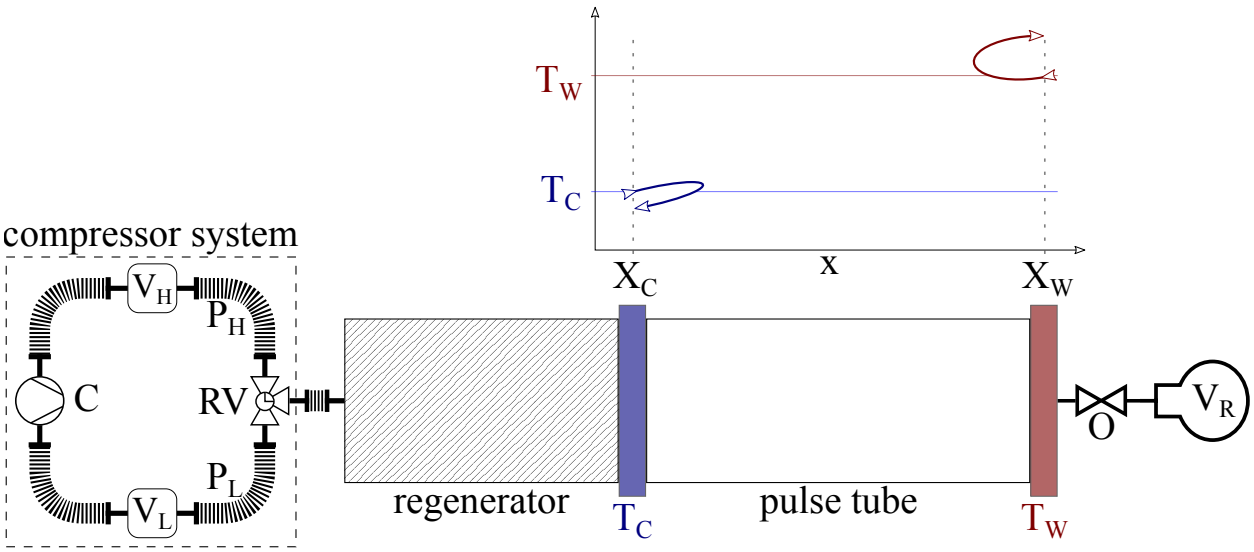

Figure B.2: Basic pulse tube cryorefrigerator with an external compressor system. The graph illustrates the temperature behavior of gas passing through the heat exchangers at either end of the pulse tube during one pressure cycle.

3. **Expansion:** The cold piston is retracted to expand the gas in the cold volume, cooling the gas and absorbing heat from the low temperature heat exchanger. This step removes heat from any sample mounted to the low temperature heat exchanger.

4. **Return Transfer:** Both pistons again move together to isochorically transfer the cold gas through the regenerator, where it reabsorbs the heat deposited during step 2. After this step, the system has returned to its original configuration.

The cryocooler in pSAM is of the Gifford-McMahon (GM) pulse tube variety [75], which has an orifice and a reservoir volume instead of the cold piston as in the basic Stirling system. A schematic of a single GM pulse tube cooling system is displayed in Figure B.2. An external compressor (C) provides ambient temperature (T_W) compressed helium at two pressures (P_H, P_L) which a motorized rotating valve (RV) alternates between, creating an oscillating pressure in the regenerator and pulse tube. As the pressure rises to P_H, the working gas cools by depositing heat in the regenerator before flowing through the cold heat exchanger (X_C) and entering the pulse tube at T_C and P_H. When the valve (RV) switches to low pressure (P_L), the gas in the pulse tube expands, cools, and flows back through X_C at $T<T_C$, extracting energy from the sample being cooled.

The reverse process occurs at the warm heat exchanger (X_W), which is connected to a reservoir volume (V_R) by an orifice (O). The orifice is a valve used to regulate flow into and out of V_R. At the high pressure part of the cycle, gas at the warm end of the pulse tube compresses, heats, and flows into V_R through the warm heat exchanger (X_W) at T_W, where it deposits the heat energy due to compression. When pressure in the tube subsequently drops, gas at temperature T_W flows from the reservoir into the pulse tube until equilibrium is achieved. The flow of gas into and out of V_R is crucial to efficient cooling, as without flow, the cooling due to expansion in the tube would be canceled by the subsequent compression.

The purpose of the pulse tube is to isolate the two processes occurring at the heat exchangers. Gas in the middle of the pulse tube never leaves the tube since the flow is reversed before it can traverse the entire length of the tube. The purpose of the regenerator is to pre-cool the gas entering the pulse tube and reheat the gas exiting the pulse tube. The regenerator usually consists of a high heat capacity material with large surface area to maximize heat exchange with the gas. The lack of moving parts near the cold heat exchanger makes pulse tube cryocoolers highly reliable, have long lifetimes, and results in greatly reduced vibration at the cold heat exchanger. Low vibration

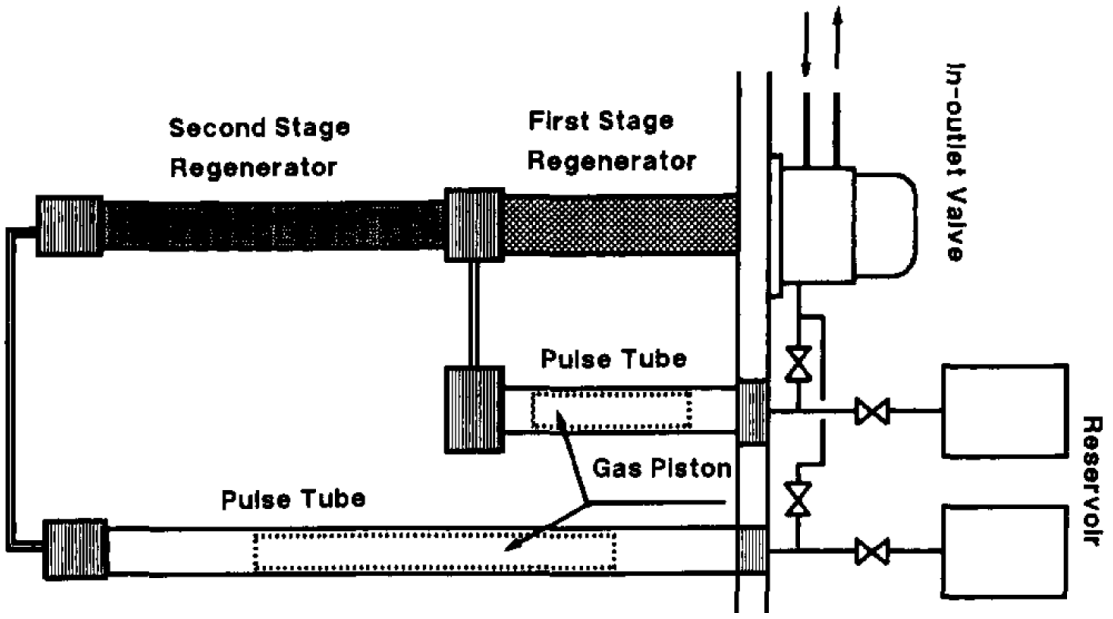

Figure B.3: Standard configuration for modern two-stage pulse tube cryocoolers. Figure taken from [3].

is especially important for optical applications, where sample stability is crucial. For the pSAM cryocooler system, the compressor is connected to the motorized rotating valve by two 100 ft. long flexible helium lines, which serve as the high and low pressure volumes in the compressor system. The motorized valve is isolated from the cold head (regenerator and pulse tubes) by a 2 ft. flexible helium line.

Contemporary single-stage pulse tube cryocoolers can achieve base temperatures near 30 K, where they are limited by heat conduction along the regenerator. To reach the single-digit base temperatures necessary to freeze Neon, pSAM uses a more advanced two-stage pulse tube cryocooler. In this configuration the regenerators are in series and the pulse tubes are in parallel, as displayed in Figure B.3 from [3]. The second stage heat exchanger for the pSAM cryocooler is capable of achieving a base temperature of 2.8 K under no heat load. A drawing and picture of the pSAM cold head are included in Figure B.4 and B.5. A more thorough description of modern cryocooler design and development can be found in [76, 77, 3, 78].

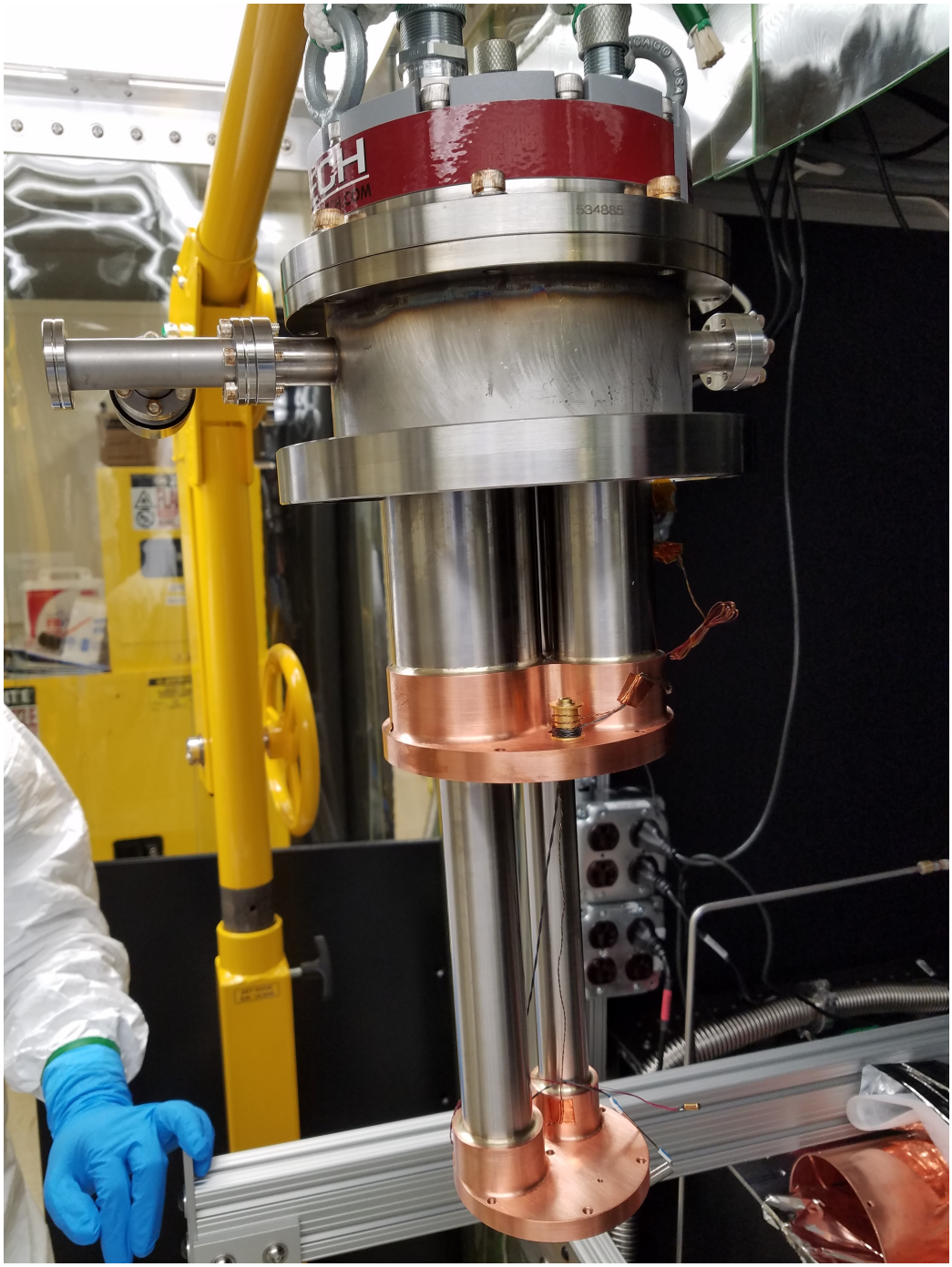

Figure B.4: Picture of the pSAM cryocooler cold head. External reservoir volumes not pictured.

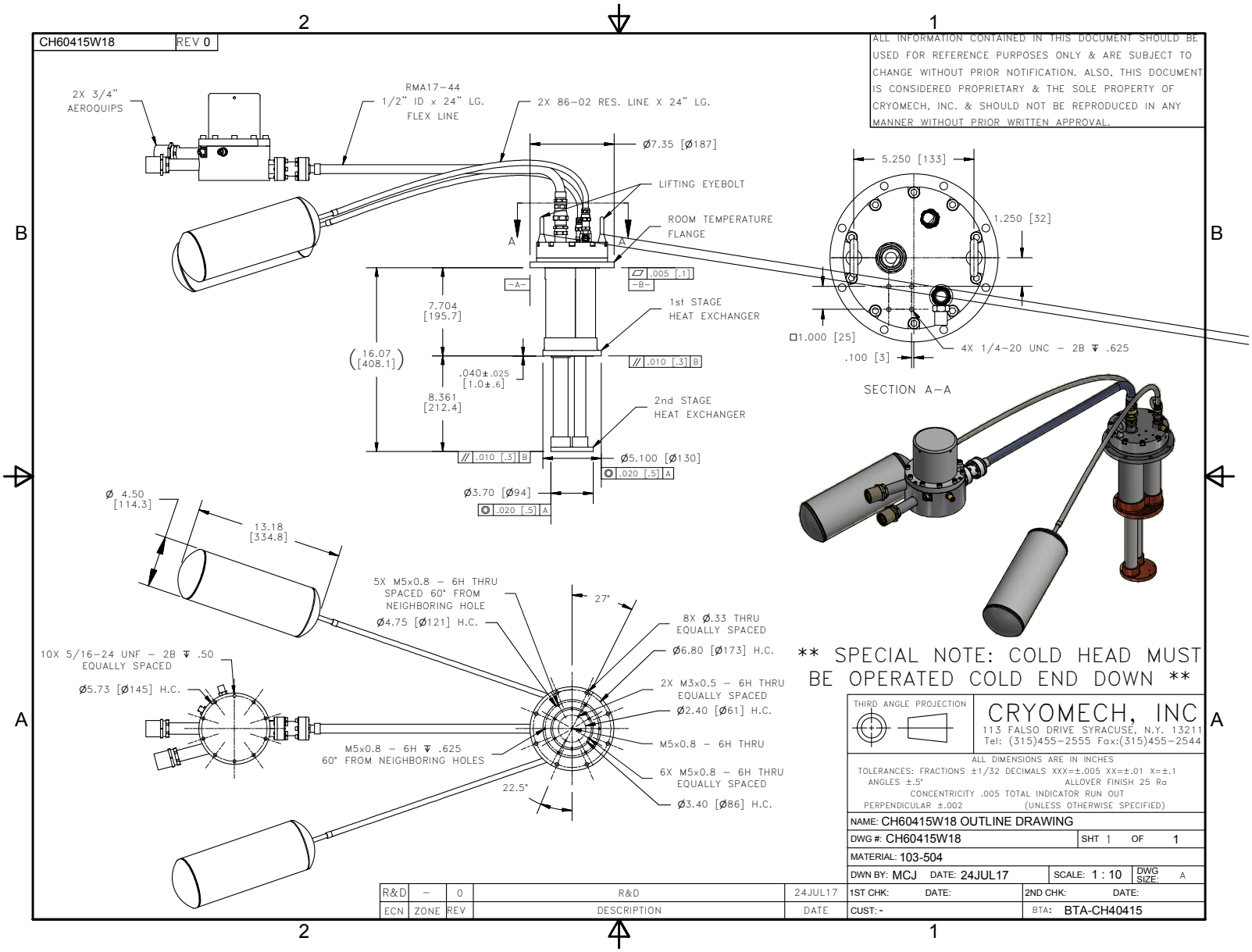

Figure B.5: Dimensioned drawing of the pSAM cryocooler (Cryomech model PT415), with remote motor.

APPENDIX C

TEMPERATURE PROBE CALIBRATIONS

Table C.1: pSAM Temperature Sensor Calibration Data.

	Lakeshore Sensor Model CX-1050-AA-1.4L		Lakeshore Sensor Model CX-1050-CU-HT-1.4L	
	Serial Number X103297		Serial Number X134596	
index	Temperature (K)	Resistance (Ω)	Temperature (K)	Resistance (Ω)
1	1.20012	39214.8	1.19951	38225.6
2	1.30145	31724.5	1.29965	30841.4
3	1.39992	26474.8	1.39971	25538.2
4	1.60176	19376.0	1.59972	18609.2
5	1.80418	15067.7	1.80009	14413.5
6	2.00010	12310.3	1.99643	11712.5
7	2.20037	10330.4	2.20165	9746.46
8	2.40088	8876.43	2.40150	8352.72
9	2.59947	7783.34	2.59873	7312.47
10	2.80034	6919.27	2.79697	6493.96
11	3.00021	6233.21	2.99541	5841.74
12	3.20060	5674.01	3.19814	5300.68
13	3.40246	5207.05	3.39656	4863.22
14	3.60085	4821.02	3.59962	4487.47
15	3.80121	4488.85	3.79974	4172.93
16	3.99340	4213.27	3.99612	3907.02
17	4.18279	3975.40	4.20270	3663.44
18	4.53376	3608.25	4.58971	3288.94
19	4.94429	3261.71	4.99923	2973.78
20	5.45870	2921.39	5.51191	2663.31
21	6.18086	2562.03	6.23500	2334.03
22	7.00112	2261.00	7.05740	2058.36
23	8.03154	1984.02	8.08655	1804.01
24	9.06155	1777.80	9.12550	1613.42
25	10.0914	1617.55	10.1586	1466.64
26	11.1203	1488.99	11.1913	1348.73
27	12.1410	1383.92	12.2129	1252.61
28	13.1516	1296.28	13.2269	1172.19
29	14.1546	1221.57	14.2252	1104.24
30	15.1524	1156.88	15.2154	1045.55
31	16.1370	1100.58	16.1977	994.256
32	17.1190	1050.55	17.1724	948.751
33	18.0978	1005.68	18.1427	908.072
34	19.0774	964.979	19.1070	871.505
35	20.0548	928.012	20.0794	837.787
36	21.1348	890.724	21.1446	804.163
37	22.7142	841.941	22.7274	759.469
38	24.3140	798.211	24.3316	719.454
39	25.9307	758.833	25.9412	683.751
40	27.5459	723.521	27.5634	651.468
41	29.1683	691.450	29.1927	622.167
42	30.9802	659.093	31.0123	592.643

Table C.2: pSAM Temperature Sensor Calibration Data.

	Lakeshore Sensor Model CX-1050-AA-1.4L		Lakeshore Sensor Model CX-1050-CU-HT-1.4L	
	Serial Number X103297		Serial Number X134596	
Index	Temperature (K)	Resistance (Ω)	Temperature (K)	Resistance (Ω)
43	33.0928	625.198	33.1275	561.912
44	36.0913	582.963	36.1363	523.563
45	39.0904	546.380	39.1473	490.353
46	42.0924	514.284	42.1561	461.428
47	45.0860	485.984	45.1528	435.888
48	48.0842	460.756	48.1527	413.159
49	50.0821	445.368	50.1462	399.419
50	55.0777	411.227	55.1320	368.824
51	60.0722	382.106	60.1248	342.742
52	65.0623	356.965	65.1148	320.212
53	70.0568	334.978	70.1060	300.580
54	75.0535	315.549	75.0924	283.259
55	80.0447	298.320	80.0806	267.876
56	85.0496	282.826	85.0833	254.075
57	90.0475	268.881	90.0775	241.622
58	95.0448	256.231	95.0758	230.358
59	100.044	244.702	100.072	220.100
60	110.039	224.459	110.059	202.063
61	120.035	207.222	120.057	186.701
62	130.038	192.360	130.062	173.486
63	140.039	179.429	140.061	161.979
64	150.036	168.074	150.056	151.893
65	160.030	158.021	160.052	142.949
66	170.023	149.085	170.048	134.984
67	180.016	141.076	180.038	127.854
68	190.023	133.852	190.043	121.422
69	200.026	127.329	200.048	115.603
70	210.027	121.415	210.047	110.319
71	220.020	116.019	220.036	105.507
72	230.024	111.086	230.044	101.105
73	240.031	106.568	240.042	97.0637
74	250.022	102.415	250.032	93.3474
75	260.034	98.5810	260.045	89.9072
76	270.032	95.0404	270.039	86.7346
77	280.043	91.7438	280.046	83.7939
78	290.035	88.6792	290.040	81.0603
79	300.052	85.8434	300.040	78.5092
80	310.038	83.2023	310.015	76.1460
81	315.049	81.9444	315.024	75.0136
82	320.057	80.7260	320.024	73.9221
83	326.058	79.3161	326.012	72.6612
84	330.073	78.4051	330.021	71.8414

APPENDIX D

LINEAR SHIFT MECHANISM (LSM) COMMANDS

Table D.1: Commonly used LSM commands. Refer to McLennan PM1000 Motion Controller manual for more information. The '1' beginning each command refers to the axis of motion, of which there is only one in the case of pSAM, but could be higher if multiple linear motion mechanisms are ever implemented.

Command	Description
1qa	Query all. Returns all of the current settings and modes of the controller along with the current positions in a single page format.
1qs	Query speeds. Query the current settings for the speeds and accelerations.
1qp	Query position. Query the current position information. Returns values for Command Position (CP, steps), Actual Position (AP, μm), Input Position (IP), Auxiliary Position (TP), and Datum Position (OD, steps). CP is the stepper motor position, and AP is the position read by the linear encoder. IP, TP, are reserved for additional linear encoders and are not used. OD is a reference position and is not used.
1ma<position>	Move absolute. Move the motor to the position given inthe argument. The position is relative to the Command Position of zero.
1mr<position>	Move relative. Move the motor to the position given in the argument relative to the current Command Position.
1sv<speed>	Set velocity. Sets the Slew (maximum) velocity for all following moves (steps/second, range from 1 to 1,200,000. 15,000 typical.)
1ab	Command abort. Sending will abort the current motion. Motion control will be disabled after command abort until reset with the RS command.
1rs	Command Reset. Resets an abort condition, enabling motion control.

BIBLIOGRAPHY

BIBLIOGRAPHY

[1] Jack Ekin. *Experimental Techniques for Low-Temperature Measurements*. Oxford University Press, oct 2006.

[2] D A Steck. Rubidium 85 and 87 D Line Data, available online at http://steck.us/alkalidata (revision 2.1.5, 13 January 2015). pages 1–29, 2015.

[3] Y. Matsubara and J. L. Gao. Novel configuration of three-stage pulse tube refrigerator for temperatures below 4 K. *Cryogenics*, 34(4):259–262, apr 1994.

[4] E. Margaret Burbidge, G. R. Burbidge, William A. Fowler, and F. Hoyle. Synthesis of the elements in stars. *Reviews of Modern Physics*, 29(4):547–650, oct 1957.

[5] Bradley S. Meyer. The r-, s-, and p-Processes in Nucleosynthesis. *Annual Review of Astronomy and Astrophysics*, 32(1):153–190, sep 1994.

[6] T Rauscher, N Dauphas, I Dillmann, C Fröhlich, Zs Fülöp, and Gy Gyürky. Constraining the astrophysical origin of the p-nuclei through nuclear physics and meteoritic data. *Reports on Progress in Physics*, 76(6):066201, jun 2013.

[7] F.-K. Thielemann, M. Eichler, I.V. Panov, and B. Wehmeyer. Neutron Star Mergers and Nucleosynthesis of Heavy Elements. *Annual Review of Nuclear and Particle Science*, 67(1):annurev–nucl–101916–123246, oct 2017.

[8] M. Couder, G. P.A. Berg, J. Görres, P. J. LeBlanc, L. O. Lamm, E. Stech, M. Wiescher, and J. Hinnefeld. Design of the recoil mass separator St. George. *Nuclear Instruments and Methods in Physics Research, Section A: Accelerators, Spectrometers, Detectors and Associated Equipment*, 587(1):35–45, mar 2008.

[9] G. P.A. Berg, M. Couder, M. T. Moran, K. Smith, M. Wiescher, H. Schatz, U. Hager, C. Wrede, F. Montes, G. Perdikakis, X. Wu, A. Zeller, M. S. Smith, D. W. Bardayan, K. A. Chipps, S. D. Pain, J. Blackmon, U. Greife, K. E. Rehm, and R. V.F. Janssens. Design of SECAR a recoil mass separator for astrophysical capture reactions with radioactive beams. *Nuclear Instruments and Methods in Physics Research, Section A: Accelerators, Spectrometers, Detectors and Associated Equipment*, 877(March 2017):87–103, 2018.

[10] M. Jaeger, R. Kunz, A. Mayer, J. W. Hammer, G. Staudt, K. L. Kratz, and B. Pfeiffer. 22Ne(a,n)25Mg: The Key Neutron Source in Massive Stars. *Physical Review Letters*, 87(20):202501, oct 2001.

[11] Daniel Robertson, Manoel Couder, Uwe Greife, Frank Strieder, and Michael Wiescher. Underground nuclear astrophysics studies with CASPAR. *European Physical Journal Web of Conferences*, 109(09002):09002, feb 2016.

[12] A. Formicola, C. G. Bruno, A. Caciolli, F. Cavanna, R. Depalo, A. Di Leva, D. A. Scott, D. Trezzi, M. Aliotta, M. Anders, D. Bemmerer, C. Broggini, P. Corvisiero, Z. Elekes, Zs. Fülöp, G. Gervino, A. Guglielmetti, C. Gustavino, Gy. Gyürky, G. Imbriani, M. Junker, R. Menegazzo, P. Prati, E. Somorjai, O. Straniero, F. Strieder, and T. Szücs. Cross-section measurements at astrophysically relevant energies: The LUNA experiment. *Nuclear Instruments and Methods in Physics Research, Section A: Accelerators, Spectrometers, Detectors and Associated Equipment*, 742:258–260, apr 2014.

[13] F. W. D. Rost. *Fluorescence microscopy*. Cambridge University Press, 1992.

[14] C. Chambers, T. Walton, D. Fairbank, A. Craycraft, D. R. Yahne, J. Todd, A. Iverson, W. Fairbank, A. Alamare, J. B. Albert, G. Anton, I. J. Arnquist, I. Badhrees, P. S. Barbeau, D. Beck, V. Belov, T. Bhatta, F. Bourque, J. P. Brodsky, E. Brown, T. Brunner, A. Burenkov, G. F. Cao, L. Cao, W. R. Cen, S. A. Charlebois, M. Chiu, B. Cleveland, M. Coon, W. Cree, M. Côté, J. Dalmasson, T. Daniels, L. Darroch, S. J. Daugherty, J. Daughhetee, S. Delaquis, A. Der Mesrobian-Kabakian, R. DeVoe, J. Dilling, Y. Y. Ding, M. J. Dolinski, A. Dragone, J. Echevers, L. Fabris, J. Farine, S. Feyzbakhsh, R. Fontaine, D. Fudenberg, G. Giacomini, R. Gornea, G. Gratta, E. V. Hansen, M. Heffner, E. W. Hoppe, J. Hößl, A. House, P. Hufschmidt, M. Hughes, Y. Ito, A. Jamil, C. Jessiman, M. J. Jewell, X. S. Jiang, A. Karelin, L. J. Kaufman, D. Kodroff, T. Koffas, S. Kravitz, R. Krücken, A. Kuchenkov, K. S. Kumar, Y. Lan, A. Larson, D. S. Leonard, G. Li, S. Li, Z. Li, C. Licciardi, Y. H. Lin, P. Lv, R. MacLellan, T. Michel, B. Mong, D. C. Moore, K. Murray, R. J. Newby, Z. Ning, O. Njoya, F. Nolet, O. Nusair, K. Odgers, A. Odian, M. Oriunno, J. L. Orrell, G. S. Ortega, I. Ostrovskiy, C. T. Overman, S. Parent, A. Piepke, A. Pocar, J. F. Pratte, D. Qiu, V. Radeka, E. Raguzin, T. Rao, S. Rescia, F. Retière, A. Robinson, T. Rossignol, P. C. Rowson, N. Roy, R. Saldanha, S. Sangiorgio, S. Schmidt, J. Schneider, A. Schubert, D. Sinclair, K. Skarpaas VIII, A. K. Soma, G. St-Hilaire, V. Stekhanov, T. Stiegler, X. L. Sun, M. Tarka, T. Tolba, T. I. Totev. R. Tsang, T. Tsang, F. Vachon, B. Veenstra, V. Veeraraghavan, G. Visser, J. L. Vuilleumier, M. Wagenpfeil, Q. Wang, J. Watkins, M. Weber, W. Wei, L. J. Wen, U. Wichoski, G. Wrede, S. X. Wu, W. H. Wu, Q. Xia, L. Yang, Y. R. Yen, O. Zeldovich, X. Zhang, J. Zhao, Y. Zhou, and T. Ziegler. Imaging individual barium atoms in solid xenon for barium tagging in nEXO. jun 2018.

[15] M. K. Moe. Detection of neutrinoless double-beta decay. *Physical Review C*, 44(3):R931–R934, sep 1991.

[16] M. Wiescher, F. Käppeler, and K. Langanke. Critical Reactions in Contemporary Nuclear Astrophysics. *Annual Review of Astronomy and Astrophysics*, 50(1):165–210, 2012.

[17] K. A. Chipps, U. Greife, D. W. Bardayan, J. C. Blackmon, A. Kontos, L. E. Linhardt, M. Matos, S. D. Pain, S. T. Pittman, A. Sachs, H. Schatz, K. T. Schmitt, M. S. Smith, and P. Thompson. The Jet Experiments in Nuclear Structure and Astrophysics (JENSA) gas jet target. *Nuclear Instruments and Methods in Physics Research, Section A: Accelerators, Spectrometers, Detectors and Associated Equipment*, 763:553–564, 2014.

[18] T. Rauscher, N. Nishimura, R. Hirschi, G. Cescutti, A. St. J. Murphy, and A. Heger. Uncertainties in the production of p nuclei in massive stars obtained from Monte Carlo variations. *Monthly Notices of the Royal Astronomical Society*, 463(4):4153–4166, dec 2016.

[19] T. Rauscher. NON-SMOKER, https://nucastro.org/nonsmoker.html.

[20] James F. Ziegler, M. D. Ziegler, and J. P. Biersack. SRIM - The stopping and range of ions in matter (2010). *Nuclear Instruments and Methods in Physics Research, Section B: Beam Interactions with Materials and Atoms*, 268(11-12):1818–1823, jun 2010.

[21] Ilja Gerhardt, Kyungseob Sin, and Takamasa Momose. Excitation and emission spectra of rubidium in rare-gas thin-films. *Journal of Chemical Physics*, 137(1):014507, jul 2012.

[22] C. Crépin-Gilbert and A. Tramer. Photophysics of metal atoms in rare-gas complexes, clusters and matrices. *International Reviews in Physical Chemistry*, 18(4):485–556, oct 1999.

[23] Ed. John R. Rumble. *CRC Handbook of Chemistry and Physics, 99th Edition (Internet Version 2018)*. CRC Press/Taylor \& Francis, 2018.

[24] M L Klein and J A Venables. *Rare gas solids*. Number v. 2 in Rare Gas Solids. Academic Press, 1977.

[25] Gerald L. Pollack. The solid state of rare gases. *Reviews of Modern Physics*, 36(3):748–791, jul 1964.

[26] Hamza Shakeel, Haoyan Wei, and J. M. JM Pomeroy. Measurements of enthalpy of sublimation of Ne, N2, O2, Ar, CO2, Kr, Xe, and H2O using a double paddle oscillator. *Journal of Chemical Thermodynamics*, 118:127–138, mar 2018.

[27] Jørgen Schou. Sputtering of frozen gases. *Nuclear Inst. and Methods in Physics Research, B*, 27(1):188–200, jun 1987.

[28] Wilfried Schulze and Dieter M. Kolb. Density and refractive index of solid layers of noble gases and sulphur hexafluoride. *Journal of the Chemical Society, Faraday Transactions 2: Molecular and Chemical Physics*, 70(0):1098–1105, jan 1974.

[29] W. L. Brown and R. E. Johnson. Sputtering of ices: a review. *Nuclear Inst. and Methods in Physics Research, B*, 13(1-3):295–303, 1986.

[30] J. Schou, O. Ellegaard, R. Pedrys, and H. Sørensen. Sputtering of solid neon and argon by medium mass ions. *Nuclear Inst. and Methods in Physics Research, B*, 65(1-4):173–176, mar 1992.

[31] V. Balaji, D. E. David, T. F. Magnera, J. Michl, and H. M. Urbassek. Sputtering yields of condensed rare gases. *Nuclear Inst. and Methods in Physics Research, B*, 46(1-4):435–440, feb 1990.

[32] Derek C. Silverman and Mario E. Fajardo. Matrix isolation spectroscopy of Na atoms deposited as Na+ions. *Journal of Chemical Physics*, 106(22):8964–8966, 1997.

[33] B. Mong, S. Cook, T. Walton, C. Chambers, A. Craycraft, C. Benitez-Medina, K. Hall, W. Fairbank, J. B. Albert, D. J. Auty, P. S. Barbeau, V. Basque, D. Beck, M. Breidenbach, T. Brunner, G. F. Cao, B. Cleveland, M. Coon, T. Daniels, S. J. Daugherty, R. DeVoe, T. Didberidze, J. Dilling, M. J. Dolinski, M. Dunford, L. Fabris, J. Farine, W. Feldmeier, P. Fierlinger, D. Fudenberg, G. Giroux, R. Gornea, K. Graham, G. Gratta, M. Heffner, M. Hughes, X. S. Jiang, T. N. Johnson, S. Johnston, A. Karelin, L. J. Kaufman, R. Killick, T. Koffas, S. Kravitz, R. Krücken, A. Kuchenkov, K. S. Kumar, D. S. Leonard, C. Licciardi, Y. H. Lin, J. Ling, R. MacLellan, M. G. Marino, D. Moore, A. Odian, I. Ostrovskiy, A. Piepke, A. Pocar, F. Retiere, P. C. Rowson, M. P. Rozo, A. Schubert, D. Sinclair, E. Smith, V. Stekhanov, M. Tarka, T. Tolba, K. Twelker, J.-L. Vuilleumier, J. Walton, M. Weber, L. J. Wen, U. Wichoski, L. Yang, Y.-R. Yen, and Y. B. Zhao. Spectroscopy of Ba and Ba + deposits in solid xenon for barium tagging in nEXO. *Physical Review A*, 91(2):022505, feb 2015.

[34] H.D. Betz. Charge States and Chatge-Changing Cross Sections of Fast Heavy Ions Penetrating Through Gaseous and Solid Media. *Reviews of Modern Physics*, 44(8):75, 1972.

[35] J. J. Wright and L. C. Balling. Absorption and emission spectra of Li atoms trapped in rare gas matrices. *The Journal of Chemical Physics*, 73(7):3103–3106, oct 1980.

[36] L. C. Balling, M. D. Havey, and J. F. Dawson. Absorption and emission spectra of Na atoms trapped in rare-gas matrices. *The Journal of Chemical Physics*, 69(4):1670–1675, 1978.

[37] L. C. Balling, M. D. Havey, and J. J. Wright. Absorption and emission spectra of K atoms trapped in rare-gas matrices. *The Journal of Chemical Physics*, 70(5):2404–2408, mar 1979.

[38] L. C. Balling and J. J. Wright. Laser excitation of excited states of Rb and Cs atoms in an Ar matrix. *The Journal of Chemical Physics*, 78(1):592–593, jan 1983.

[39] J.M. Brom, W. D. Hewett Jr., and W. Weltner Jr. Optical spectra of Be atoms and Be2 molecules in rare gas matrices. *The Journal of Chemical Physics*, 62(8):3122, apr 1975.

[40] Brendan Healy, Paul Kerins, and John G. McCaffrey. Metal atom (Zn, Cd and Mg) luminescence in solid neon. *Low Temperature Physics*, 38(8):679–687, aug 2012.

[41] John G. McCaffrey and Geoffrey A. Ozin. Luminescence of atomic magnesium in inert low temperature solids. I. Argon and krypton. *The Journal of Chemical Physics*, 101(12):10354–10365, 1994.

[42] V. E. Bondybey. Multiphonon relaxation processes in matrix isolated atoms. *The Journal of Chemical Physics*, 68(3):1308–1309, feb 1978.

[43] John C. Miller and Lester Andrews. Laser excited emission spectra of Sr2isolated in rare gas matrices at 12 K, jul 1978.

[44] Veronica A. Bracken, Peter Gürtler, and John G. McCaffrey. Luminescence spectroscopy of atomic zinc in rare-gas solids. I. *Journal of Chemical Physics*, 107(14):5290–5299, aug 1997.

[45] Sandra L. Laursen and Harry E. Cartland. Multiplicity dependence of matrix-induced frequency shifts for atomic transitions of the group 12 metals in rare gas solids. *The Journal of Chemical Physics*, 95(7):4751–4755, oct 1991.

[46] J. H. Ammeter and D. C. Schlosnagle. Electronic quenching of Al and Ga atoms isolated in rare gas matrices. *The Journal of Chemical Physics*, 59(9):4784–4820, nov 1973.

[47] Roger Grinter and Richard J. Singer. MCD spectroscopy and magnetization studies of matrix-isolated aluminium atoms. *Chemical Physics*, 113(1):87–97, apr 1987.

[48] Leonid Khriachtchev, Mika Pettersson, Esa Isoniemi, and Markku Rasanen. 193 nm photolysis of H2S in rare-gas matrices: Luminescence spectroscopy of the products. *Journal of Chemical Physics*, 108(14):5747–5754, jul 1998.

[49] M. J. Pellin, D. M. Gruen, T. Fisher, and T. Foosnaes. Emission, optical–optical double resonance, and excited state absorption spectroscopy of matrix isolated chromium and molybdenum atoms. *The Journal of Chemical Physics*, 79(12):5871–5886, dec 1983.

[50] Chen-Yu Xu. *Studies of neutral ytterbium atoms in a solid neon matrix*. PhD thesis, 2015.

[51] C. Y. Xu, J. Singh, J. C. Zappala, K. G. Bailey, M. R. Dietrich, J. P. Greene, W. Jiang, N. D. Lemke, Z. T. Lu, P. Mueller, and T. P. O'Connor. Measurement of the hyperfine quenching rate of the clock transition in Yb 171. *Physical Review Letters*, 113(3):1–5, 2014.

[52] C. Y. Xu, S. M. Hu, J. Singh, K. Bailey, Z. T. Lu, P. Mueller, T. P. O'Connor, and U. Welp. Optical excitation and decay dynamics of ytterbium atoms embedded in a solid neon matrix. *Physical Review Letters*, 107(9):093001, aug 2011.

[53] W W Duley. The spectroscopy of metal atoms trapped in low-temperature matrices of the inert gases: mercury. *Proceedings of the Physical Society*, 90(1):263–268, jan 1967.

[54] Hiroyuki Niino, Tadatake Sato, and Akira Yabe. Laser ablation of solid nitrogen films at a cryogenic temperature. volume 4274, pages 232–239. International Society for Optics and Photonics, jun 2001.

[55] A. C. Becker, Ulrich Schurath, H. Dubost, and J. P. Galaup. Luminescence of metastable16O2(18O2) in solid argon: Relaxation and energy transfer. *Chemical Physics*, 125(2-3):321–336, oct 1988.

[56] Jun He and David R. Clarke. Polarization dependence of the Cr3+R-line fluorescence from sapphire and its application to crystal orientation and piezospectroscopic measurement. *Journal of the American Ceramic Society*, 80(1):69–78, jan 1997.

[57] C Chambers, T Walton, D Fairbank, A Craycraft, D R Yahne, J Todd, A Iverson, W Fairbank, A Alamre, J B Albert, G Anton, I J Arnquist, I Badhrees, P S Barbeau, D Beck, V Belov, T Bhatta, F Bourque, J P Brodsky, E Brown, T Brunner, A Burenkov, G F Cao, L Cao, W R Cen, S A Charlebois, M Chiu, B Cleveland, M Coon, M Côté, W Cree, J Dalmasson, T Daniels, L Darroch, S J Daugherty, J Daughhetee, S Delaquis, A Der Mesrobian-Kabakian, R DeVoe, J Dilling, Y Y Ding, M J Dolinski, A Dragone, J Echevers, L Fabris, J Farine, S Feyzbakhsh, R Fontaine, D Fudenberg, G Gallina, G Giacomini, R Gornea, G Gratta, E V Hansen, M Heffner, E W Hoppe, J Hößl, A House, P Hufschmidt, M Hughes, Y Ito, A Jamil, C Jessiman, M J Jewell, X S Jiang, A Karelin, L J Kaufman, D Kodroff, T Koffas, S Kravitz, R Krücken, A Kuchenkov, K S Kumar, Y Lan, A Larson, D S Leonard, G Li, S Li, Z Li,

C Licciardi, Y H Lin, P Lv, R MacLellan, T Michel, B Mong, D C Moore, K Murray, R J Newby, Z Ning, O Njoya, F Nolet, O Nusair, K Odgers, A Odian, M Oriunno, J L Orrell, G S Ortega, I Ostrovskiy, C T Overman, S Parent, A Piepke, A Pocar, J.-F. Pratte, D Qiu, V Radeka, E Raguzin, T Rao, S Rescia, F Retière, A Robinson, T Rossignol, P C Rowson, N Roy, R Saldanha, S Sangiorgio, S Schmidt, J Schneider, A Schubert, K Skarpaas, A K Soma, G St-Hilaire, V Stekhanov, T Stiegler, X L Sun, M Tarka, T Tolba, T I Totev, R Tsang, T Tsang, F Vachon, B Veenstra, V Veeraraghavan, G Visser, J.-L. Vuilleumier, M Wagenpfeil, Q Wang, J Watkins, M Weber, W Wei, L J Wen, U Wichoski, G Wrede, S X Wu, W H Wu, Q Xia, L Yang, Y.-R. Yen, O Zeldovich, X Zhang, J Zhao, Y Zhou, T Ziegler, and nEXO Collaboration. Imaging individual barium atoms in solid xenon for barium tagging in nEXO. *Nature*, 569(7755):203–207, 2019.

[58] Cryomech | The Original Innovators | https://www.cryomech.com/.

[59] Guy Dubuis, Xi He, and Ivan Božović. Sub-millikelvin stabilization of a closed cycle cryocooler. *Review of Scientific Instruments*, 85(10):103902, oct 2014.

[60] Hans-Jörg Himmel, Anthony J. Downs, and Tim M. Greene. Reactions of Ground State and Electronically Excited Atoms of Main Group Elements: a Matrix Perspective. *Chemical Reviews*, 102(11):4191–4242, nov 2002.

[61] M J Almond, R J H (Robin Jon Hawes) Clark, R E (Ronald E.) Hester, and A J Downs. *Spectroscopy of matrix isolated species*. Chichester ; New York : Wiley, 1989.

[62] Alvin M. Goodman. Optical interference method for the approximate determination of refractive index and thickness of a transparent layer. *Applied Optics*, 17(17):2779, sep 1978.

[63] J. M. (James Martin) Lafferty. *Foundations of vacuum science and technology*. Wiley, 1998.

[64] Eric Jones, Travis Oliphant, Pearu Peterson, and Others. {SciPy}: Open source scientific tools for {Python}.

[65] Giacinto Scoles, D R Miller, W Ronald Gentry, H Pauly, Davide Bassi, U.Hefter, K Bergman, Mario Zen, J Reuss, C J N van den Meijdenberg, D J. Abuerbach, M Kappes, Samuel Leutwyler, Ugo Valbusa, U Buck, Y T Lee, Paul Dagdigian, Steven Stolte, and Salvatore Iannotta. *Atomic and Molecular Beam Methods: Vol. 1*. 1998.

[66] O Kester, D Bazin, C Benatti, J Bierwagen, G Bollen, S Bricker, A C Crawford, S Chouhan, C Compton, K Davidson, J. DeLauter, M Doleans, L Dubbs, K Elliott, A Lapierre, W Hartung, M Johnson, S Krause, F Marti, J Ottarson, G Perdikakis, L. Popielarski, J Popielarski, M Portillo, R Rencsok, D Sanderson, S Schwarz, N Verhanovitz, J Vincent, J Wlodarczak, X Wu, J Yurkon, A Zeller, Q Zhao, A Schempp, and J Schmidt. ReA3 - The rare isotope reaccelerator at MSU. In *Proceedings - 25th Linear Accelerator Conference, LINAC 2010*, pages 26–30, 2011.

[67] X Wu, B Arend, C Compton, A Facco, M Johnson, D Lawton, D Leitner, F Montes, S Nash, J Ottarson, G Perdikakis, J Popielarski, A Rodriguez, M Syphers, W Wittmer, and Q Zhao. *THE DESIGN AND COMMISSIONING OF THE ACCELERATOR SYSTEM OF THE RARE ISOTOPE REACCELERATOR-ReA3 AT MICHIGAN STATE UNIVERSITY**. 2012.

[68] Antonio Villari, Stefan Schwarz, Ryan Ringle, Qiang Zhao, Randall Rencsok, Masanori Ikegami, Chandana Sumithrarachchi, Steven Lidia, Alain Lapierre, Georg Bollen, Tasha Summers, Rebecca Shane, Dan Crisp, David Morrissey, and Samuel Nash. On the Acceleration of Rare Isotope Beams in the Reaccelerator (ReA3) at the National Superconducting Cyclotron Laboratory at MSU. page TUOP04, 2017.

[69] Elena R. Dobrovinskaya, Leonid A. Lytvynov, and Valerian Pishchik. Properties of Sapphire. In *Sapphire*, pages 55–176. Springer US, Boston, MA, 2009.

[70] Mikkel Bregnhøj. *The Electronic Transitions of Molecular Oxygen*, volume 2. 2019.

[71] Kenji Takizawa and Seiichiro Koda. Emission spectra and relaxation mechanism of b state O2 in low temperature Ar solids. *Bulletin of the Chemical Society of Japan*, 75(10):2137–2145, oct 2002.

[72] G. Tyczkowski, U. Schurath, M. Bodenbinder, and H. Willner. Matrix-isolated oxygen: Lineshapes and transition probabilities of the b 1Σ+g→ X 3Σ-g b 1Σ+g→ a 1\Delta g and a1\Delta g → X 3Σ-g transitions. *Chemical Physics*, 215(3):379–396, mar 1997.

[73] John R. Taylor and William Thompson. *An Introduction to Error Analysis: The Study of Uncertainties in Physical Measurements*. University Science Books, 1997.

[74] John E. Greivenkamp. *Field Guide to Geometrical Optics*. SPIE, jan 2004.

[75] Guy K. White and Philip J. Meeson. Experimental Techniques in Low-Temperature Physics, 2002.

[76] Ray Radebaugh, James Zimmerman, David R. Smith, and Beverly Louie. A Comparison of Three Types of Pulse Tube Refrigerators: New Methods for Reaching 60K. In *Advances in Cryogenic Engineering*, pages 779–789. Springer US, Boston, MA, 2011.

[77] Zhu Shaowei, Wu Peiyi, and Chen Zhongqi. Double inlet pulse tube refrigerators: an important improvement. *Cryogenics*, 30(6):514–520, jun 1990.

[78] A. T.A.M. De Waele, P. P. Steijaert, and J. Gijzen. Thermodynamical aspects of pulse tubes. *Cryogenics*, 37(6):313–324, mar 1997.